Central exclusive production

A thesis submitted to the University of Manchester for the degree of
Doctor of Philosophy
in the Faculty of Engineering and Physical Sciences

2009

Timothy Daniel Coughlin

School of Physics and Astronomy

Contents

Total word count: 20526

List of Tables

List of Figures

Abstract

In this thesis we investigate the theoretical description of the central exclusive production process. We derive the form of the amplitude, proposed by the Durham group, by summing logarithmically enhanced corrections appearing in the perturbation series, to all orders in the strong coupling. Our results show however that the Durham result must be modified, specifically, that the scale appearing in the Sudakov factor, $\mu = 0.62\sqrt{\hat{s}}$, must be replaced with $\mu = \sqrt{\hat{s}}$, where $\sqrt{\hat{s}}$ is the invariant mass of the centrally produced system. We confirm this result with two fixed order calculations in different approaches and show that the replacement leads to approximately a factor 2 suppression in the cross-section with respect to the Durham result, for central system masses in the range 80-560 GeV.

In addition to the above we study the production of long-lived gluino pairs at the LHC, via the central exclusive production mechanism. We compute the rates for both bound-state and open production, with realistic experimental cuts. While we find that an observation of bound-state production is not feasible, the open production channel is and offers the possibility to measure the gluino mass to an accuracy of better than 1% for masses below 350 GeV, with 300 fb^{-1} of data.

Declaration

No portion of the work referred to in this thesis has been submitted in support of an application for another degree or qualification of this or any other university or other institution of learning.

Timothy Daniel Coughlin
School of Physics and Astronomy
University of Manchester
Oxford Road
Manchester
M13 9PL
November 2009

Copyright

The Author

The author was educated at Sale Grammar school between 1994 and 2001, before obtaining a first class MPhys (Hons) degree at the University of Manchester. The work presented in this thesis was undertaken at the University of Manchester, under the supervision of Jeff Forshaw.

Acknowledgements

First of all I would like to thank my family (Mike, Viv and Ceryn), who have always supported me, never more so than in the last year.

Next I would like to thank my supervisor Jeff. Not only for his choice of such an interesting topic, which has taught me a great deal, but for his support, insight and enthusiasm over the last four years.

The particle physics group in Manchester has been a very enjoyable place to work and while I can't thank everyone here, I would especially like to thank the following people: everyone in the theory office past and present, Simone, Phil, James, Irina, Chris T, Alessandra, Mark O, Chris J, Nasim, Paul M, Fred and Sabah. Special thanks go to Andy P, not least for his help generating the plots of chapter 4.

Outside of the physics department, I would like to thank all of the friends who have made living in Manchester so enjoyable. Thanks go especially to: Jo, Daniel, Andy, Martin, Cloe, Paul, Jon, Alison and Courtenay.

Finally, I would like to thank George Sterman, Misha Ryskin and Lance Dixon for their replies to my questions on their work, which helped my understanding so much. I would especially like to thank Misha and Valery Khoze, for taking the time to meet with me to discuss my work and theirs.

Chapter 1

Introduction

At hadron colliders, in events producing high transverse momentum particles in the central rapidity region, the colliding particles usually breakup. However, in a small fraction of such events the hadrons remain intact and scatter through very small angles, this type of production is known as central exclusive production (CEP). By adding detectors far down the beam-pipe from the interaction point, it is possible to measure the scattered hadrons. Such a measurement provides, potentially unique, information on the invariant mass and quantum numbers of the centrally produced system. Photon pairs, di-jets and χ_c particles produced in this way have now been observed at the Tevatron and there are groups within both the ATLAS and CMS collaborations actively seeking to observe these events at the LHC.

For a massive enough central system, the calculation of this type of process may be performed in perturbative Quantum Chromo Dynamics (QCD). At lowest order, in the strong coupling constant, two gluons in a colour singlet state are exchanged between the hadrons. Crucial however to a correct theoretical description of the process is the inclusion of logarithmically enhanced terms, appearing at all-orders in the QCD perturbation series. These enhanced terms are due to the infra-red divergence structure of QCD.

This thesis investigates the theoretical description, in perturbative QCD, of the CEP process. In addition, we demonstrate its advantages with respect to inclusive production in the specific example of long-lived gluino production. In chapter 2 we introduce the techniques used to analyse infrared divergences and the associated large logarithms in perturbation theory, which we shall use to study the CEP amplitude. In chapter 3 we describe methods, used in the subsequent chapters, to evaluate tree and one-loop level corrections in perturbation theory. In chapter 4 we analyse the CEP process, both at all orders and in two fixed order approaches. We compare our results to those obtained by Khoze, Martin and Ryskin (hereafter referred to as the Durham group) and assess the phenomenological impact of the difference between our result and theirs. In chapter 5 we study the production of hypothetical heavy coloured particles, known as gluinos. There we calculate the rates of bound-state and open production and discuss how the open production channel may be used to measure the gluino mass. Finally, in chapter 6, we conclude.

Chapter 2

Infrared divergences, factorisation and large logarithms

2.1 Infrared sensitivity in QCD

If we wish to make calculations in QCD using perturbation theory there are two obstacles which must be overcome. The first is that hadrons, not quarks and gluons, are the asymptotic states of the theory. Only the parts of the process which occur on short distance/time scales are amenable to a perturbative calculation and we must find a way to describe the transition between the hadron picture and the picture in terms of partons. In practice this is done by introducing parton distribution functions (pdfs), fragmentation functions and hadronisation models, which describe respectively, the distribution of partons in an incoming hadron, the distribution of a measured final-state hadron in a collection of partons and the way in which partons convert to the measured hadrons in the final-state. All of these pieces must presently be fit to data. The second problem to overcome is of a more technical nature. It turns out that in any calculation involving incoming or outgoing partons, the perturbation series will contain terms which are due

to long distance/time physics. Of course, the perturbation series is not a good approximation for these pieces and the result is a divergent answer, a so called infrared divergence. The presence of such terms would seem to indicate that our division of the calculation into a separate non-perturbative and perturbative piece is not correct. It is possible to show however, that for observables involving a large momentum transfer, all of the problem terms in the perturbation series either cancel in the sum of diagrams, or can be collected into universal factors, dependent only on the incoming or, measured, final-state particles. These factors may then be absorbed into a redefinition of the pdfs and/or fragmentation functions. This result is known as factorisation and without it using perturbation theory to do precision collider physics involving hadrons would be impossible (see [1] for a review).

In the following sections we review some of the key steps in the proof of factorisation in QCD, using the inclusive Deep Inelastic Scattering (DIS) process to illustrate some of the main points. Following this, we shall discuss the definitions and behaviour of pdfs under changes of momentum scale. Finally, we shall end the chapter by describing how one may treat low energy (soft) gluons in perturbation theory.

2.2 Identification of infrared sensitivity in perturbation theory

As already stated, long distance/time contributions to perturbation theory in QCD show up as infrared divergences. To understand the origin of such divergences, consider the following integral, associated with some Feynman diagram

$$I = \prod_i \int d^4 l_i \frac{N}{\prod_j \left(q_j^2(\{l_k\}, \{p_k\}) + i\varepsilon \right)} \,, \tag{2.1}$$

where the l_i are loop momenta, the p_i are external momenta, the q_j are linear combinations of these loop and external momenta, N is a numerator factor and we have taken all particles as massless. The $i\varepsilon$ factors displace the poles of (2.1) from the real axis of each loop momentum integration, ensuring the integral is well defined[1]. Infrared divergences are due to these poles migrating to the real axis as we take the limit $\varepsilon \to 0^+$. However, a denominator may vanish in many ways, due to the form of the Minkowski metric. Not all such poles lead to a divergence in the limit $\varepsilon \to 0^+$, as we now discuss.

2.2.1 Pinch singularities

The following simple example shows that a vanishing denominator is not sufficient to guarantee a divergence. Consider the following integrals

$$I_\pm = \int_{-\infty}^{\infty} dk \frac{1}{(k + i\varepsilon)(k \pm i\varepsilon)} \,. \tag{2.2}$$

In both cases a pair of poles approach the real k axis as we take ε to zero. However, only I_- is divergent in this limit, since for I_+ we may close the contour in the upper half plane and enclose no poles, obtaining zero. The difference between the two cases is that for I_+ the poles approach the contour (real axis) from the same direction, we may thus deform the contour away from them, avoiding a divergence. In the case of I_- however, the poles approach from opposite sides of the contour and trap, or "pinch" it, thus making the singularities impossible to avoid. In addition to such "pinch singularities", a divergence may also result from the migration of a pole to the end-point of an integration contour. Again, the contour may not be deformed away from this point, resulting in a divergence. Note that for multiple integrals the singular points and integration contours become hyper-surfaces. We will refer to singular surfaces which pinch the contour (integration surface) as pinch surfaces (see e.g. [2]).

[1] We assume that ultraviolet divergences have either been regulated or subtracted.

Returning to our Feynman diagram integral, (2.1), we may now establish which singular surfaces of the integrand produce divergences, our analysis will follow very closely that given in [3]. Let us first narrow our attention to a specific region of the full integration space. We divide the propagators into two sets, F and Z. In the integration region under consideration, the momenta of lines in F carry finite momenta and the momenta of lines in Z approach zero (we shall refer to these lines as soft). Furthermore, we decompose the loop integrals into two sets, L_F and L_Z. L_F contains loops with propagators in F only and L_Z consists of all other loops, i.e. those containing at least one propagator in Z.

We now introduce Feynman parameters for the propagators in F only. Thus I becomes:

$$I = \prod_{i\in L_Z} \int d^4k_i \frac{1}{\prod_{j\in Z}\left(q_j^2(\{k\})+i\varepsilon\right)} \prod_{k\in F} \int_0^1 d\alpha_k \, \delta\left(\sum_{m\in F}\alpha_m - 1\right) \times \prod_{n\in L_F} \int d^4l_n \frac{N\,(n_F-1)!}{\left(\sum_{r\in F}\alpha_r q_r^2(\{k,l\})+i\varepsilon\right)^{n_F}} \,, \tag{2.3}$$

where n_F is the number of lines in F and we relabelled the soft loop momenta, $l_{i\in L_Z} = k_i$. Now observe that the soft loop momenta, k_i, are pinched at $k_i^\mu = 0$, independently of the finite momenta, due to the fact that each of these loop momenta has an associated propagator, $(k_i^2 + i\epsilon)^{-1}$, which provides a double pole, pinching k_i^0 at the origin as $|\boldsymbol{k}_i|$ vanishes. In addition, the configurations of finite momenta that generate pinch surfaces may be identified by use of the Landau equations [2, 4]. These give, for each line, i, in F:

$$\begin{aligned} & q_i^2 = 0 \,, \\ \text{and/or} \qquad & \alpha_i = 0 \,, \end{aligned} \tag{2.4}$$

and around each closed loop, j, in either L_F or L_Z:

$$\sum_{i\in\text{closed loop } j} \eta_{ji}\alpha_i q_i^\mu = 0 \qquad i \in F \,, \tag{2.5}$$

where η_{ji} is an incidence matrix, equal to $+1$ if q_i is in the same direction as the loop momentum l_j and -1 if they are in opposite directions. Note that in equation (2.5) the restriction $i \in F$ is obtained by taking the soft limit, $q_{i \in Z} \to 0$. We now proceed to discuss the interpretation of these equations.

2.2.2 Reduced diagrams and physical pictures

The interpretation of equations (2.4) and (2.5) is facilitated by a technique introduced by Coleman and Norton for massive particles [5] and later adapted by Sterman for the massless case [3]. We begin by considering a particular pinch singularity of a Feynman diagram, as defined by equations (2.4) and (2.5), for one or more of the loop integrations. We then shrink all lines which are off-shell to a point, forming what is called a reduced diagram.

The remaining lines now obey a "physical picture" in which, for lines carrying finite momentum, the diagram must represent a scattering process of classical particles, i.e. they are all on their mass-shell. This observation is a consequence of equation (2.5).

For massless particles this condition is highly restrictive and allows us to show that pinch surfaces of lines in F are always associated with jets of collinear particles [3].

2.2.3 An example

To illustrate the above procedure, consider the diagram shown in figure 2.1, with $p_1^2 = p_2^2 = 0$ and $p_1 \cdot p_2 \neq 0$. If we first take all lines in F, equation (2.5) becomes:

$$\alpha_1(k + p_1)^\mu + \alpha_2 k^\mu + \alpha_3(k - p_2)^\mu = 0 \ , \tag{2.6}$$

which together with equation (2.4) has the following two solutions:

$$k^\mu = -zp_1^\mu \ , \qquad \alpha_3 = 0 \ , \qquad \alpha_1 = \frac{z}{1-z}\alpha_2 \ , \tag{2.7}$$

$$k^\mu = zp_2^\mu \ , \qquad \alpha_1 = 0 \ , \qquad \alpha_3 = \frac{z}{1-z}\alpha_2 \ , \tag{2.8}$$

where $0 < z < 1$ but is otherwise arbitrary. Figures 2.2(a) and 2.2(b) show the reduced diagrams associated with solutions (2.7) and (2.8) respectively and we see that they correspond to particles moving collinearly with respect to either p_1 or p_2.

If we now consider the soft region, noting that only one of the three lines may be in Z due to the kinematics, we have three solutions:

$$k^\mu = 0 \ , \qquad \alpha_1 = \alpha_3 = 0 \ , \tag{2.9}$$

$$k^\mu = -p_1^\mu \ , \qquad \alpha_2 = \alpha_3 = 0 \ , \tag{2.10}$$

$$k^\mu = p_2^\mu \ , \qquad \alpha_1 = \alpha_2 = 0 \ . \tag{2.11}$$

The reduced diagram corresponding to solution (2.9) is shown in figure 2.2(c) and figures 2.2(d) and 2.2(e) represent solutions (2.10) and (2.11) respectively. Thus we see that while the reduced diagrams associated with collinear configurations have the structure of a classical scattering process, this is not always the case for the soft momenta.

So far we have simply been looking for configurations involving a (unavoidable) vanishing denominator. In fact, as we shall discuss in the next section, some of these singularities are integrable and so produce no divergence.

2.3 Power counting

Further restrictions on the parton configurations that may produce a divergence are obtained if we study the behaviour of the integrand in the vicinity of a pinch

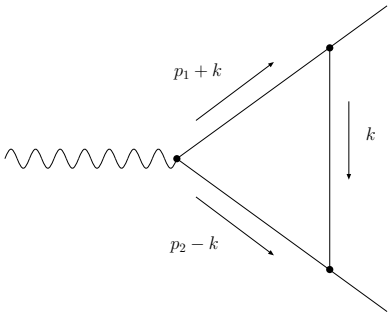

Figure 2.1: A low order graph possessing infrared divergences.

surface. The integral about a pinch surface may still be finite, if the volume of integration and numerator vanish quickly enough as we approach the singularity.

The behaviour about a pinch singularity is analysed by separating the loop and phase-space integrals of the corresponding reduced diagram into two sets. One set is termed the "intrinsic" variables and the other the "normal" variables [3, 6, 7]. Varying the intrinsic set moves us within the singular surface whereas varying

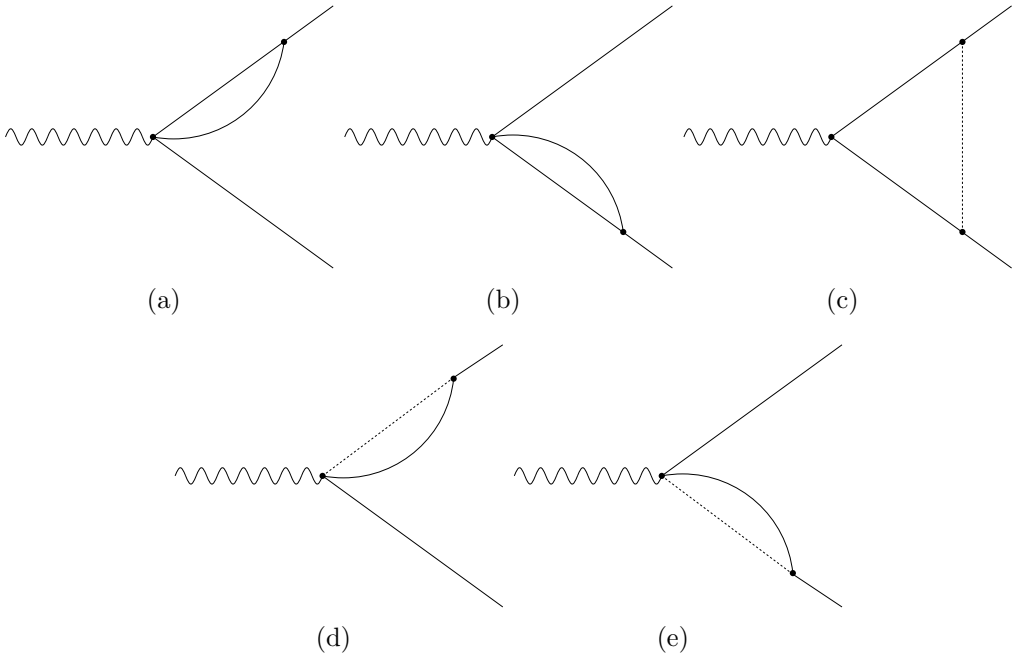

Figure 2.2: The reduced diagrams associated with the diagram shown in figure 2.1. Dotted and solid lines represent partons with vanishing and finite momenta respectively.

the normal components moves us away from the singular surface. To give an example, consider a pinch surface at which a set of lines with finite momenta are all collinear to one another and moving in the plus light-cone direction[2]. The normal variables are the components of the loop integrals in the minus and transverse directions, since varying these make the momenta no longer collinear and thus move us away from the pinch surface. The intrinsic variables are the plus components of the loop integrals, since after varying these the particles are still collinear and on-shell.

To analyse the behaviour of the integrand we count powers of the normal variables according to the following procedure [3, 6, 7]:

1. Introduce a parameter, λ, which parameterises the approach of the normal variables to the pinch surface, such that we approach the pinch surface as $\lambda \to 0$. Then scale each normal variable, κ_i, according to some power of this variable, a_i, to be determined:

$$\kappa_i = \lambda^{a_i} \kappa_i' \, . \tag{2.12}$$

2. We now approximate the denominators in the graph, keeping only the leading power, λ^{A_j}, for denominator j i.e.

$$(q_j^2(\kappa_i))^{-1} \approx \lambda^{-A_j} f(\kappa_i') \, , \tag{2.13}$$

where f is independent of λ. It is at this step that the a_i introduced in step 1 are chosen, such that the approximated integrand is not independent of any of the κ_i'.

3. The behaviour of the graph as $\lambda \to 0$ is now bounded by λ^d (i.e. its behaviour is as divergent as this, or better), where:

$$d = \sum_i a_i - \sum_j A_j + n \, . \tag{2.14}$$

[2]We define the light-cone components as: $p^{\pm} = \frac{1}{\sqrt{2}}(p^0 \pm p^3)$.

The first term here comes from the Jacobian of the change of variables (2.12), the second term is due to the propagators, equation (2.13), and the final term, n, is a possible suppression factor due to powers of normal variables appearing in the numerator.

$d > 0$ indicates the integration region under consideration gives a vanishing contribution at the singularity. $d = 0$ indicates the integration is finite in this region, up to possible logarithmic divergences. Finally, $d < 0$ suggests the integral may diverge like a power. Note that d only gives a bound on the integral's behaviour, the integral may be less divergent than the power counting suggests, or even finite.

4. To complete the power counting bound, we must ensure that the approximated integral produced in step 2 does not contain any additional pinch surfaces to those in the original integral. If it does, this indicates that there is another possible scaling of the normal variables (equation (2.12)) consistent with step 2. We must then also calculate the degree of divergence of this momentum region to complete the bound.

As stated in step 2 above, the scaling choices it is necessary to consider are those for which the approximated diagram retains dependence on all of the normal variables. The possible scalings which respect this condition are found to be [3, 8, 9]

Collinear: For a parton collinear to the plus lightcone direction we have

$$(k^+, k^-, k_\perp) \sim (1, \lambda, \sqrt{\lambda}) \tag{2.15}$$

Soft: There are two types of soft scaling,

(a) **Infrared:**

$$(k^+, k^-, k_\perp) \sim (\lambda, \lambda, \lambda) \tag{2.16}$$

(b) **Glauber/Coulomb:**

$$(k^+, k^-, k_\perp) \sim (\lambda, \lambda, \sqrt{\lambda}) \tag{2.17}$$

where "$\sim$" should be read "scales as". The Glauber/Coulomb region arises when one considers poles in the soft momenta due to finite momentum collinear propagators going on-shell [8, 9]. For example, in figure 2.1, if we take the momenta p_1 and p_2 to be moving in the plus and minus lightcone directions respectively, then the poles in $(p_1 + k)^2$ and $(p_2 - k)^2$ give

$$2k^- p_1^+ = -k^2 \ , \tag{2.18}$$

$$2k^+ p_2^- = k^2 \ , \tag{2.19}$$

resulting in the scalings of equation (2.17). Considering now the approximation of this diagram (step 2), we see that for the infrared region, the propagators become

$$(p_1 + k)^2 \approx 2p_1^+ k^- \ , \tag{2.20}$$

$$(p_2 - k)^2 \approx -2p_2^- k^+ \ . \tag{2.21}$$

So while the $k^\pm$ dependence is shared between soft and finite momentum propagators, the $k_\perp$ dependence enters only through the soft propagator. For the Glauber/Coulomb region however, the situation is reversed and the approximated propagators are given by

$$k^2 \approx k_\perp^2 \ , \tag{2.22}$$

$$(p_1 + k)^2 \approx 2p_1^+ k^- + k_\perp^2 \ , \tag{2.23}$$

$$(p_2 - k)^2 \approx -2p_2^- k^+ + k_\perp^2 \ . \tag{2.24}$$

So the $k_\perp$ dependence is shared between finite and soft momentum propagators, whereas the $k^\pm$ dependence is not. Thus we see that the difference between the

two soft regions is where in the approximated diagram the dependence on their normal variables resides.

The proof that in fact the Glauber/Coulomb region does not contribute any infrared divergences is one of the most technical aspects involved in the proof of factorisation (for processes with more than one initial-state hadron) [10, 11]. We shall not consider it further here, however, it is interesting to note that it can contribute to large logarithmic corrections in certain, non-inclusive, observables [12–14].

2.4 Physical picture and power counting for Inclusive Deep Inelastic Scattering

We turn now to the application of these techniques to the case of inclusive DIS, as computed in the Feynman gauge. The physical picture and the infrared power counting technique will highly constrain the form of the diagrams. Then, in the subsequent sections, we shall introduce the additional manipulations required to write the result in a factorised form.

2.4.1 Form of the reduced diagrams

The general reduced diagram for DIS is shown in figure 2.3. The incoming parton breaks up into any number of collinear partons, some of these interact with the electron/virtual photon at a "hard" vertex, H, which contains only off shell lines (including the virtual photon). The rest are contained in the sub-diagram J. From the hard vertex are produced one or more separate jets, J_i, of collinear partons. In addition to this, soft partons (represented by dotted lines) may interact with all parts of the diagram including each other, in a sub-diagram S.

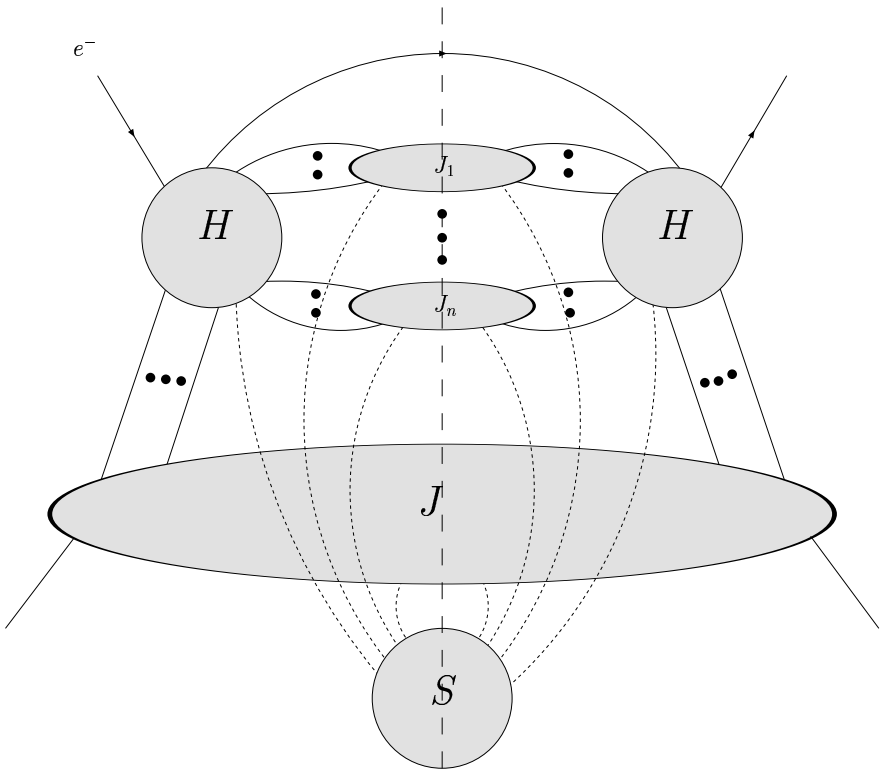

Figure 2.3: General form of the DIS reduced diagram. Solid, arrow-less lines and dotted lines denote collinear and soft partons respectively.

2.4.2 Final state jet cancellation

Before going on to apply the power counting technique to DIS, we will first show that the final state jets, J_i, do not contribute to the pinch surface. In order to do so we must sum over all cuts of the diagram shown in figure 2.3. We may then make use of the "generalised unitarity" identity, which states that if we sum over the cuts of a graph, G_C, this sum is proportional to the imaginary part of the graph without the cut, G (see e.g. [7]):

$$\sum_C G_C = 2\Im m(-iG) \; . \tag{2.25}$$

The "generalised" term derives from the fact that this identity holds for *fixed spatial momenta* of the lines appearing in the diagram. This is important if we wish to retain a distinction between finite and zero momentum lines. The

key observation now is that the pinch surfaces of the un-cut graph are *not* the same as those of the cut graphs. In particular, the physical picture implies that the graph must represent the on-shell scattering of classical particles. However, in the un-cut graph, the jets, J_i, are emitted from the left-hand hard vertex and travel at the speed of light until they recombine at the hard vertex on the right. This is only possible if they travel collinearly to one another and the incoming proton. However, recall that the centre-of-mass energy of the proton-virtual photon system is given by (neglecting the proton mass)

$$(p+q)^2 = \frac{(1-x)Q^2}{x} \,, \tag{2.26}$$

with:

$$x = \frac{Q^2}{2p\cdot q} \,, \tag{2.27}$$

$$Q^2 = -q^2 \,, \tag{2.28}$$

and p and q denote the proton and virtual photon momenta respectively. Therefore, the final state momenta may only be mutually collinear if x approaches 1. This region however corresponds to elastic scattering and is highly suppressed in Q^2 relative to the inclusive DIS cross-section.

Since, as a result of the above considerations, reduced diagrams with jets in the final state do not contribute to a pinch singularity in the sum of cuts, we may henceforth ignore them. Doing so, the general reduced diagram for DIS becomes that shown in figure 2.4. We now proceed to simplify this picture further and uncover its internal structure by use of the power counting technique.

2.4.3 Power counting analysis

We will now find the degree of divergence, d, associated with the reduced diagram of figure 2.4. We shall find that d depends on certain features of the diagram. By

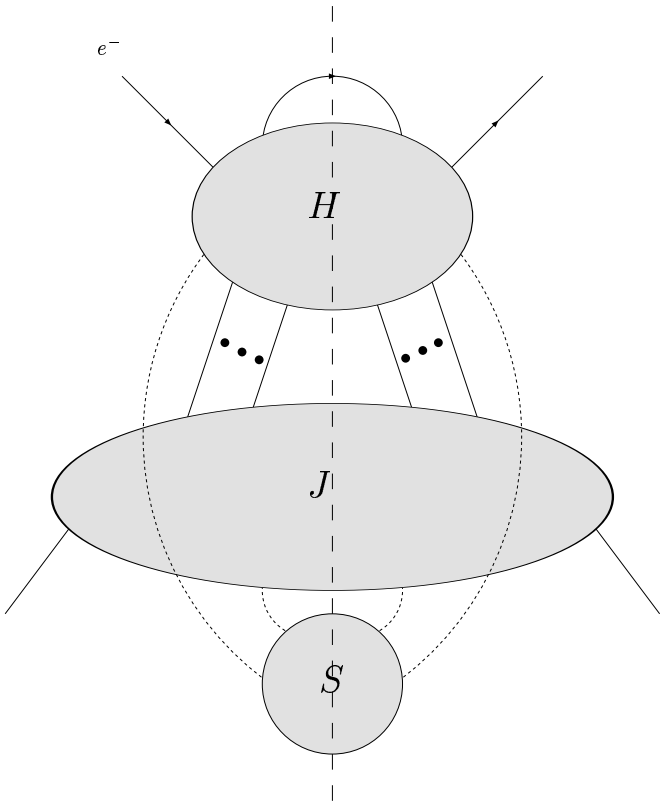

Figure 2.4: General form of the DIS reduced diagram after final state jet cancellation.

excluding those features whose presence give $d > 0$ we may constrain the form of the diagram still further.

Useful identities

Before launching into the calculation of d, we state some graph-theoretic identities which will prove useful. The first is "Euler's identity":

$$L = N + 1 - V \ , \tag{2.29}$$

where L is the number of loops in the graph, N is the number of lines *internal* to the graph and V is the total number of vertices of the graph. In addition to Euler's identity, we have two relations which express the "end-conservation" of

gluon (g) and fermion (f) lines respectively:

$$2N^{(g)} + E^{(g)} = \sum_n nV^{(ng)\{a\}} \ , \tag{2.30}$$

$$2N^{(f)} + E^{(f)} = \sum_n nV^{(nf)\{a\}} \ , \tag{2.31}$$

where $E^{(i)}$ and $N^{(i)}$ are, respectively, the number of external and internal lines of type i and $V^{(ni)\{a\}}$ is the number of vertices in the diagram connecting n lines of type i along with any other set of lines a, such that $a \neq i$.

Power counting for J

We now derive the contribution of the finite momentum collinear lines to the degree of divergence, d_J.

We take the collinear lines to be moving in the plus light-cone direction with the scalings given in equation (2.15). Thus equation (2.14) gives us

$$d_J = 2L_J - (N_J + E_J) + n_J \ , \tag{2.32}$$

where L_J is the number of internal loops in J and between J and H involving only finite momentum lines. N_J is the number of lines in J and E_J is the number of finite momentum lines that connect J to H. As before, n_J is a numerator suppression factor. Now applying Euler's identity, (2.29), we obtain

$$L_J = N_J + E_J + 1 - V_J \ , \tag{2.33}$$

where V_J is the number of vertices in J plus the one hard vertex. This gives us

$$d_J = N_J + E_J - 2(V_J - 1) + n_J \ . \tag{2.34}$$

We now re-write V_J as

$$V_J = 1 + \sum_{\alpha \geq 3} x_\alpha + \sum_{\alpha \geq 2} y_\alpha \ , \tag{2.35}$$

where x_α is the number of α-point vertices connecting only finite momentum lines in J and y_α is the number of vertices connecting α finite momentum lines in J with at least one soft line. In addition, conservation of the ends of the finite momentum lines gives

$$\sum_{\alpha\geq 3} \alpha x_\alpha + \sum_{\alpha\geq 2} \alpha y_\alpha = 2N_J + E_J + 2 \; . \tag{2.36}$$

We now use equations (2.35) and (2.36) to replace V_J and N_J in equation (2.34):

$$d_J = \frac{(E_J - 2)}{2} + \frac{1}{2}\left(\sum_{\alpha\geq 3}(\alpha - 4)x_\alpha + \sum_{\alpha\geq 2}(\alpha - 4)y_\alpha\right) + n_J \; . \tag{2.37}$$

Power counting for S

Next we deal with the contribution of the soft lines to the degree of divergence, d_S. As discussed previously, we shall only consider the infrared scaling of equation (2.16), which implies

$$d_S = 4L_S - 2N_S^{(g)} - 2E_S^{(g)} - N_S^{(f)} - E_S^{(f)} + n_S \; , \tag{2.38}$$

where $N_S^{(i)}$ and $E_S^{(i)}$ are, respectively, the number of soft lines, of type i, internal to S, and connecting S to J or H. A few comments are in order here. We have grouped the ghost lines in with the fermions and have included an extra positive power of λ for each fermion propagator. For the quarks this simply comes from the power of momentum appearing in the propagator numerator, whereas for the ghosts it is due to the power of momentum associated with each ghost-gluon vertex.

Again we use Euler's identity to obtain

$$L_S = \sum_{i=g,f}\left(N_S^{(i)} + E_S^{(i)}\right) + 1 - V_S \; , \tag{2.39}$$

where V_S is the number of vertices internal to S plus 1, from regarding J and H as a single vertex for the purposes of the identity. In addition we define

$$V_S = 1 + \sum_{\substack{n,m \\ n+m\geq 3}} V_S^{(ng)(mf)} \; , \tag{2.40}$$

where $V_S^{(ng)(mf)}$ is the number of vertices, internal to S, connecting n gluon lines and m fermion lines. Furthermore, we have the gluon and fermion end conservation equations:

$$2N_S^{(g)} + E_S^{(g)} = \sum_{\substack{n,m \\ n+m\geq 3}} nV_S^{(ng)(mf)} \ , \tag{2.41}$$

$$2N_S^{(f)} + E_S^{(f)} = \sum_{\substack{n,m \\ n+m\geq 3}} mV_S^{(ng)(mf)} \ . \tag{2.42}$$

Now substituting equations (2.39-2.42) into (2.38) we obtain

$$d_S = E_S^{(g)} + \frac{3}{2}E_S^{(f)} + \sum_{\substack{n,m \\ n+m\geq 3}} \left(n + \frac{3m}{2} - 4\right) V_S^{(ng)(mf)} + n_S \ . \tag{2.43}$$

We may now find a lower bound for d_S as

$$d_S \geq E_S^{(g)} + \frac{3}{2}E_S^{(f)} - V_S^{(3g)(0f)} + V_S^{(NE)} + n_S \ , \tag{2.44}$$

where $V_S^{(NE)}$ is the number of vertices of "non-elementary form". In other words such vertices do not appear in the Feynman rules. Note however that $V_S^{(3g)(0f)}$ may include off-shell lines which have been contracted to a point.

Now note that for each of the three-gluon vertices, $V_S^{(3g)(0f)}$, there is a power of soft momentum present in the numerator. Thus we have for the numerator suppression factor, $n_S \geq V_S^{(3g)(0f)}$ and so finally:

$$d_S \geq E_S^{(g)} + \frac{3}{2}E_S^{(f)} + V_S^{(NE)} \ . \tag{2.45}$$

Combining the results

The full degree of divergence of the general DIS reduced diagram is now given by

$$\begin{aligned} d &= d_J + d_S \\ &\geq \frac{(E_J - 2)}{2} + \frac{1}{2}\sum_{\alpha\geq 4}(\alpha - 4)(x_\alpha + y_\alpha) + n_J - \frac{x_3}{2} \\ &\quad - \left(y_2 + \frac{y_3}{2}\right) + E_S^{(g)} + \frac{3}{2}E_S^{(f)} + V_S^{(NE)} \ . \end{aligned} \tag{2.46}$$

This expression seems to allow for an arbitrarily negative degree of divergence, by increasing x_3, y_2 or y_3, i.e. no bound at all on the divergent behaviour. However, we have not yet taken the numerator suppression factor, n_J, into account. For each three point vertex appearing in the jet there is a power of jet momentum, with scaling properties given by (2.15). These momenta must either combine to form invariants or contract with free Lorentz indices external to the jet, i.e. those due to soft gluons attaching to the jet or gluons entering the hard scattering. Each invariant is proportional to λ and so provides a suppression factor, however, the momenta attaching to external Lorentz indices may avoid such a suppression since the plus components of the jet momenta scale as λ^0. We may thus find a lower bound for n_J as[3]:

$$n_J \geq \max\left(\frac{x_3 + y_2^{(1)} - E_S^{(+g)} - E_J^{(+g)}}{2}, 0\right) . \tag{2.47}$$

Here $y_\alpha^{(\beta)}$ denotes the number of vertices between α finite momentum lines and β soft lines, $E_S^{(+g)}$ and $E_J^{(+g)}$ are, respectively, the number of soft gluons attaching to the jet and the number of jet gluons attaching to the hard scattering whose Lorentz indices are contracted with jet momenta in the plus direction. In addition to (2.47) we make the following replacement:

$$E_S^{(f)} + E_S^{(g)} = \sum_{\alpha,\beta} \beta y_\alpha^{(\beta)} . \tag{2.48}$$

The degree of divergence is now given by

$$\begin{aligned} d \geq & \frac{\left(E_J - 2 - E_J^{(+g)}\right)}{2} + E_S^{(f)} + \frac{\left(E_S^{(g)} - E_S^{(+g)}\right)}{2} \\ & + \frac{1}{2}\sum_{\beta\geq 2}(\beta-2)y_2^{(\beta)} + \frac{1}{2}\sum_{\beta\geq 2}(\beta-1)y_3^{(\beta)} + \sum_{\alpha\geq 4}\sum_{\beta}\beta y_\alpha^{(\beta)} \\ & + \frac{1}{2}\sum_{\alpha\geq 4}(\alpha-4)(x_\alpha + y_\alpha) + V_S^{(NE)} . \end{aligned} \tag{2.49}$$

[3]This is the case in Feynman gauge, however in a physical gauge, for example the planar gauge, additional connections of gluons to the hard scattering sub-diagram receive a suppression for all components of the jet momenta.

Note that $E_J \geq 2 + E_J^{(+g)}$, since there must be at least two partons connecting the jet with the hard vertex which are not gluons contracted with the plus component of a jet momentum. If this is not the case the diagram vanishes due to the Ward identity, since such gluons are effectively longitudinally polarised (we shall discuss this point in more detail in the next section). Now observe that $d \geq 0$, so the cross-section is at worst logarithmically divergent. If we now keep only features of the diagram that give $d = 0$ we obtain the following constraints:

- There are only two fermions or transversely polarised gluons connecting J with H (one each side of the cut). All other finite momentum lines connecting the two are gluons with polarisation vectors in the plus direction.
- S only connects to J and only through gluons whose polarisation vectors are contracted with a vector in the plus direction.
- Aside from H the diagram contains only three and four-point vertices.

The second of these points ensures that the soft corrections are sub-leading in the power counting, since the tensor structure of the soft diagram always leads to plus momenta being contracted together[4] [1].

2.4.4 Factoring the additional collinear gluons

We mentioned in the previous section that the additional gluons connecting J and H are effectively longitudinally polarised. Let us now explain how this comes about. Consider one of the additional gluons, with momentum q. J and H are contracted through the Lorentz indices of this gluon, which we represent as $J^\mu(q)H_\mu(q)$. By the analysis of the previous section, J^μ must be in the plus

[4]This point is slightly non-trivial. The soft diagram can give a contribution for which none of its Lorentz indices are connected by a metric tensor. Such a contribution however vanishes by the Ward identity [15].

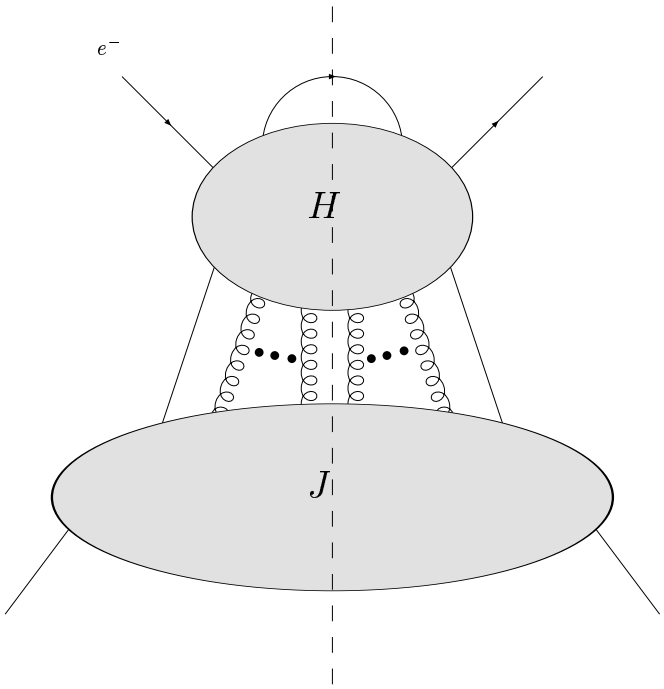

Figure 2.5: General form of the DIS reduced diagram after the power counting analysis.

direction in order to give $d = 0$, thus

$$J^\mu(q)H_\mu(q) = u \cdot J(q) v \cdot H(q) \ , \tag{2.50}$$

where $v^\mu = \delta^\mu_+$ and $u^\mu = \delta^\mu_-$. Also, in H, we may neglect the components of q in the minus and transverse directions since they are small compared to momenta in H. If, in addition, we multiply (2.50) by $1 = \frac{q^+}{q \cdot u - i\varepsilon}$, we obtain

$$J^\mu(q)H_\mu(q) \approx J^+(q) \frac{\hat{q}^\mu H_\mu(\hat{q})}{q \cdot u - i\varepsilon} \ , \tag{2.51}$$

where $\hat{q}^+ = q^+$ and $\hat{q}^- = \hat{q}_\perp = 0$. Now observe that $\hat{q} \cdot H(\hat{q})$ describes a set of diagrams with an external gluon attached whose polarisation vector is in the direction of its momentum, i.e. it is longitudinally polarised. If H^μ contained all the diagrams of an S-matrix element then $\hat{q} \cdot H(\hat{q})$ would vanish by the Ward identity[5]. This is not the case however, since we are missing some diagrams.

[5]Since all lines in H are off-shell we may take its external lines to be exactly massless.

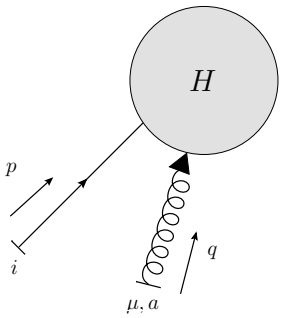

(a) Example of part of a reduced diagram.

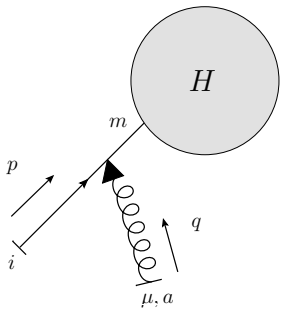

(b) Example of a diagram not included in H.

Figure 2.6: Longitudinal gluon insertions. See figure 2.7 for definitions of the diagrammatic rules.

To explain, consider the section of a reduced diagram shown in figure 2.6(a). The gluon is longitudinally polarised, as represented by the arrow at its end (see figure 2.7). Not included in the hard vertex, H, of this reduced diagram is the contribution shown in figure 2.6(b). The sum of the two vanishes by the Ward identity, so we have the first relation shown in figure 2.8. Also shown in figure 2.8 is the contribution of this diagram written in terms of the so-called eikonal Feynman rules (see for example [1]), given in figure 2.9.

Multiple attachments may be treated iteratively in much the same way, with the "missing" diagrams now being all those involving a connection between the incoming collinear particles. This is shown in figure 2.10 for the case of two longitudinally polarised gluons. On the first line of figure 2.10, q_1 is extracted from the hard scatter using the Ward identity. This time, as well as the connection to the quark line, an attachment to the other longitudinally polarised gluon must also be included. In the next line, the identity of figure 2.8 is applied to extract

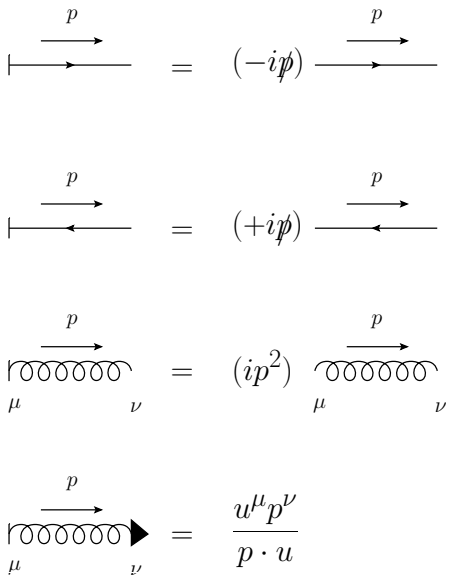

Figure 2.7: Diagrammatic rules representing amputated external lines and longitudinally polarised gluons.

the remaining longitudinally polarised gluon. The result may be written

$$H^{\alpha_1\alpha_2}_{i\ a_1a_2}(p,q_1,q_2)\frac{q_{1\alpha_1}q_{2\alpha_2}u^{\mu_1}u^{\mu_2}}{(q_1\cdot u)(q_2\cdot u)}$$
$$= H_n(p+q_1+q_2)\left\{\left(\frac{i}{(-q_2\cdot u)}igt^{a_2}_{nm}u^{\mu_2}\right)\left(\frac{i}{(-q_1\cdot u)}igt^{a_1}_{mi}u^{\mu_1}\right)\right.$$
$$\left.+\left(\frac{i}{(-q_1-q_2)\cdot u}igt^{a_3}_{ni}u^{\mu_2}\right)\left(\frac{i}{(-q_1\cdot u)}ig(-if^{a_1a_3a_2})u^{\mu_1}\right)\right\}\ . \quad (2.52)$$

This may in turn be re-written, using the commutation relation: $if^{a_1a_2a_3}t^{a_3} = [t^{a_1},t^{a_2}]$ and the following identity:

$$\frac{1}{q_1\cdot u\ q_2\cdot u}-\frac{1}{(q_1+q_2)\cdot u\ q_1\cdot u}=\frac{1}{q_2\cdot u\ (q_1+q_2)\cdot u} \quad (2.53)$$

to give the expression shown on the final line of figure 2.10.

The result of factorising any number of longitudinally polarised gluons is shown in figure 2.11 and may be proved by induction [16]. The result of applying this identity to the inclusive DIS cross-section is shown in figure 2.12, note however that unlike in figure 2.11, there is no sum over permutations of the gluons, since this is included in the sum of all possible attachments of the gluons to J.

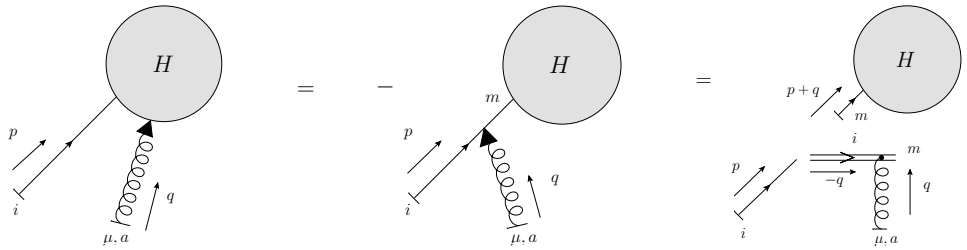

Figure 2.8: Application of the Ward identity. See figures 2.7 and 2.9 for the diagrammatic rules used.

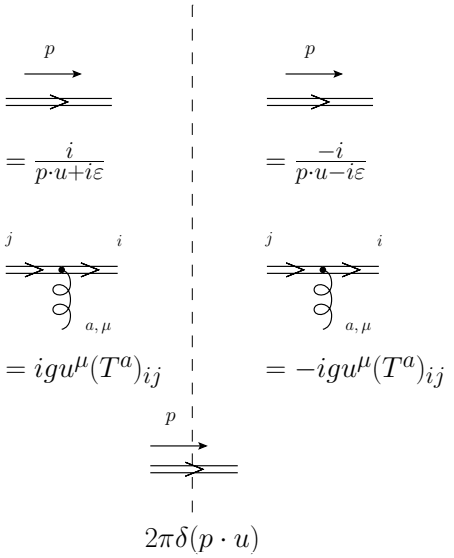

Figure 2.9: Eikonal Feynman rules. The SU(3) generators are given by $(T^a)_{ij} = t^a_{ij}$ for quarks and $(T^a)_{ij} = -if^{aij}$ for gluons.

The eikonal line structure we have uncovered may be identified with the perturbative expansion of a Wilson line, or path ordered exponential of the gluon field [1]:

$$[z_1^-, z_2^-] = P\text{exp}\left[ig\int_{z_2^-}^{z_1^-} dz'^- A_c^+(z'^-)t^c\right] . \tag{2.54}$$

2.4.5 Factorised form

Having factorised the cross-section diagrammatically, as shown in figure 2.12, we may now factorise it kinematically as well. We note that H depends only on k^+, since all other components of k are much smaller than the momenta in H.

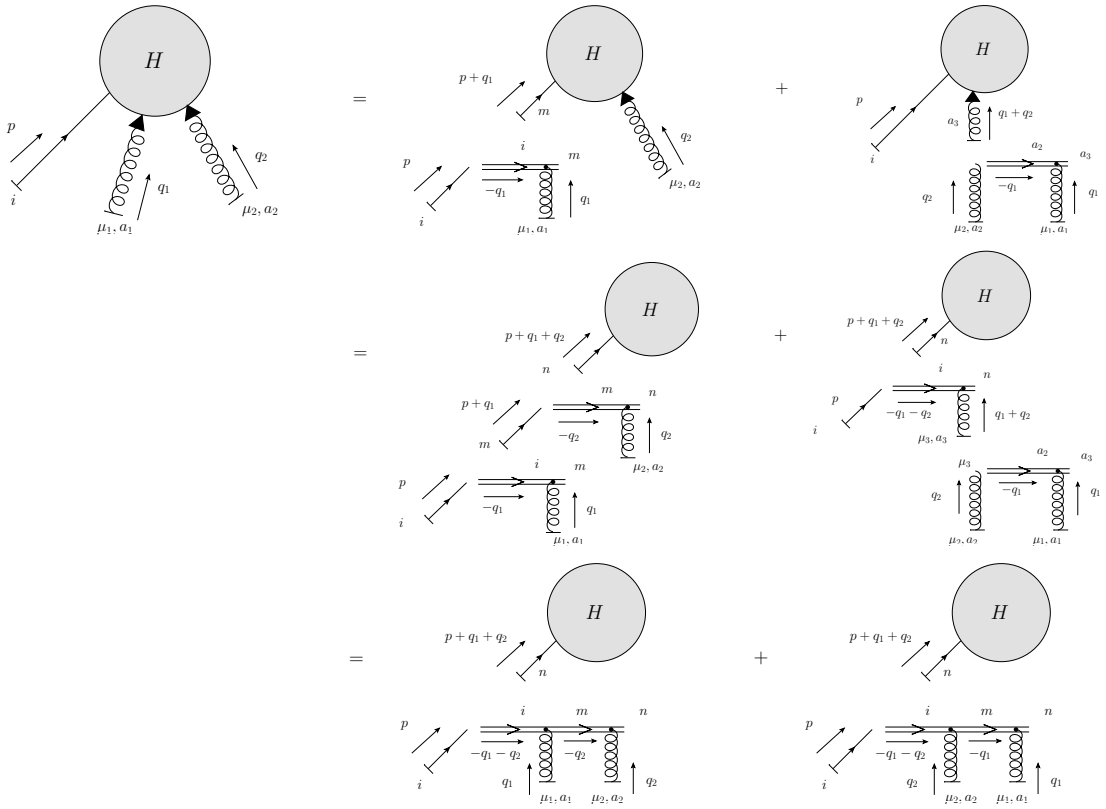

Figure 2.10: Factorisation of two longitudinally polarised gluon attachments.

We may therefore absorb the integrations over k^- and $k_\perp$ into the lower part of the diagram. The contractions over spinor or Lorentz indices of the two partons entering H may also be separated between upper and lower parts of the diagram (see [7] for details). The cross-section may then be written in a factorised form [7]:

$$\frac{d\sigma}{dQ^2 dx}(x, Q^2) = \sum_{a=\bar{q},q,g} \int_0^1 d\xi \; C^a(\xi, x, Q^2, \mu_F^2) \; a(\xi; \mu_F^2) \; . \tag{2.55}$$

Here ξ is the fraction of the proton momentum carried by the parton, a, entering the hard scattering (i.e. the k^+ integration), C^a is a coefficient function which contains all of the short distance physics and $a(\xi; \mu_F^2)$ is a parton distribution function (pdf). The pdfs contain all of the collinear divergences associated with the jet sub-diagram and may be defined in terms of matrix elements of quark and gluon operators and Wilson lines. They also depend on an arbitrary scale, known as the factorisation scale, μ_F. We shall discuss their definitions, properties and

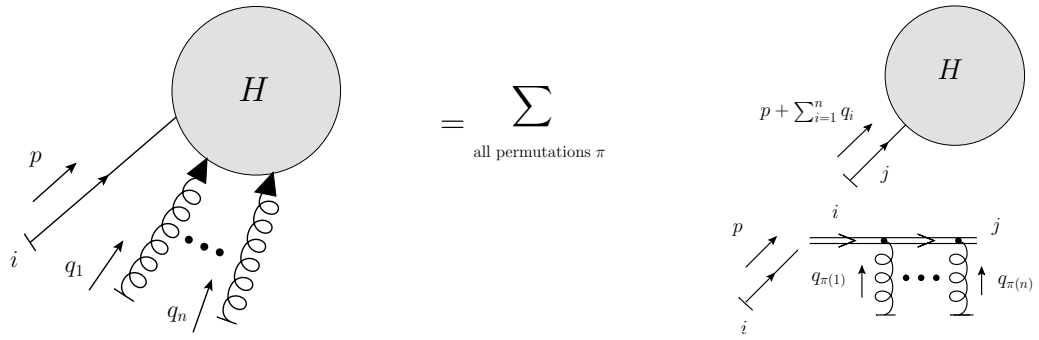

Figure 2.11: General form of factorisation for any number of collinear gluons attached to the hard scattering sub-diagram.

behaviour with respect to μ_F in the next section.

2.5 Parton distribution functions

2.5.1 Pdf definitions

First we introduce the generalised (skewed) pdfs, which we shall have need of subsequently (see for example [17]):

$$H_q(\xi,\eta;\mu_F^2) = \frac{1}{\sqrt{1-\eta^2}}\frac{1}{2}\sum_\sigma \int \frac{dz^-}{2\pi} e^{i\xi z^- p^+} \langle p_2,\sigma|\,\bar\psi(-z^-)[-z^-,z^-]\gamma^+\psi(z^-)\,|p_1,\sigma\rangle \tag{2.56}$$

$$H_g(\xi,\eta;\mu_F^2) = \frac{1}{\sqrt{1-\eta^2}}\frac{1}{2}\sum_\sigma \frac{4}{p^+} \times \int \frac{dz^-}{2\pi} e^{i\xi z^- p^+} \langle p_2,\sigma|\,G_a^{+\mu}(-z^-)[-z^-,z^-]_{ab} G_{b\mu}{}^{+}(z^-)\,|p_1,\sigma\rangle \tag{2.57}$$

where

$$p = p_1 + p_2\ , \tag{2.58}$$

$$\eta = \frac{p_1^+ - p_2^+}{p^+} \tag{2.59}$$

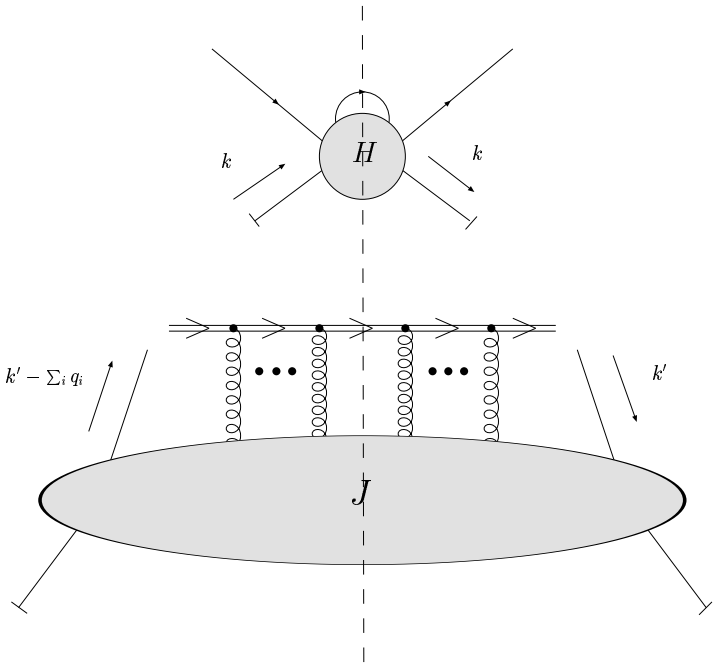

Figure 2.12: Factorisation of collinear gluons in inclusive DIS.

and σ labels the proton's spin. We may also define an anti-quark pdf, by:

$$H_{\bar{q}}(\xi, \eta; \mu_F^2) = -H_q(-\xi, \eta; \mu_F^2) \; . \tag{2.60}$$

In turn, these generalised pdfs are related to the standard pdfs, appearing in equation (2.55), when the proton states have equal momenta [17]:

$$H_q(\xi, 0; \mu_F^2) = q(\xi; \mu_F^2)\Theta(\xi) - \bar{q}(-\xi; \mu_F^2)\Theta(-\xi) \; , \tag{2.61}$$

$$H_g(\xi, 0; \mu_F^2) = \xi g(\xi; \mu_F^2)\Theta(\xi) - \xi g(-\xi; \mu_F^2)\Theta(-\xi) \; . \tag{2.62}$$

The factorisation scale, μ_F, arises as a result of renormalising the above matrix elements and essentially determines "how collinear" a parton must be in order to be included in the pdfs. Note that this approach of defining pdfs in terms of matrix elements of operators and then dealing with their ultraviolet behaviour using renormalisation, is entirely conventional. The study of infrared divergences presented in the previous sections applies only *at* the pinch surface. The definitions of the jet and hard functions away from this region is a matter of choice.

The cross-section of course, cannot depend on μ_F and so any variation in $a(x;\mu_F^2)$ due to varying μ_F must be compensated by a variation of C^a. Since C^a is perturbatively calculable, so is the variation of $a(x;\mu_F^2)$ with μ_F, as we now discuss.

2.5.2 Pdf evolution

As we stated in the previous section, the variation of the pdfs with factorisation scale, or evolution, is calculable in perturbation theory and is given by the following set of equations [17]:

$$\frac{d}{d\ln\mu_F}\begin{pmatrix} H_q(\xi,\eta;\mu_F^2) \\ H_g(\xi,\eta;\mu_F^2) \end{pmatrix} = -\int_{-1}^{1} d\xi' \begin{pmatrix} \sum\limits_{q'=q_i,\bar{q}_i} K^{qq}\delta^{qq'} & K^{qg} \\ \sum\limits_{q'=q_i,\bar{q}_i} K^{gq'} & K^{gg} \end{pmatrix} \begin{pmatrix} H_{q'}(\xi',\eta;\mu_F^2) \\ H_g(\xi',\eta;\mu_F^2) \end{pmatrix} \tag{2.63}$$

where

$$K^{ab} \equiv K^{ab}\left(\frac{\eta+\xi}{2},\frac{\eta-\xi}{2}\Big|\frac{\eta+\xi'}{2},\frac{\eta-\xi'}{2}\right) . \tag{2.64}$$

The evolution kernels, K^{ab}, have a perturbative expansion:

$$K^{ab}(x_1,x_2|y_1,y_2) = \sum_{n=1}^{\infty}\left(\frac{\alpha_s}{2\pi}\right)^n K^{ab}_{(n-1)}(x_1,x_2|y_1,y_2) \tag{2.65}$$

and the lowest order kernels are given by [17]

$$K^{qq}_{(0)}(x_1,x_2|y_1,y_2) = C_F\left[\frac{x_1}{x_1-y_1}\vartheta^0_{11}(x_1,x_1-y_1)+\frac{x_2}{x_2-y_2}\vartheta^0_{11}(x_2,x_2-y_2)\right.$$
$$\left.+\,\vartheta^0_{111}(x_1,-x_2,x_1-y_1)\right]_+ , \tag{2.66}$$

$$K^{qg}_{(0)}(x_1,x_2|y_1,y_2) = \frac{T_F}{2}\left[\vartheta^1_{112}(x_1,-x_2,x_1-y_1)+2\frac{x_1-y_1}{y_1y_2}\vartheta^0_{111}(x_1,-x_2,x_1-y_1)\right] \tag{2.67}$$

$$K^{gq}_{(0)}(x_1,x_2|y_1,y_2) = 2C_F\left[(y_1-y_2)\vartheta^0_{111}(x_1,-x_2,x_1-y_1)\right.$$
$$\left.+x_1x_2\vartheta^1_{111}(x_1,-x_2,x_1-y_1)\right] , \tag{2.68}$$

$$K^{gg}_{(0)}(x_1,x_2|y_1,y_2) = C_A\left[\frac{x_1}{y_1}\left[\frac{x_1}{x_1-y_1}\vartheta^0_{11}(x_1,x_1-y_1)\right]_+\right.$$
$$+\frac{x_2}{y_2}\left[\frac{x_2}{x_2-y_2}\vartheta^0_{11}(x_2,x_2-y_2)\right]_+ + 2\frac{x_1x_2+y_1y_2}{y_1y_2}\vartheta^0_{111}(x_1,-x_2,x_1-y_1)$$
$$\left.+\,2\frac{x_1x_2}{y_1y_2}\frac{x_1y_1+x_2y_2}{(x_1+x_2)^2}\vartheta^0_{11}(x_1,-x_2)+\left(\frac{1}{2}\frac{\beta_0}{C_A}+2\right)\delta(x_1-y_1)\right] , \tag{2.69}$$

where the generalised step function is defined as

$$\vartheta^k_{\alpha_1\cdots\alpha_j}(x_1,\ldots,x_j) = \int\frac{d\kappa}{2\pi i}\frac{\kappa^k}{\prod_{l=1}^j(x_l\kappa-1+i\varepsilon)^{\alpha_l}} \tag{2.70}$$

and the plus-distribution is given by

$$\left[\frac{x_1}{x_1-y_1}\vartheta^0_{11}(x_1,x_1-y_1)\right]_+ = \frac{x_1}{x_1-y_1}\vartheta^0_{11}(x_1,x_1-y_1)$$
$$-\,\delta(x_1-y_1)\int dx'_1\frac{x'_1}{x'_1-y_1}\vartheta^0_{11}(x'_1,x'_1-y_1) . \tag{2.71}$$

Note that our definitions of the kernels differ slightly from those of [17], in particular:

$$K^{qq}_{(0)} = K^{qq}_{(0)}|_{\,[17]} \qquad K^{qg}_{(0)} = \frac{1}{4n_f}K^{qg}_{(0)}|_{\,[17]}$$
$$K^{gq}_{(0)} = 2K^{gq}_{(0)}|_{\,[17]} \qquad K^{gg}_{(0)} = K^{gg}_{(0)}|_{\,[17]} . \tag{2.72}$$

In the forward ($\eta \to 0$) limit these kernels are related to the standard Altarelli-Parisi splitting functions:

$$K^{qq}_{(0)}\left(\frac{\xi}{2},-\frac{\xi}{2}\middle|\frac{\xi}{2z},-\frac{\xi}{2z}\right) = -\frac{2z}{|\xi|}P_{qq}(z)\Theta(z)\Theta(1-z)\ , \tag{2.73}$$

$$K^{qg}_{(0)}\left(\frac{\xi}{2},-\frac{\xi}{2}\middle|\frac{\xi}{2z},-\frac{\xi}{2z}\right) = -\frac{2z^2}{|\xi|\xi}P_{qg}(z)\Theta(z)\Theta(1-z)\ , \tag{2.74}$$

$$K^{gq}_{(0)}\left(\frac{\xi}{2},-\frac{\xi}{2}\middle|\frac{\xi}{2z},-\frac{\xi}{2z}\right) = -2z\ \mathrm{sgn}(\xi)P_{gq}(z)\Theta(z)\Theta(1-z)\ , \tag{2.75}$$

$$K^{gg}_{(0)}\left(\frac{\xi}{2},-\frac{\xi}{2}\middle|\frac{\xi}{2z},-\frac{\xi}{2z}\right) = -\frac{2z^2}{|\xi|}P_{gg}(z)\Theta(z)\Theta(1-z) \tag{2.76}$$

where the P_{ij} are as given in [18]. Equation (2.63) then becomes the DGLAP equation [19–22]:

$$\frac{da(\xi,\mu_F^2)}{d\ln\mu_F} = \frac{\alpha_s}{\pi}\sum_{b=q,\bar{q},g}\int_0^1\frac{dz}{z}P_{ab}(z)b(\xi/z,\mu_F^2)\ . \tag{2.77}$$

We shall now discuss how these results are derived in perturbation theory, first demonstrating how the splitting kernels arise by treating the cases of $K^{qq}_{(0)}$ and $K^{gq}_{(0)}$ in detail. We shall then use this knowledge to derive the evolution equation (2.63).

2.5.3 Derivation of the splitting kernels $K^{qq}_{(0)}$ and $K^{gq}_{(0)}$

Consider the factorised amplitude, A, shown in figure 2.13, where p_1 and p_2 are in the plus lightcone direction, but we do not require $p_1 = p_2$[6]. The amplitude may be written in factorised form as

$$A = \sqrt{1-\eta^2}\ \frac{p^+}{2}\sum_a\int d\xi\ C^a\left(\frac{\eta+\xi}{2},\frac{\eta-\xi}{2};Q_0^2\right)H_a(\xi,\eta;Q_0^2) \tag{2.78}$$

with p^+ and η given by equations (2.58) and (2.59) respectively and

$$k_1^+ = \frac{(\xi+\eta)}{2}p^+\ . \tag{2.79}$$

[6]We shall see an example of an amplitude which is expected to factorise in this way in chapter 4.

As previously discussed, we may study the behaviour of H_a with respect to the factorisation scale, Q_0, by studying the Q_0 dependence of the coefficient function, C^a. To do so, we consider the limit of very small Q_0. In this limit, the coefficient function will contain large logarithms in Q_0, which correspond to would be collinear divergences, factorised into the pdfs. We work in the approximation that we require one of these large logarithms at each perturbative order, such that the smallness of α_s is compensated. We may compute these "leading logarithms" by taking the partons entering C^a off-shell, with $k_i^2 = -Q_0^2 < 0$. In this case, we may write:

$$k_i^\mu = y_i p^\mu + \frac{k_i^2}{y_i s}\bar{p}^\mu \tag{2.80}$$

$$s = 2p \cdot \bar{p} \tag{2.81}$$

where $\bar{p}$ is a light-like four-vector in the minus lightcone direction.

We shall now treat C^q in detail and then extend our results to anti-quarks and gluons. Consider C_n^q, the $\mathcal{O}(\alpha_s^n)$ contribution to C^q. Each loop in C_n^q must generate a logarithm in our approximation, which means that the virtual correction with the lowest transverse momentum must attach to at least one of the external quarks. Neglecting a lowest order term then, the diagrams contributing to C_n^q are those shown in figure 2.14.

To understand under what conditions this virtual correction may produce a logarithm, we may apply the techniques described in the previous sections. The lowest transverse momentum emission effectively plays the rôle of the jet subdiagram, with the rest of the diagram, which involves lines much further off-shell, playing the rôle of the hard vertex. In line with our discussion of the DIS case then, the gluons in figures 2.14(b) and 2.14(c) may be treated as longitudinally polarised and so may be factorised onto eikonal lines, as shown in figure 2.15 for diagram 2.14(b).

The coefficient function is obtained from each set of Feynman diagrams at

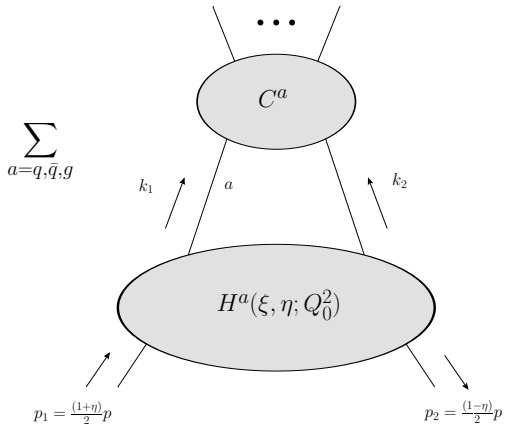

Figure 2.13: Factorised amplitude for the scattering of two collinear hadrons.

$\mathcal{O}(\alpha_s^n)$, G_n^q, by the following expression

$$C_n^q = \frac{1}{2N}\sum_i \mathrm{Tr}\left[\frac{\gamma^-}{2}G_n^q\right] \tag{2.82}$$

where i labels the colour of the incoming quark and the trace is taken over spinor indices. Note that we do not include external quark spinors in G_n^q. Although we are working at the amplitude level, the above expression includes a sum over quark spins and colours; let us now discuss how this comes about. The colour sum is easily understood, it is simply (including the factor of N^{-1}) the colour-singlet projector, necessary because the incoming and outgoing hadrons are colourless. The trace with γ^- on the other hand, follows from a factorisation of the spin structure connecting the hard and jet sub-diagrams in the analysis of the previous sections. Consider figure 2.12, for the case of a quark entering the hard vertex. The jet function, J, and the hard vertex, H, are connected by a trace over spinor indices, $J_{\alpha_1\alpha_2}H_{\alpha_1\alpha_2}$. However, J only depends on momenta in the plus lightcone direction, so we have: $J_{\alpha_1\alpha_2} = \gamma^-\hat{J}$. Using $\mathrm{Tr}[\gamma^+\gamma^-] = 4$, we may then write

$$J_{\alpha_1\alpha_2}H_{\alpha_1\alpha_2} = \mathrm{Tr}\left[\frac{\gamma^+}{2}J\right]\mathrm{Tr}\left[\frac{\gamma^-}{2}H\right] \ . \tag{2.83}$$

Thus we see the origin of the trace with γ^-, appearing in the definition of the coefficient function. The additional factor of 1/2 in equation (2.82) is simply a normalisation convention.

Returning to the task in hand, the diagrams of figure 2.14 (after factorisation onto eikonal lines) give the following contributions

$$C_n^q|_{2.14(a)} = \frac{-2ig^2C_F}{4N}\sum_j \int \frac{d^4q}{(2\pi)^4} \frac{\mathrm{Tr}\left[\gamma^- \not{k}_2' G_{n-1}^q(x_1,x_2)\not{k}_1'\right]}{[k_1'^2+i\varepsilon][k_2'^2+i\varepsilon][q^2+i\varepsilon]} , \tag{2.84}$$

$$C_n^q|_{2.14(b)} = \frac{-ig^2C_F}{4N}\sum_j \int \frac{d^4q}{(2\pi)^4} \frac{\mathrm{Tr}\left[\gamma^- (G_{n-1}^q(x_1,x_2) - G_{n-1}^q(y_1,y_2))\not{k}_1'\not{\bar{p}}\right]}{q\cdot\bar{p}[k_1'^2+i\varepsilon][q^2+i\varepsilon]} , \tag{2.85}$$

$$C_n^q|_{2.14(c)} = \frac{ig^2C_F}{4N}\sum_j \int \frac{d^4q}{(2\pi)^4} \frac{\mathrm{Tr}\left[\gamma^- (G_{n-1}^q(x_1,x_2) - G_{n-1}^q(y_1,y_2))\not{k}_2'\not{\bar{p}}\right]}{q\cdot\bar{p}[k_2'^2+i\varepsilon][q^2+i\varepsilon]} , \tag{2.86}$$

$$C_n^q|_{2.14(d)} = \frac{ig^2T_F}{4N}\sum_a \int \frac{d^4q}{(2\pi)^4} \frac{\mathrm{Tr}\left[\gamma^-\gamma^\nu \not{q}\gamma^\mu\right] G_{n-1\mu\nu}^g(x_1,x_2)}{[k_1'^2+i\varepsilon][k_2'^2+i\varepsilon][q^2+i\varepsilon]} , \tag{2.87}$$

$$C_n^q|_{2.14(e)} = \frac{1}{4N}\sum_i \mathrm{Tr}\left[\gamma^- G_{n-1}^q(y_1,y_2)\right]\Sigma(k_1) , \tag{2.88}$$

where x_1 and x_2 are, respectively, the momentum fractions of k_1' and k_2' in the p direction. The self energy is given, in dimensional regularisation, by (see for example [23]):

$$\Sigma(k_1) = \frac{C_F g^2 (Q_0^2)^{-\epsilon}}{(4\pi)^{d/2}} \frac{(d-2)}{(d-3)(d-4)} \frac{\Gamma(1+\epsilon)\Gamma(1-\epsilon)^2}{\Gamma(1-2\epsilon)} \tag{2.89}$$

where $d = 4-2\epsilon$ is the space-time dimension. We now proceed to approximate these contributions, such that we keep only the part enhanced by a logarithm. Firstly, we drop the small virtuality Q_0 in the numerators of equations (2.84-2.87), treating k_1 and k_2 as massless. Next we decompose q in terms of Sudakov components:

$$q^\mu = \alpha p^\mu + \beta\bar{p}^\mu + q_\perp , \tag{2.90}$$

$$q_\perp \cdot p = q_\perp \cdot \bar{p} = 0 , \tag{2.91}$$

$$q_\perp^2 = -\boldsymbol{q}_\perp^2 , \tag{2.92}$$

$$d^4q = \frac{s}{2} d^2q_\perp d\alpha d\beta . \tag{2.93}$$

We may then treat q as a jet momentum and count powers in β and $q_\perp$, according to the scalings of equation (2.15), dropping terms which do not correspond to a

logarithmic divergence. The numerators of diagrams 2.14(a)-2.14(c) thus become

$$\mathrm{Tr}\left[\gamma^- \not{k}_2' G_{n-1}(x_1, x_2) \not{k}_1'\right] \approx -\boldsymbol{q}_\perp^2 \mathrm{Tr}\left[\gamma^- G_{n-1}(x_1, x_2)\right] \ , \tag{2.94}$$

$$\mathrm{Tr}\left[\gamma^-(G_{n-1}(x_1, x_2) - G_{n-1}(y_1, y_2)) \not{k}_i' \not{p}\right] \approx x_i s \mathrm{Tr}\left[\gamma^-(G_{n-1}(x_1, x_2) - G_{n-1}(y_1, y_2))\right] \ . \tag{2.95}$$

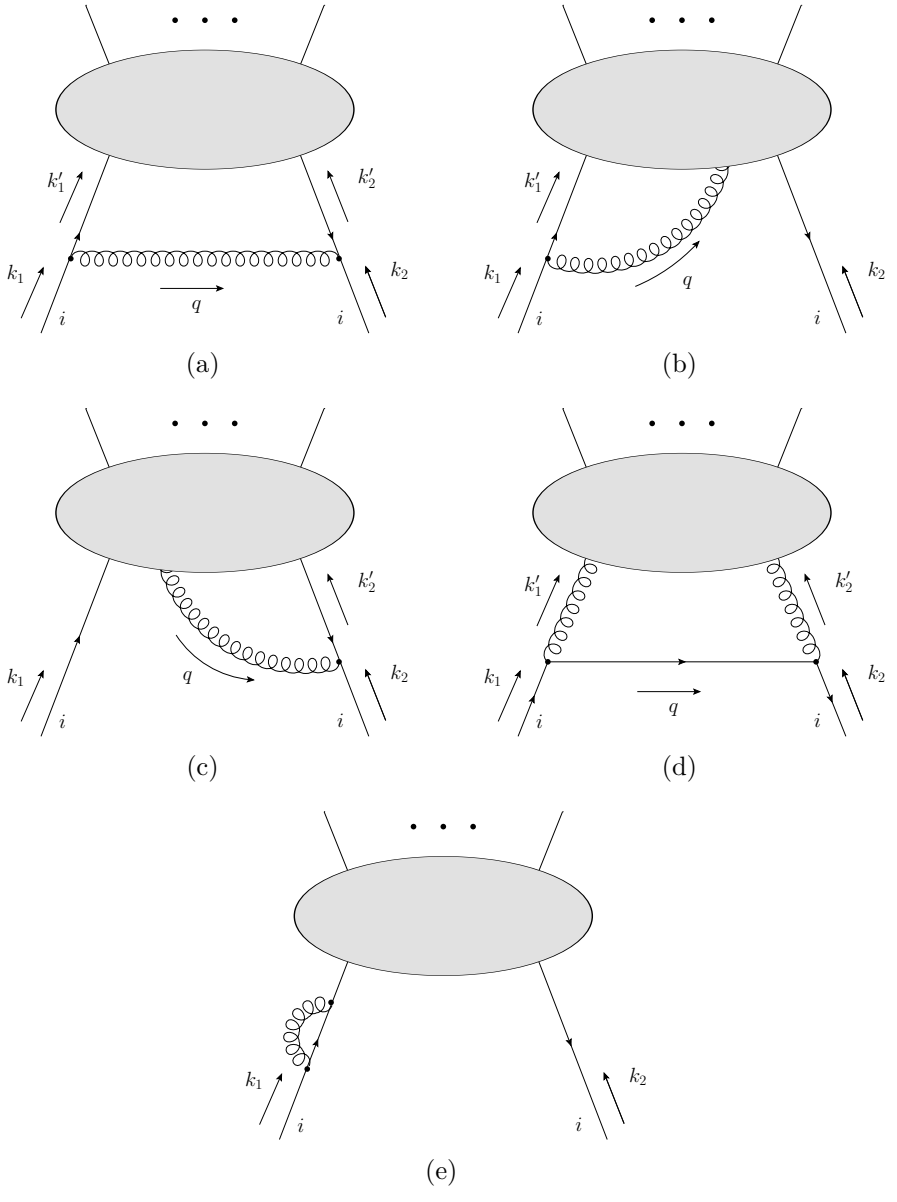

Figure 2.14: The diagrams contributing to C_n^q in the leading logarithm approximation.

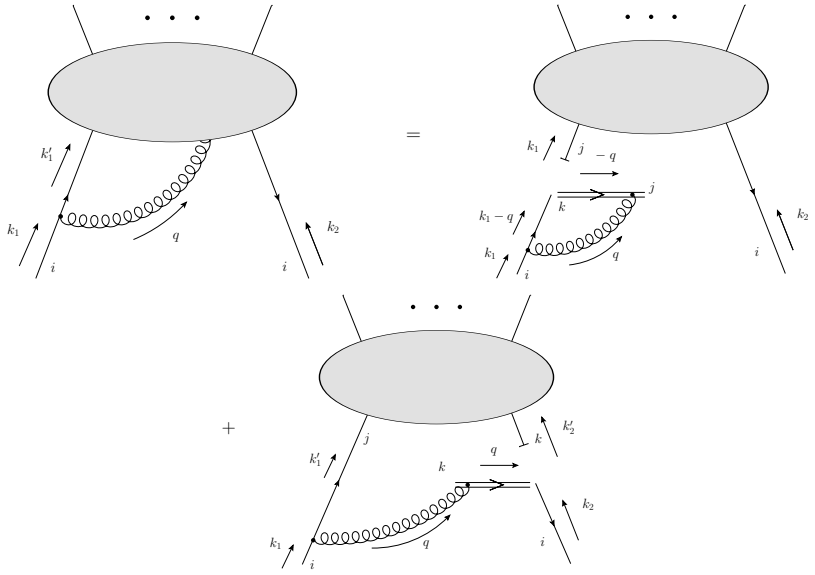

Figure 2.15: Factorisation onto an eikonal line for one of the diagrams contributing to C_n^q.

Diagram 2.14(d) requires a little more work. First, evaluating the trace, we find

$$\mathrm{Tr}\left[\gamma^-\gamma^\nu \not{q}\gamma^\mu\right] = \frac{4}{p^+}\left(p^\mu q^\nu + p^\nu q^\mu - g^{\mu\nu}\frac{\beta s}{2}\right) . \tag{2.96}$$

Now note that the Ward identity implies the following

$$k_1'^\mu G^g_{n-1\mu\nu} = 0 , \tag{2.97}$$

$$k_2'^\nu G^g_{n-1\mu\nu} = 0 , \tag{2.98}$$

which, when combined with the requirement of a large logarithm, allows us to make the following replacement

$$p^\mu q^\nu + p^\nu q^\mu - g^{\mu\nu}\frac{\beta s}{2} = \frac{(y_2-y_1)}{x_1x_2}(\beta\bar{p}^\mu + q_\perp^\mu)(\beta\bar{p}^\nu + q_\perp^\nu) - g^{\mu\nu}\frac{\beta s}{2} \tag{2.99}$$

$$\approx -\frac{g_\perp^{\mu\nu}}{2}\left(\frac{\boldsymbol{q}_\perp^2(y_2-y_1)}{x_1x_2} + \beta s\right) , \tag{2.100}$$

where the transverse metric is given by

$$g_\perp^{\mu\nu} = g^{\mu\nu} - \frac{2}{s}\left(p^\mu\bar{p}^\nu + \bar{p}^\mu p^\nu\right) . \tag{2.101}$$

Here we also made the replacement

$$q_\perp^\mu q_\perp^\nu \to -\frac{g_\perp^{\mu\nu}\boldsymbol{q}_\perp^2}{2}\ , \tag{2.102}$$

which is valid, since the factor of G_{n-1}^g multiplying it cannot depend on $q_\perp$ if we require a logarithm.

Next we deal with the denominators:

$$\begin{aligned} k_1'^2 + i\varepsilon &= -x_1\beta s - \frac{x_1}{y_1}Q_0^2 - \boldsymbol{q}_\perp^2 + i\varepsilon \\ &\approx l^2\left(\frac{-x_1\beta s}{l^2} - 1 + i\varepsilon\right) \end{aligned} \tag{2.103}$$

$$\begin{aligned} k_2'^2 + i\varepsilon &= x_2\beta s - \frac{x_2}{y_2}Q_0^2 - \boldsymbol{q}_\perp^2 + i\varepsilon \\ &\approx l^2\left(\frac{x_2\beta s}{l^2} - 1 + i\varepsilon\right) \end{aligned} \tag{2.104}$$

where $l^2 = \boldsymbol{q}_\perp^2 + Q_0^2$. Here we have assumed $x_i/y_i \sim \mathcal{O}(1)$ and used the fact that logarithms of Q_0 or Q_0 multiplied by an order one number are equivalent in the leading logarithm approximation. Now, changing variables from α and β to

$$\kappa = \frac{s\beta}{l^2} \tag{2.105}$$

$$\xi = y_1 - y_2 - 2\alpha \tag{2.106}$$

and rewriting the results in terms of the generalised step functions, we obtain

$$C_n^q|_{2.14(a)} \approx -\frac{\alpha_s}{4\pi}C_F\int_{Q_0^2}\frac{dl^2}{l^2}\int d\xi\ \vartheta_{111}^0(x_1,-x_2,x_1-y_1)C_{n-1}^q(x_1,x_2)\ , \tag{2.107}$$

$$C_n^q|_{2.14(b)} \approx -\frac{\alpha_s}{4\pi}C_F\int_{Q_0^2}\frac{dl^2}{l^2}\int d\xi\left[\frac{x_1}{x_1-y_1}\vartheta_{11}^0(x_1,x_1-y_1)\right]_+ C_{n-1}^q(x_1,x_2)\ , \tag{2.108}$$

$$C_n^q|_{2.14(c)} \approx -\frac{\alpha_s}{4\pi}C_F\int_{Q_0^2}\frac{dl^2}{l^2}\int d\xi\left[\frac{x_2}{x_2-y_2}\vartheta_{11}^0(x_2,x_2-y_2)\right]_+ C_{n-1}^q(x_1,x_2)\ , \tag{2.109}$$

$$\begin{aligned} C_n^q|_{2.14(d)} \approx -\frac{\alpha_s}{4\pi}C_F\int_{Q_0^2}\frac{dl^2}{l^2}\int d\xi\ 2\big((y_1-y_2)\vartheta_{111}^0(x_1,-x_2,x_1-y_1) \\ +x_1x_2\vartheta_{111}^1(x_1,-x_2,x_1-y_1)\big)\,C_{n-1}^g(x_1,x_2)\ , \end{aligned} \tag{2.110}$$

where

$$C_n^g(x_1,x_2)=\left(-\frac{g_\perp^{\mu\nu}}{2}\right)\frac{1}{(-x_1x_2p^+)}\sum_a\frac{1}{N^2-1}G^g_{n\mu\nu}\ . \tag{2.111}$$

Note that in the plus-distribution the soft, $1/\alpha$, divergences cancel. This is a cancellation between the two types of eikonal diagram shown in figure 2.15. Were we computing the logarithmic corrections to these diagrams with a cut and with $k_2=-k_1$ (an amplitude squared), then the two contributions would be classified as real and virtual respectively. The cancellation then is simply a manifestation of the Bloch-Nordsieck theorem.

Next, the self-energy contribution, after $\overline{\rm MS}$ subtraction, may be written

$$C_n^q|_{2.14(e)}\approx\frac{\alpha_s}{4\pi}C_F\int_{Q_0^2}^{\mu_R^2}\frac{dl^2}{l^2}\int d\xi\ \vartheta^0_{111}(x_1,-x_2,x_1-y_1)C^q_{n-1}(y_1,y_2)\ , \tag{2.112}$$

where μ_R is the renormalisation scale and we have kept only the logarithmic term.

Putting all of these pieces together then and including incoming anti-quarks and gluons, we find the following result

$$\begin{aligned}C_n^{a_0}\left(\frac{\eta+\xi_0}{2},\frac{\eta-\xi_0}{2};Q_0^2\right)\approx-\sum_{a_1=q,\bar q,g}\int_{Q_0^2}^{l_2^2}\frac{dl_1^2}{l_1^2}\frac{\alpha_s(l_1^2)}{4\pi}\\ \times\int d\xi_1\ K^{a_1a_0}_{(0)}\left(\frac{\eta+\xi_1}{2},\frac{\eta-\xi_1}{2}\Big|\frac{\eta+\xi_0}{2},\frac{\eta-\xi_0}{2}\right)\\ \times C^{a_1}_{n-1}\left(\frac{\eta+\xi_1}{2},\frac{\eta-\xi_1}{2};Q_0^2\right)\ .\end{aligned} \tag{2.113}$$

In writing the above we made the change $l\to l_1$ in addition to two further alterations. Firstly, the upper cutoff on the l_1^2 integration is now l_2^2. This variable is the exact analogue of l_1, but for the first emission contained in C_{n-1}[7]. This cutoff arises either by a choice of renormalisation scale or kinematically, in precisely the same way as Q_0 entered as a lower cutoff. The choice of this renormalisation scale induces the other change in (2.113), namely that α_s now runs with l_1.

[7]If $n=1$, then l_2 is replaced by the hard scale of the tree-level process, Q.

2.5.4 Derivation of the evolution equation

We now discuss how the logarithmically enhanced corrections studied in the previous section lead to the evolution equation. Firstly, we may iterate equation (2.113) until we are left with the tree-level process, C_0:

$$C_n^{a_0}\left(\frac{\eta+\xi_0}{2},\frac{\eta-\xi_0}{2};Q_0^2\right)\approx\left(-\sum_{a_1}\int_{Q_0^2}^{l_2^2}\frac{dl_1^2}{l_1^2}\frac{\alpha_s(l_1^2)}{4\pi}\int d\xi_1\;K_{(0)}^{a_1a_0}\right)\cdots\left(-\sum_{a_n}\int_{Q_0^2}^{Q^2}\frac{dl_n^2}{l_n^2}\frac{\alpha_s(l_n^2)}{4\pi}\int d\xi_n\;K_{(0)}^{a_na_{n-1}}\right)\times C_0^{a_n}\left(\frac{\eta+\xi_n}{2},\frac{\eta-\xi_n}{2};Q_0^2\right) \tag{2.114}$$

Next, we introduce an arbitrary scale, $Q_0<\mu_F<Q$, by means of the following identity:

$$\prod_{k=1}^{n}\int_{Q_0^2}^{l_{k+1}^2}dl_k^2=\sum_{i=0}^{n}\left(\int_{Q_0^2}^{l_2^2}dl_1^2\cdots\int_{Q_0^2}^{\mu_F^2}dl_i^2\right)\left(\int_{\mu_F^2}^{\tilde{l}_2^2}d\tilde{l}_1^2\cdots\int_{\mu_F^2}^{Q^2}d\tilde{l}_{n-i}^2\right) \tag{2.115}$$

where $\tilde{l}_j=l_{j+i}$. Summing over n to obtain the full coefficient functions and interchanging the sums on i and n, we may write:

$$C^{a_0}\left(\frac{\eta+\xi_0}{2},\frac{\eta-\xi_0}{2};Q_0^2\right)\approx\sum_{i=0}^{\infty}\prod_{j=1}^{i}\left(-\sum_{a_j}\int_{Q_0^2}^{l_{j+1}^2}\frac{dl_j^2}{l_j^2}\frac{\alpha_s(l_j^2)}{4\pi}\int d\xi_j\times K_{(0)}^{a_ja_{j-1}}\left(\frac{\eta+\xi_j}{2},\frac{\eta-\xi_j}{2}\middle|\frac{\eta+\xi_{j-1}}{2},\frac{\eta-\xi_{j-1}}{2}\right)\right)\times C^{a_i}\left(\frac{\eta+\xi_i}{2},\frac{\eta-\xi_i}{2};\mu_F^2\right) \tag{2.116}$$

where $l_{i+1}^2=\mu_F^2$. We now substitute this expression into equation (2.78), arriving at:

$$\begin{aligned}A&=\sqrt{1-\eta^2}\,\frac{p^+}{2}\sum_{a_0}\int d\xi_0\;C^{a_0}\left(\frac{\eta+\xi_0}{2},\frac{\eta-\xi_0}{2};Q_0^2\right)H_{a_0}(\xi_0,\eta;Q_0^2)\\&=\sqrt{1-\eta^2}\,\frac{p^+}{2}\sum_{a}\int d\xi\;C^{a}\left(\frac{\eta+\xi}{2},\frac{\eta-\xi}{2};\mu_F^2\right)H_a(\xi,\eta;\mu_F^2)\end{aligned} \tag{2.117}$$

where:

$$H_a(\xi,\eta;\mu_F^2) = H_a(\xi,\eta;Q_0^2) + \sum_{a_0}\int d\xi_0\; H_{a_0}(\xi_0,\eta;Q_0^2)$$
$$\times\sum_{i=1}^{\infty}\left(-\prod_{j=1}^{i-1}\sum_{a_j}\int_{Q_0^2}^{l_{j+1}^2}\frac{dl_j^2}{l_j^2}\frac{\alpha_s(l_j^2)}{4\pi}\int d\xi_j\; K_{(0)}^{a_j a_{j-1}}\right)$$
$$\times\left(-\int_{Q_0^2}^{\mu_F^2}\frac{dl_i^2}{l_i^2}\frac{\alpha_s(l_i^2)}{4\pi}K_{(0)}^{a a_{i-1}}\left(\frac{\eta+\xi}{2},\frac{\eta-\xi}{2}\middle|\frac{\eta+\xi_{i-1}}{2},\frac{\eta-\xi_{i-1}}{2}\right)\right) \tag{2.118}$$

It is a simple matter to show that this function does indeed satisfy the evolution equation (2.63).

2.5.5 BFKL corrections

The derivation of the large logarithmic corrections in the previous sections must be modified if the momentum fractions carried forward along the emission chain, x_i, become very small. If this is the case, we see that equations (2.103) and (2.104) become independent of Q_0^2, thus removing the transverse momentum ordering which generated our large logarithms. However, in this region, strongly ordered momentum fraction integrals may generate large logarithms instead. These corrections may also be organised into the form of a ladder and a corresponding integral equation derived, known as the BFKL equation [24–27]. We refer the reader to [28] for more details.

2.6 Dealing with soft corrections

2.6.1 Factoring soft gluons from jets

The cancellation of the soft region in DIS was facilitated by a sum over cuts. After this sum we saw that the soft diagram could only attach to a single jet and/or

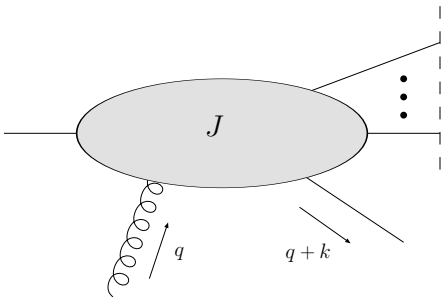

Figure 2.16: A soft gluon attachment to a jet.

the hard vertex, both of which ensured a suppression in the power counting. Unfortunately, such a simple mechanism does not hold when one considers processes with more than one hadron in the initial state. In such cases, the soft diagram may connect jets moving in different directions and thus avoid any suppression. In order to demonstrate the cancellation of the soft region in this case, we must first decouple the soft attachments from the jets. We shall now describe how one accomplishes this.

Consider the diagram shown in figure 2.16. As before, J is a jet of collinear partons, which we take to be moving in the plus direction. Attached to this, in all possible ways, is a soft gluon, q. In addition, one parton, $k + q$, enters the hard vertex. Now note that, by power counting, J depends only on q^- and none of the other components of q. In addition, as we proved in section 2.4.3, all free Lorentz indices of the jet due to soft gluons are proportional to a vector in the jet direction. Thus we may write

$$J^\mu(q) = v^\mu u \cdot J(\tilde{q}) = v^\mu \frac{\tilde{q} \cdot J(\tilde{q})}{q \cdot v} \tag{2.119}$$

where, $v^\mu = \delta^\mu_+$, $u^\mu = \delta^\mu_-$, $\tilde{q}^- = q^-$ and $\tilde{q}^+ = \tilde{q}_\perp = 0$. Once again we have rewritten the diagram in terms of the attachment of a longitudinally polarised gluon, this time moving in the minus direction. We may again apply the Ward identity, however, in contrast to the factorisation of collinear lines, we do have a sum over a complete set of diagrams. This time though, the parton entering the

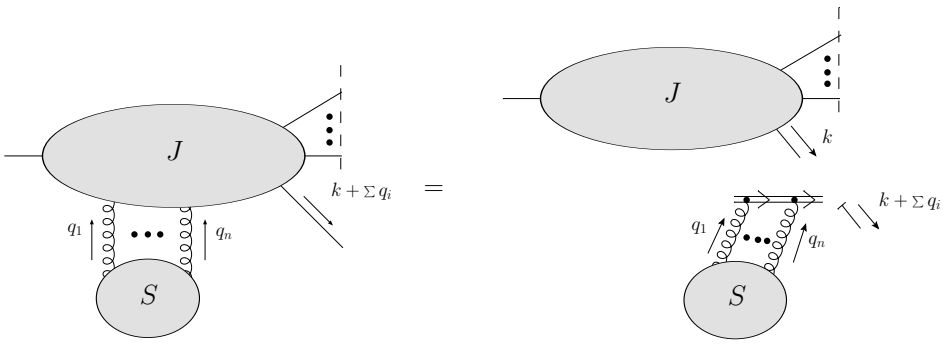

Figure 2.17: Factorisation of soft gluons onto an eikonal line.

hard vertex is off-shell and so the sum does not vanish. This non-vanishing term may then be written as an attachment onto an eikonal line. Note though that, in this case, the eikonal line is moving in the plus direction and so its Feynman rules are obtained from those of figure 2.9 by replacing u with v.

Generalising this procedure to more than one soft gluon is straightforward [9] and the result is displayed in figure 2.17. The soft and jet diagrams are now kinematically independent and one may show that the sum of cuts of the soft diagram is free of divergences [9].

Chapter 3

Aspects of fixed order calculations

3.1 Computing tree level amplitudes (The Weyl-van der Waerden formalism)

3.1.1 Overview of the formalism

In this chapter we introduce some of the techniques we shall use to perform fixed order calculations at tree and one loop-level. We begin with a description of a technique, known as the Weyl-van der Waerden (WvdW) formalism, which allows one to calculate tree-level processes at the amplitude level [29, 30]. This approach is more efficient than the technique of first squaring the amplitude and then summing over spins, in order to exploit trace theorems. In addition, the central exclusive gluino production process, considered in chapter 5, requires a sum over spins at the amplitude level, making this approach particularly well suited. In the remainder of this section we shall follow closely the presentation of [29].

The formalism proceeds via the following steps:

- Rewrite all four-vectors and spinor wave-functions making up the amplitude in terms of two-spinors (defined in the next section).
- Represent all gauge boson polarisation vectors in terms of two-spinors.
- Choose a gauge to simplify the calculation.

3.1.2 Two-spinor notation and conventions

The first step is to rewrite the amplitude in terms of left and right-handed 'two-spinors', denoted ψ_α and $\psi^{\dot{\alpha}}$ respectively. These are two-component objects which transform under the $(\frac{1}{2}, 0)$ and $(0, \frac{1}{2})$ representations of the Lorentz group respectively.

The two types of spinor are related by complex conjugation (indicated by a dotted index) and contractions with the two-dimensional antisymmetric tensor:

$$\psi_{\dot{\alpha}} = (\psi_\alpha)^* \qquad \psi^\alpha = \epsilon^{\alpha\beta}\psi_\beta \qquad \psi_{\dot{\alpha}} = \epsilon_{\dot{\alpha}\dot{\beta}}\psi^{\dot{\beta}} \tag{3.1}$$

$$\epsilon^{\alpha\beta} = \epsilon^{\dot{\alpha}\dot{\beta}} = \epsilon_{\alpha\beta} = \epsilon_{\dot{\alpha}\dot{\beta}} = \begin{pmatrix} 0 & +1 \\ -1 & 0 \end{pmatrix} . \tag{3.2}$$

Furthermore, one may construct a spinor product, $\langle\phi\psi\rangle$, which has the following properties:

$$\langle\phi\psi\rangle = \phi_\alpha\psi^\alpha = \phi_\alpha\epsilon^{\alpha\beta}\psi_\beta \tag{3.3}$$

$$\langle\phi\psi\rangle^* = \phi_{\dot{\alpha}}\psi^{\dot{\alpha}} = \phi_{\dot{\alpha}}\epsilon^{\dot{\alpha}\dot{\beta}}\psi_{\dot{\beta}} \tag{3.4}$$

$$\langle\phi\psi\rangle = -\langle\psi\phi\rangle \tag{3.5}$$

$$\langle\phi_1\phi_2\rangle\langle\phi_3\phi_4\rangle + \langle\phi_1\phi_3\rangle\langle\phi_4\phi_2\rangle + \langle\phi_1\phi_4\rangle\langle\phi_2\phi_3\rangle = 0 \tag{3.6}$$

where the final expression is known as the Schouten identity. It is the goal of the WvdW technique to represent the amplitude solely in terms of these objects and four-vector products.

Four-vectors contracted with Dirac matrices may also be incorporated, by using the Weyl representation:

$$\gamma^\mu = \begin{pmatrix} 0 & \sigma^\mu_{\alpha\dot\beta} \\ \sigma^{\mu,\dot\alpha\beta} & 0 \end{pmatrix} \qquad\qquad \gamma^5 = \begin{pmatrix} 1 & 0 \\ 0 & -1 \end{pmatrix} \tag{3.7}$$

where

$$\sigma^{\mu,\dot\alpha\beta} = (1, \boldsymbol{\sigma}) \tag{3.8}$$

$$\sigma^\mu_{\dot\alpha\beta} = \epsilon_{\dot\alpha\dot\gamma}\epsilon_{\beta\delta}\sigma^{\mu,\dot\gamma\delta} = (1, -\boldsymbol{\sigma}^*) \tag{3.9}$$

$$\sigma^\mu_{\alpha\dot\beta} = (\sigma^\mu_{\dot\alpha\beta})^* \tag{3.10}$$

$$\sigma^{\mu,\alpha\dot\beta} = (\sigma^{\mu,\dot\alpha\beta})^* \tag{3.11}$$

and $\boldsymbol{\sigma}$ is a vector of the standard Pauli matrices. This allows us to write contractions between Dirac matrices and four-vectors in terms of the following object

$$k_{\dot\alpha\beta} = \sigma^\mu_{\dot\alpha\beta}k_\mu = \begin{pmatrix} k^0 + k^3 & k^1 + ik^2 \\ k^1 - ik^2 & k^0 - k^3 \end{pmatrix} . \tag{3.12}$$

Furthermore, the identity

$$\sigma^\mu_{\dot\alpha\beta}\sigma^{\nu,\dot\alpha\beta} = 2g^{\mu\nu} \tag{3.13}$$

may be used to relate traces of the matrices (3.12) to four-vector products:

$$k_{\dot\alpha\beta}p^{\dot\alpha\beta} = 2k\cdot p\ . \tag{3.14}$$

Importantly, for real k, the matrix $k_{\dot\alpha\beta}$ is hermitian and so may be represented in terms of its eigenvectors and eigenvalues

$$k_{\dot\alpha\beta} = \sum_{i=1,2} \lambda_i n_{i,\dot\alpha}n_{i,\beta} \tag{3.15}$$

with eigenvalues $\lambda_{1,2} = k^0 \pm |\boldsymbol{k}|$ and eigenvectors:

$$n_{1,\alpha} = \begin{pmatrix} e^{-i\phi}\cos\frac{\theta}{2} \\ \sin\frac{\theta}{2} \end{pmatrix} \qquad\qquad n_{2,\alpha} = \begin{pmatrix} \sin\frac{\theta}{2} \\ -e^{i\phi}\cos\frac{\theta}{2} \end{pmatrix} . \tag{3.16}$$

Here θ and ϕ are the polar and azimuthal angles of k and the eigenvectors are normalised such that

$$\langle n_i n_j \rangle = \epsilon_{ji} \ . \tag{3.17}$$

For massless k, equation (3.12) reduces to

$$k_{\dot{\alpha}\beta} = k_{\dot{\alpha}} k_{\beta} \ , \tag{3.18}$$

where $k_\beta = \sqrt{\lambda_1} n_{1,\beta}$. Thus for massless momenta, k and p, equation (3.14) becomes

$$| \langle kp \rangle |^2 = 2k \cdot p \ . \tag{3.19}$$

So we see that (for massless momenta) the spinor product corresponds to the (complex) square-root of a four-vector product.

3.1.3 Spin-$\frac{1}{2}$ particles

External, massive or massless, spin-$\frac{1}{2}$ particles may also be incorporated by constructing appropriate wave-functions, Ψ, from two-spinor components:

$$\Psi = \begin{pmatrix} \phi_\alpha \\ \psi^{\dot{\alpha}} \end{pmatrix} \ . \tag{3.20}$$

The form we shall use is [29]

$$\Psi^{(\pm)}_{k,1} = \begin{pmatrix} \sqrt{\lambda_1} n_{1,\alpha} \\ \mp \sqrt{\lambda_2} n_2^{\dot{\alpha}} \end{pmatrix} \qquad \Psi^{(\pm)}_{k,2} = \begin{pmatrix} \pm \sqrt{\lambda_2} n_{2,\alpha} \\ \sqrt{\lambda_1} n_1^{\dot{\alpha}} \end{pmatrix} \ . \tag{3.21}$$

The $\pm$ denote fermion and antifermion wave-functions respectively, i.e.

$$\not{k} \Psi^{(\pm)}_{k,i} = \pm m \Psi^{(\pm)}_{k,i} \tag{3.22}$$

The index i labels the two helicity states, with $\Psi^{(+)}_{k,1} (\Psi^{(-)}_{k,2})$ corresponding to a positive helicity fermion (antifermion) and $\Psi^{(+)}_{k,2} (\Psi^{(-)}_{k,1})$ corresponding to a negative

helicity fermion (antifermion). Alternatively, in terms of the helicity projector, $\Sigma_k^{\pm}$, we have

$$\Sigma_k^{\pm}\Psi_{k,1}^{(\pm)} = \Psi_{k,1}^{(\pm)} \qquad \Sigma_k^{\pm}\Psi_{k,1}^{(\mp)} = 0 \tag{3.23}$$

$$\Sigma_k^{\pm}\Psi_{k,2}^{(\mp)} = \Psi_{k,2}^{(\mp)} \qquad \Sigma_k^{\pm}\Psi_{k,2}^{(\pm)} = 0 \tag{3.24}$$

where

$$\Sigma_k^{\pm} = \frac{1}{2}\left(1 \pm \gamma^5 \not{s}_k\right) \qquad s_k^{\mu} = \frac{k^0}{m}\frac{k^{\mu}}{|\boldsymbol{k}|} - g^{\mu 0}\frac{m}{|\boldsymbol{k}|}\,. \tag{3.25}$$

The matrix $k_{\dot{\alpha}\beta}$ may also be represented in terms of the components of $\Psi_{k,i}^{(\pm)}$ as

$$k_{\dot{\alpha}\beta} = \phi_{\dot{\alpha}}\phi_{\beta} + \psi_{\dot{\alpha}}\psi_{\beta}\,. \tag{3.26}$$

Finally, for massless k, the spinor wave-functions become

$$\Psi_{k,1}^{(\pm)} = \begin{pmatrix} k_{\alpha} \\ 0 \end{pmatrix} \qquad \Psi_{k,2}^{(\pm)} = \begin{pmatrix} 0 \\ k^{\dot{\alpha}} \end{pmatrix}\,. \tag{3.27}$$

3.1.4 Spin-1 massless gauge bosons

The polarisation vectors of massless gauge bosons[1] may also be represented in terms of two-spinors. The polarisation vectors, $\varepsilon_{i,\mu}(k)$, satisfy

$$k^{\mu}\varepsilon_{i,\mu}(k) = 0 \qquad \varepsilon_i^{\mu}(k)\varepsilon_{i,\mu}(k) = 0 \qquad \varepsilon_i^{\mu}(k)\varepsilon_{j,\mu}^{*}(k) = -\delta_{ij} \qquad i,j = \pm \tag{3.28}$$

which when converted into the matrix notation gives

$$k^{\beta\dot{\alpha}}\varepsilon_{i,\dot{\alpha}\beta}(k) = 0 \quad \varepsilon_{i,\dot{\alpha}\beta}(k)\varepsilon_i^{\dot{\alpha}\beta}(k) = 0 \qquad \varepsilon_{i,\dot{\alpha}\beta}(k)\varepsilon_j^{\beta\dot{\alpha}}(k) = -2\delta_{ij} \qquad i,j = \pm\,. \tag{3.29}$$

An appropriate representation is thus given by

$$\varepsilon_{+,\dot{\alpha}\beta} = \frac{\sqrt{2}g_{\dot{\alpha}}^{+}k_{\beta}}{\langle kg^{+}\rangle^{*}} \qquad \varepsilon_{+,\alpha\dot{\beta}} = \frac{\sqrt{2}k_{\alpha}g_{\dot{\beta}}^{+}}{\langle kg^{+}\rangle^{*}}$$

$$\varepsilon_{-,\dot{\alpha}\beta} = \frac{\sqrt{2}k_{\dot{\alpha}}g_{\beta}^{-}}{\langle kg^{-}\rangle} \qquad \varepsilon_{-,\alpha\dot{\beta}} = \frac{\sqrt{2}g_{\alpha}^{-}k_{\dot{\beta}}}{\langle kg^{-}\rangle}\,. \tag{3.30}$$

[1]Massive gauge bosons may also be treated [29], though we shall not consider them here.

The gauge spinors, $g_\alpha^\pm$, must be linearly independent of k, but are otherwise arbitrary. A change in $g_\alpha^\pm$ corresponds to a gauge transformation (see for example [31]). One of the powerful aspects of the WvdW technique is that a judicious choice of $g_\alpha^\pm$ can often drastically simplify the calculation of the amplitude.

3.2 Computing one-loop corrections

3.2.1 Tensor reduction

We now turn to a discussion of one-loop calculations. This section will be based on [32].

The basic building blocks for the calculation of one-loop corrections are the so-called tensor integrals, $I^{\mu_1\cdots\mu_m}(d;\{q_1,\nu_1\},\ldots,\{q_N,\nu_N\})$, which are defined by[2]

$$I^{\mu_1\cdots\mu_m}(d;\{q_1,\nu_1\},\ldots,\{q_N,\nu_N\}) = \int \frac{d^dk}{i\pi^{d/2}} \frac{k^{\mu_1}\cdots k^{\mu_m}}{d_1^{\nu_1}\cdots d_N^{\nu_N}} \tag{3.31}$$

where

$$d_i = (k+q_i)^2 + i\varepsilon\ . \tag{3.32}$$

These integrals are associated with a one-loop diagram of the form shown in figure 3.1. In [33], it was shown that these tensor integrals may be written in terms of a tensor constructed from the external momenta and scalar integrals in $d \geq 4-2\epsilon$ dimensions, $I(d;\{\nu_k\}_{k=1}^N)$, as follows:

$$\begin{aligned} I^{\mu_1\cdots\mu_m}(d;\{q_1,\nu_1\},\ldots,\{q_N,\nu_N\}) = \sum_{\substack{2\lambda+\sum\kappa_i=m \\ \lambda,\kappa_i\geq 0}} \left(-\frac{1}{2}\right)^\lambda \left\{[g]^\lambda[q_1]^{\kappa_1}\cdots[q_N]^{\kappa_N}\right\}^{\mu_1\cdots\mu_m} \\ \times (\nu_1)_{\kappa_1}\cdots(\nu_N)_{\kappa_N} I(d+2(m-\lambda);\{\nu_k+\kappa_k\}_{k=1}^N) \end{aligned} \tag{3.33}$$

[2]Massive propagators may also be treated, however we shall only consider the massless case here.

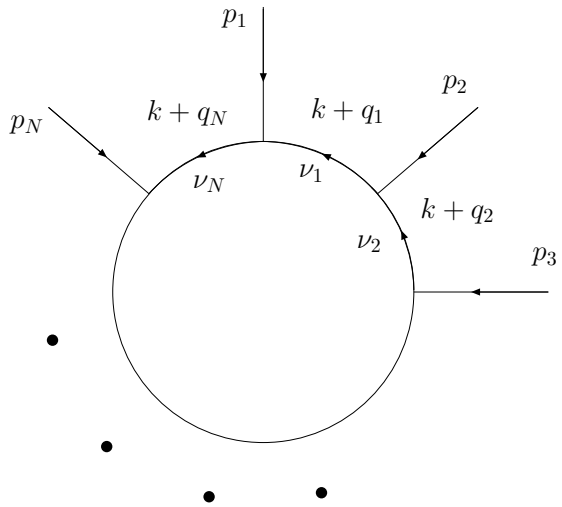

Figure 3.1: Definition of kinematics for a generic one-loop diagram.

where,

$$I(d; \{\nu_k\}_{k=1}^{N}) = \int \frac{d^d k}{i\pi^{d/2}} \frac{1}{d_1^{\nu_1} \cdots d_N^{\nu_N}} \tag{3.34}$$

and $(\nu_i)_{\kappa_i}$ denotes the Pochhammer symbol:

$$(\nu_i)_{\kappa_i} = \frac{\Gamma(\nu_i + \kappa_i)}{\Gamma(\nu_i)} \ . \tag{3.35}$$

The tensor, $\left\{[g]^{\lambda}[q_1]^{\kappa_1} \cdots [q_N]^{\kappa_N}\right\}^{\mu_1 \cdots \mu_m}$ is the totally-symmetric tensor built from λ factors of the metric and κ_i factors of q_i. Thus we see that this relation leaves us with a sum over scalar integrals with dimension ranging between $d + m$ and $d + 2m$ and with up to m additional powers of the original propagators. The reason this decomposition is useful is that scalar integrals in different dimensions and with different powers of propagators may be related to one another through recursion relations, which we discuss in the next section. This allows us to reduce them to a basis set of known integrals.

It was shown in [32] that we may always reduce the integrals appearing on the right in equation (3.33) to the following basis set

- The self-energy integrals $I(d; \{\nu_1, \nu_2\})$.

- The triangle integrals with one off-shell leg, $I(d;\{\nu_1,\nu_2,\nu_3\})$.
- The triangle integrals with two or three off-shell legs, $I(d=4-2\epsilon;\{1,1,1\})$.
- The box integrals $I(d=4-2\epsilon;\{1,1,1,1\})$.
- The pentagon integrals $I(d=6-2\epsilon;\{1,1,1,1,1\})$.

Where d and the ν_i are arbitrary unless indicated otherwise. The analytic expressions for these integrals are collected in appendix A.

3.2.2 Integral recursion

The basic equation

The two key properties of dimensionally regulated scalar integrals, that we shall use to derive the necessary recursion relations, are the dimensional shift identity:

$$I(d-2;\{\nu_k\}_{k=1}^N) = -\sum_{i=1}^N \nu_i I(d;\{\nu_k+\delta_{ik}\}_{k=1}^N) \tag{3.36}$$

and the integration-by-parts identity:

$$\int \frac{d^dk}{i\pi^{d/2}} \frac{\partial}{\partial k^\mu} \left(\frac{\sum_{i=1}^N y_i (k^\mu + q_i^\mu)}{d_1^{\nu_1}\cdots d_N^{\nu_N}} \right) = 0 \tag{3.37}$$

where the y_i are arbitrary. These two identities may be combined to give

$$\begin{aligned}\sum_{i,j=1}^N S_{ji} y_i \nu_j I(d;\{\nu_k+\delta_{kj}\}_{k=1}^N) = &-\sum_{i=1}^N y_i I(d-2;\{\nu_k-\delta_{ki}\}_{k=1}^N) \\ &- \left(d-1-\sum_{j=1}^N \nu_j\right)\left(\sum_{i=1}^N y_i\right) I(d;\{\nu_k\}_{k=1}^N)\end{aligned} \tag{3.38}$$

where the kinematic matrix is given by

$$S_{ij} = (q_i - q_j)^2 \ . \tag{3.39}$$

We will now use equation (3.38) to derive all of the recursion relations we shall require.

Recursion for det$(S) \neq 0$

If the kinematic matrix is non-singular, we may take $y_i = S^{-1}_{il}$, with $1 \leq l \leq N$. Substituting this in equation (3.38), we obtain

$$(\nu_l - 1)I(d; \{\nu_k\}_{k=1}^N) = -\sum_{i=1}^N S^{-1}_{li} I(d-2; \{\nu_k - \delta_{ik} - \delta_{lk}\}_{k=1}^N) \\ - b_l(d-\sigma)I(d; \{\nu_k - \delta_{lk}\}_{k=1}^N) \tag{3.40}$$

where we made use of the following definitions

$$\sigma = \sum_{i=1}^N \nu_i \ , \qquad b_i = \sum_{j=1}^N S^{-1}_{ij} \ , \qquad B = \sum_{i=1}^N b_i \ . \tag{3.41}$$

This relation may reduce the dimension of the scalar integral by two, in addition to reducing the power of a single propagator by up to two units, or two propagators by one unit each.

Another useful recursion relation may be obtained by shifting $\{\nu_k\}_{k=1}^N \to \{\nu_k + \delta_{lk}\}_{k=1}^N$ and summing equation (3.40) over l:

$$(d-1-\sigma)BI(d; \{\nu_k\}_{k=1}^N) = I(d-2; \{\nu_k\}_{k=1}^N) - \sum_{i=1}^N b_i I(d-2; \{\nu_k - \delta_{ik}\}_{k=1}^N) \ . \tag{3.42}$$

The action of this equation reduces the dimension by two and may also reduce the power of one propagator by a single unit. This relation may also be recast as

$$I(d; \{\nu_k\}_{k=1}^N) = (d+1-\sigma)BI(d+2; \{\nu_k\}_{k=1}^N) + \sum_{i=1}^N b_i I(d; \{\nu_k - \delta_{ik}\}_{k=1}^N) \ , \tag{3.43}$$

which may be used to rewrite the $d = 4 - 2\epsilon$ pentagon with unit propagators, $I(4-2\epsilon; \{1\}_{k=1}^5)$, as a sum over boxes in $d = 4-2\epsilon$ and the $d = 6-2\epsilon$ pentagon:

$$I(4-2\epsilon; \{1\}_{k=1}^5) = -2\epsilon BI(6-2\epsilon; \{1\}_{k=1}^5) + \sum_{i=1}^5 b_i I(4-2\epsilon; \{1-\delta_{ik}\}_{k=1}^5) \ . \tag{3.44}$$

The $d = 6 - 2\epsilon$ pentagon however is finite and since it appears multiplied by ϵ here, we may neglect it [34, 35].

Finally, we may combine equations (3.40) and (3.42) to give

$$(\nu_l - 1)I(d; \{\nu_k\}_{k=1}^N) = -\frac{b_l}{B} I(d-2; \{\nu_k - \delta_{lk}\}_{k=1}^N) + \sum_{i=1}^N \left(\frac{b_i b_l}{B} - S_{li}^{-1}\right) I(d-2; \{\nu_k - \delta_{ik} - \delta_{lk}\}_{k=1}^N) \quad (3.45)$$

which reduces the dimension by two and the power of a propagator by up to two.

Recursion for two mass triangles

In the case of triangles with two off-shell legs ($p_1^2, p_2^2 \neq 0, p_3^2 = 0$) the kinematic matrix, (3.39), is singular. However, we may still derive useful recursion relations with different choices for the y_i. For $p_1^2 \neq p_2^2$, the choices

$$y = \begin{pmatrix} 0 \\ \frac{\alpha}{p_2^2} \\ \frac{1-\alpha}{p_1^2} \end{pmatrix}, \qquad \alpha = \frac{p_2^2}{p_2 - p_1^2} \quad (3.46)$$

and

$$y = \begin{pmatrix} 0 \\ \beta p_1^2 \\ -\beta p_2^2 \end{pmatrix} \qquad \forall \beta \quad (3.47)$$

give us the following two equations

$$I(d; \{\nu_k\}_{k=1}^3) = \frac{1}{p_1^2 - p_2^2} \frac{1}{\nu_1 - 1} \left(I(d-2; \{\nu_1 - 1, \nu_2 - 1, \nu_3)\}\right) - I(d-2; \{\nu_1 - 1, \nu_2, \nu_3 - 1\})) \qquad \nu_1 \neq 0 \quad (3.48)$$

and

$$I(d; \{\nu_k\}_{k=1}^3) = \frac{1}{d - 1 - \sigma} \frac{1}{p_2^2 - p_1^2} \left(p_1^2 I(d-2; \{\nu_1, \nu_2 - 1, \nu_3\}) - I(d-2; \{\nu_1, \nu_2, \nu_3 - 1\})\right) \quad (3.49)$$

For the equal mass case, the choice

$$y = \begin{pmatrix} 0 \\ \alpha \\ -\alpha \end{pmatrix} \qquad \forall\alpha \tag{3.50}$$

yields

$$I(d;\{\nu_k\}_{k=1}^3) = I(d;\{\nu_1,\nu_2+1,\nu_3-1\}) \tag{3.51}$$

The algorithm

The above recursion relations will reduce any scalar integral to our basis set by application of the following algorithm [32]:

1. If $N = 3$, $\det(S) = 0$ and $p_1^2 \neq p_2^2$ apply equation (3.49).
2. If $N = 3$, $\det(S) = 0$ and $p_1^2 = p_2^2$ apply equation (3.51).
3. If $\sigma = N = 5$ and $d = 4 - 2\epsilon$ apply equation (3.43).
4. If $\frac{d}{2}|_{\epsilon=0} + N - \sigma = 2$ apply equation (3.40).
5. If $\frac{d}{2}|_{\epsilon=0} + N - \sigma = 3$ and $\sigma > N$ apply equation (3.45).
6. If $\frac{d}{2}|_{\epsilon=0} + N - \sigma = 3$ and $\sigma = N$ apply equation (3.42).
7. If $\frac{d}{2}|_{\epsilon=0} + N - \sigma \geq 4$ apply equation (3.42).
8. Repeat until all integrals are reduced to the basis set.

Chapter 4

Central Exclusive Production

4.1 The process

Central exclusive production (CEP) is the process:

$$h_1(p_1) + h_2(p_2) \to h_1(p_1') \oplus X \oplus h_2(p_2') \tag{4.1}$$

where the hadrons, h_i, remain intact after scattering though a small angle. The $\oplus$ denote rapidity gaps, devoid of particles, between the hadrons and the system X, which decays in the central detector.

The outgoing hadron momenta may be parametrised in terms of the momentum fractions each transfers to X, x_i, and their transverse momenta, $p_{i\perp}'$:

$$p_1'^{\mu} = (1 - x_1)p_1^{\mu} + \frac{\boldsymbol{p}_{1\perp}'^2}{(1 - x_1)s}p_2^{\mu} + p_{1\perp}'^{\mu} \tag{4.2}$$

$$p_2'^{\mu} = (1 - x_2)p_2^{\mu} + \frac{\boldsymbol{p}_{2\perp}'^2}{(1 - x_2)s}p_1^{\mu} + p_{2\perp}'^{\mu} \tag{4.3}$$

with s denoting the centre-of-mass energy squared. The CEP kinematics are defined as

$$\frac{\boldsymbol{p}_{i\perp}'^2}{x_i s} \ll x_i \ll 1 \, . \tag{4.4}$$

If the outgoing hadron momenta are measured, by adding detectors far down the beam-pipe, it is possible to reconstruct the central system's four-momentum. In the CEP kinematic regime, (4.4), the central system's rapidity, y and invariant mass squared, $\hat{s}$, are given approximately by

$$\hat{s} \approx x_1 x_2 s \ , \tag{4.5}$$

$$y \approx \frac{1}{2} \ln \left(\frac{x_1}{x_2} \right) \ . \tag{4.6}$$

In addition, the process possesses a P-even, C-even, $J_z = 0$ selection rule [36] (the origin of which we shall discuss subsequently), where J_z is the projection of the central system's total spin along the hadron collision axis. Thus CEP offers a method to measure both the mass of X [37] (with a resolution of ~ 2 GeV per event [38]) and its spin-parity properties [39]. Photon pairs [40], di-jets [41] and χ_c particles [42] produced via the CEP mechanism have now been observed at the Tevatron and there are groups within both the ATLAS and CMS collaborations actively seeking to observe these events at the LHC [38].

We shall begin by presenting the calculation of this process by the Durham group [36,43–45] and then describe in detail the various aspects of the calculation for the case of Higgs production with incoming protons, which we have independently calculated. We will show that the form of the Durham group's result must be modified and we discuss the phenomenological impact of this alteration.

4.2 The Durham model

The calculation of the process by the Durham group is represented schematically in figure 4.1. The protons exchange a two gluon system, which must be in a colour singlet state in order that the protons remain intact. Two of the gluons then fuse to produce the central system, X. The cross-section is assumed to factorise in

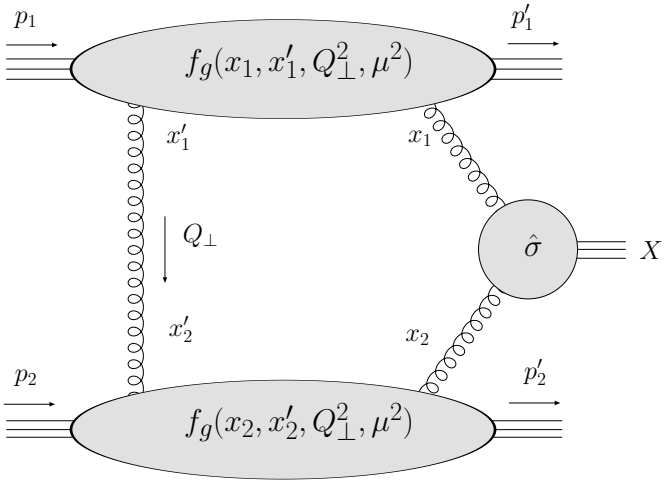

Figure 4.1: Schematic form of the CEP amplitude.

the following way [46]

$$\frac{\partial\sigma}{\partial\hat{s}\partial y\partial\boldsymbol{p}_{1\perp}'^2\partial\boldsymbol{p}_{2\perp}'^2} = S^2 e^{-b(\boldsymbol{p}_{1\perp}'^2+\boldsymbol{p}_{2\perp}'^2)}\frac{\partial\mathcal{L}}{\partial\hat{s}\partial y}d\hat{\sigma}(gg\to X)\,. \tag{4.7}$$

The transverse momenta of the final-state protons, $\boldsymbol{p}_{i\perp}'$, are assumed to be distributed according to a Gaussian, with the slope parameter, $b = 4$ GeV^{-2} [46]. The factor S^2, known as the soft survival factor, accounts for the suppression of the cross-section due to the requirement that soft interactions between the incoming protons do not spoil the exclusivity of the process [47–49]. In general S^2 depends on the kinematics of the process [50–55], however, it is common practice to set it to a constant value, corresponding to the average over the forward detector acceptance of the final-state proton transverse momenta [38]. The partonic cross-section, $\hat{\sigma}$, is related to the matrix element for two on-shell gluons to produce the central system as

$$d\hat{\sigma}(gg\to X) = \frac{1}{2\hat{s}}\left|\bar{\mathcal{M}}(gg\to X)\right|^2 d\mathrm{PS}_X \tag{4.8}$$

where $d\mathrm{PS}_X$ is the phase-space of the final state, X and

$$\bar{\mathcal{M}}(gg\to X) = \frac{1}{2}\frac{1}{N^2-1}\sum_{a_1a_2}\sum_{\lambda_1\lambda_2}\delta_{a_1a_2}\delta_{\lambda_1\lambda_2}\mathcal{M}_{\lambda_1\lambda_2}^{a_1a_2}(gg\to X) \tag{4.9}$$

with $\mathcal{M}^{a_1 a_2}_{\lambda_1 \lambda_2}$ the amplitude for two on-shell gluons, with colours a_i and helicities λ_i, to fuse to produce X. Note that the averages are carried out at the amplitude level, in contrast to an inclusive partonic cross-section. We shall discuss why this is the case in section 4.4.1. In addition, the fact that the gluons have equal helicities ($\lambda_1 = \lambda_2$) is the origin of the $J_z = 0$ selection rule.

Lastly, the effective luminosity is given by

$$\frac{\partial \mathcal{L}}{\partial \hat{s} \partial y} = \frac{1}{\hat{s}} \left(\frac{\pi}{N^2 - 1} \int \frac{d\boldsymbol{Q}_\perp^2}{\boldsymbol{Q}_\perp^4} f_g(x_1, x_1', \boldsymbol{Q}_\perp^2, \mu^2) f_g(x_2, x_2', \boldsymbol{Q}_\perp^2, \mu^2) \right)^2 . \tag{4.10}$$

The f_g are skewed, unintegrated, gluon distribution functions. Due to the kinematics of the process the amplitude is dominated by the region $x_i' \ll x_i$ and in this regime these distributions may be related to the conventional, integrated, gluon density [43, 56]:

$$f_g(x, x', \boldsymbol{Q}_\perp^2, \mu^2) \approx R_g \frac{\partial}{\partial \ln \boldsymbol{Q}_\perp^2} \left(\sqrt{T(\boldsymbol{Q}_\perp, \mu)} x g(x, \boldsymbol{Q}_\perp^2) \right) . \tag{4.11}$$

The factor R_g is given by

$$R^g = \frac{H_g(\frac{x}{2}, \frac{x}{2}; \boldsymbol{Q}_\perp^2)}{x g(x; \boldsymbol{Q}_\perp^2)} \tag{4.12}$$

and accounts for the skewed effect (H_g is the skewed gluon distribution defined in section 2.5.1). R_g is approximately equal to 1.2(1.4) at the LHC(Tevatron)[1] [46, 57]. The f_g distributions also include a Sudakov factor [56, 58]:

$$T(\boldsymbol{Q}_\perp, \mu) = \exp \left(- \int_{\boldsymbol{Q}_\perp^2}^{\mu^2} \frac{dk_\perp^2}{k_\perp^2} \frac{\alpha_s(k_\perp^2)}{2\pi} \int_0^{1-\Delta} dz \left[z P_{gg}(z) + \sum_q P_{qg}(z) \right] \right) \tag{4.13}$$

where

$$\Delta = \frac{k_\perp}{k_\perp + \mu} , \tag{4.14}$$

$$\mu = 0.62 \sqrt{\hat{s}} . \tag{4.15}$$

[1] For an LHC running at 14 TeV.

The Sudakov factor resums logarithmically enhanced soft and collinear virtual corrections and accounts for the fact that real radiation from the process is forbidden.

The Durham group's claim is that this expression resums logarithms in $\hat{s}/\boldsymbol{Q}_\perp^2$, to next-to-leading logarithmic accuracy. That is, it takes into account all terms of order $\alpha_s^n \ln^m(\hat{s}/\boldsymbol{Q}_\perp^2)$, with $m = 2n, 2n-1$. This requires a precise specification of both the lower limit on the $k_\perp$ integral in equation (4.13) and the cutoff on the z integral as $z \to 1$. Note that the upper cutoff on the $k_\perp$ integral corresponds to non-collinear hard radiation and as such there is no logarithm associated with this region. Thus, to next-to-leading logarithmic accuracy, only its order of magnitude is required.

The lower cutoff on the $k_\perp^2$ integral must be of the order of $\boldsymbol{Q}_\perp^2$, since radiation of a much lower transverse momentum would not be able to resolve the exchanged colour singlet system, the size of which is of order $1/|\boldsymbol{Q}_\perp|$. To extract the precise value, the Durham group use the fact that this region, with $k_\perp \sim |\boldsymbol{Q}_\perp|$ and the momentum fraction integral producing a logarithm, may be described within the BFKL framework [24–27] (see for example [28]). The BFKL summation of the momentum fraction logarithms implies the following replacement [59]

$$\int \frac{d^2k_\perp}{k_\perp^2} \to \int \frac{d^2k_\perp}{k_\perp^2}\left(1 - \frac{\boldsymbol{Q}_\perp^2}{k_\perp^2 + (\boldsymbol{Q}_\perp - \boldsymbol{k}_\perp)^2}\right) \approx \int_{\boldsymbol{Q}_\perp^2} \frac{d^2k_\perp}{k_\perp^2} \tag{4.16}$$

Thus determining the lower limit. We shall discuss this point in more detail in section 4.4.1.

Having specified the lower limit in this way, the Durham group fix the cutoff on the z integral, which they claim is due to wide angle soft gluon radiation [45], by considering the cross-section for central exclusive Higgs production. Their approach is to calculate the cross-section for two on-shell gluons to fuse to produce a Higgs and one additional gluon, which they then argue, thanks to unitarity, may be used to imply the form of the virtual corrections making up the CEP

Sudakov factor. To be more specific, they consider the region $\boldsymbol{Q}_\perp^2 \ll k_\perp^2 \ll m_H^2$, leaving the $k_\perp$ integral of the radiated gluon unevaluated but integrating numerically over its polar angle. The result is then fit to a function of the form $a + b\ln(m_H/(2k_\perp))$, where a and b are $k_\perp$-independent constants [60]. This approach gives the following result for the cross-section [45]

$$\sigma(gg \to Hg) \propto \int \frac{dk_\perp^2}{k_\perp^2} \frac{C_A \alpha_s}{\pi} \left(0.212 + \ln\left(\frac{m_H}{2k_\perp}\right) - \frac{11}{12} \right) . \tag{4.17}$$

The factor of 11/12 here is the usual component of the β-function coming from the $z \to 1$ finite pieces of the $P_{gg}(z)$ splitting kernel. The Durham group then assume that the factor of 0.212 here is due to the region of wide angle soft gluon emission. If this is the case, it may be absorbed into the logarithmic term (which is also due to soft emission). Equivalently, this may be written in terms of a momentum fraction integral

$$\sigma(gg \to Hg) \propto \int \frac{dk_\perp^2}{k_\perp^2} \frac{\alpha_s}{2\pi} \int_0^{1-\Delta} z P_{gg}(z)\, dz \tag{4.18}$$

where Δ is given by equations (4.14) and (4.15). Unitarity then guarantees that the soft cut-off in the real and virtual corrections must be identical, allowing one to infer the form of the z-integral cut-off in the Sudakov factor, (4.13).

Our finding is that this approach is not correct. Specifically, rather than equations (4.14) and (4.15) we find instead $\Delta = k_\perp/m_H$. In the next sections we will describe our evidence for this assertion, in the form of an all orders approximation to the CEP amplitude, an explicit next-to-leading order calculation of the relevant virtual corrections and a recalculation in the Durham group's approach, which however gives a different result to theirs.

4.3 Lowest order Higgs production

We begin our investigation of the Durham model by computing (in Feynman gauge) the lowest order amplitude for two quarks of different flavour to scatter

into two quarks and a Higgs, $A_{\rm LO}$. We take the quarks as scattering in the forward direction:

$$p_1'^{\mu} = (1 - x_1)p_1^{\mu} \,, \tag{4.19}$$

$$p_2'^{\mu} = (1 - x_2)p_2^{\mu} \,. \tag{4.20}$$

The dependence of the amplitude on the outgoing hadron transverse momenta in equation (4.7) is a non-perturbative effect and so we do not expect to be sensitive to it here. We will also make frequent use of the high energy limit: keeping only terms not suppressed by an inverse power of the centre-of-mass energy. In this limit, there are four lowest order diagrams which contribute, as shown in figure 4.2. In addition, we work in the effective theory in which the top quark has been integrated out [61–63]. This generates a point-like coupling of the Higgs to gluons (see appendix B).

For small x_i the amplitude is dominated by the region in which the exchanged gluons are soft and we may therefore take the gluons as coupling to the quark lines via eikonal vertices. Thus, for example, the contribution to the amplitude of graph 4.2(a), with the colour singlet contribution projected out, takes the form

$$A^{4.2(a)} = -i\delta_{\sigma_1\sigma_1'}\delta_{\sigma_2\sigma_2'}16T_F^2\frac{N_C^2-1}{N_C^2}g^4 p_1\cdot p_2\int\frac{d^4Q}{(2\pi)^4}\frac{p_1^{\mu}p_2^{\nu}H_{\mu\nu}(k_1,k_2;\mu)}{\mathcal{D}} \tag{4.21}$$

where

$$\begin{aligned}\mathcal{D} = {} & [Q^2+i\varepsilon][(Q-p_1)^2+i\varepsilon][(Q+p_2)^2+i\varepsilon] \\ & \times[(Q-x_1p_1)^2+i\varepsilon][(Q+x_2p_2)^2+i\varepsilon]\end{aligned} \tag{4.22}$$

and the Higgs vertex factor, $H^{\mu\nu}$, has the form (see appendix B)

$$H^{\mu\nu}(k_1,k_2;\mu) = -iC_1^R(\mu)(k_1\cdot k_2 g^{\mu\nu} - k_2^{\mu}k_1^{\nu}) \,. \tag{4.23}$$

Working in the centre-of-mass frame of p_1 and p_2, with p_1 defining the z-axis, we may evaluate the Q^+ and Q^- integrals for each graph. To leading power in

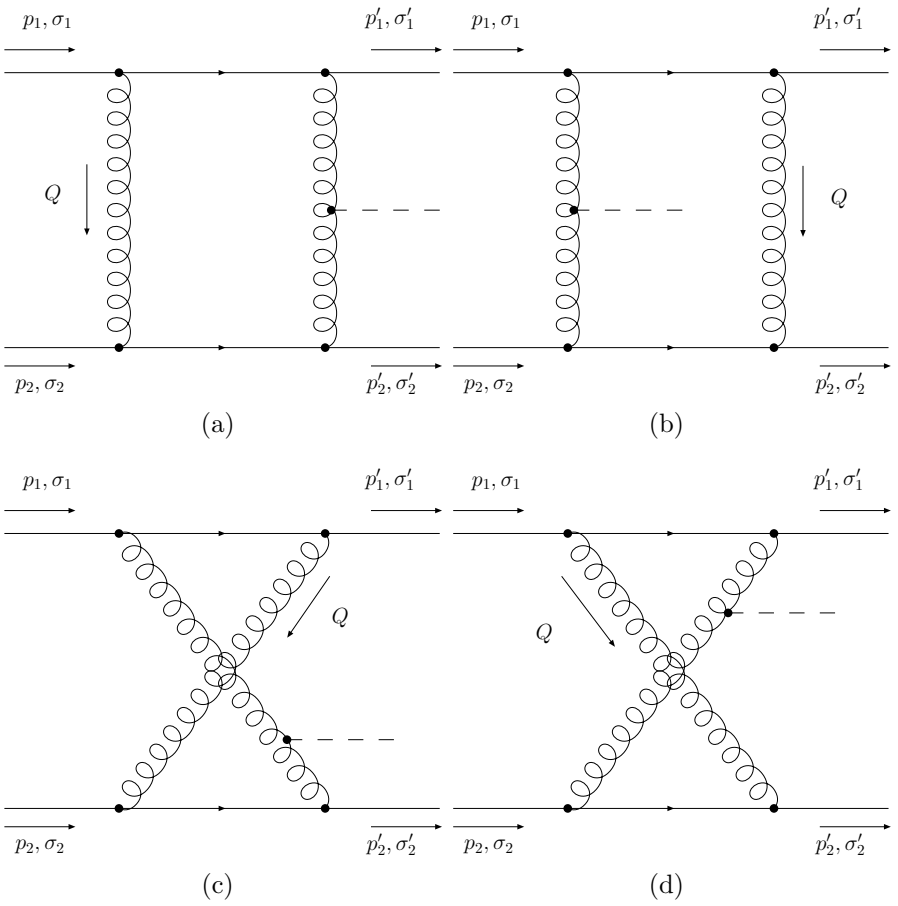

Figure 4.2: The lowest order diagrams contributing to $q + q' \to q \oplus H \oplus q'$, in the high energy limit.

the high-energy limit we obtain

$$A^{4.2(a)} = A^{4.2(c)} = A^{4.2(d)} = 0$$
$$A_{\rm LO} = A^{4.2(b)} = A_0(\mu) \int_\Lambda \frac{d\boldsymbol{Q}_\perp^2}{\boldsymbol{Q}_\perp^4} \tag{4.24}$$

where Λ is a cutoff imposed to define the integral and

$$A_0(\mu) = -\delta_{\sigma_1\sigma_1'}\delta_{\sigma_2\sigma_2'} C_1^R(\mu) g^4 \frac{s}{\pi} \frac{T_F^2 C_F}{N_C} \ . \tag{4.25}$$

A couple of comments are in order at this point. The first is that the amplitude is infrared power-divergent as $\Lambda \to 0$, this is to be expected however, since we are dealing with a fixed order expansion and (within perturbation theory - see

the footnote at the beginning of section 4.4.1) only the all-orders Sudakov factor removes the divergence. We shall discuss the origin of the Sudakov factor in the next section. The second comment is that the contribution to the S-matrix (iA) is pure imaginary. This is expected for colour singlet exchange in the high energy limit, based on arguments from Regge theory [28]. Thirdly, note that it is perhaps not surprising that diagram 4.2(b) gives a different result from all of the other diagrams, since it is the only one in which Q is pinched in the Glauber/Coulomb region.

Since its imaginary part dominates, we could equally well have used the Cutkosky rules [64] to evaluate the amplitude. In fact, it is this approach we shall use to evaluate the next-to-leading order corrections in section 4.5. The structure of the lowest order calculation will give us some hint as to how we may simplify the next-to-leading order corrections and so we detail it here.

Recall that the Cutkosky rules implement the unitarity relation, equation (2.25). For a cut to be allowed it must satisfy two conditions: the invariant-mass of the four-momenta on each side of the cut and the total energy flowing from left to right across the cut must both be positive. Given these conditions, the possible cuts of the general CEP amplitude are shown in figure 4.3 and the possible cuts of the lowest order diagrams are shown in figure 4.4.

It turns out however, that we need only consider the cuts 4.4(a) and 4.4(e); the remaining cuts all cancel amongst one another. The reason for this is that these diagrams represent a sum over soft gluon insertions onto the upper or lower quark lines. The fact that the soft gluon in all these cases is cut ensures that it is not in the Coulomb/Glauber region and we may thus apply the soft approximation as described in section 2.6.1. The result is that we may rewrite each sum of diagrams as a single diagram with the soft gluon connected to an eikonal line. This is shown explicitly in figure 4.5 for the diagrams 4.4(b) and 4.4(g). Note

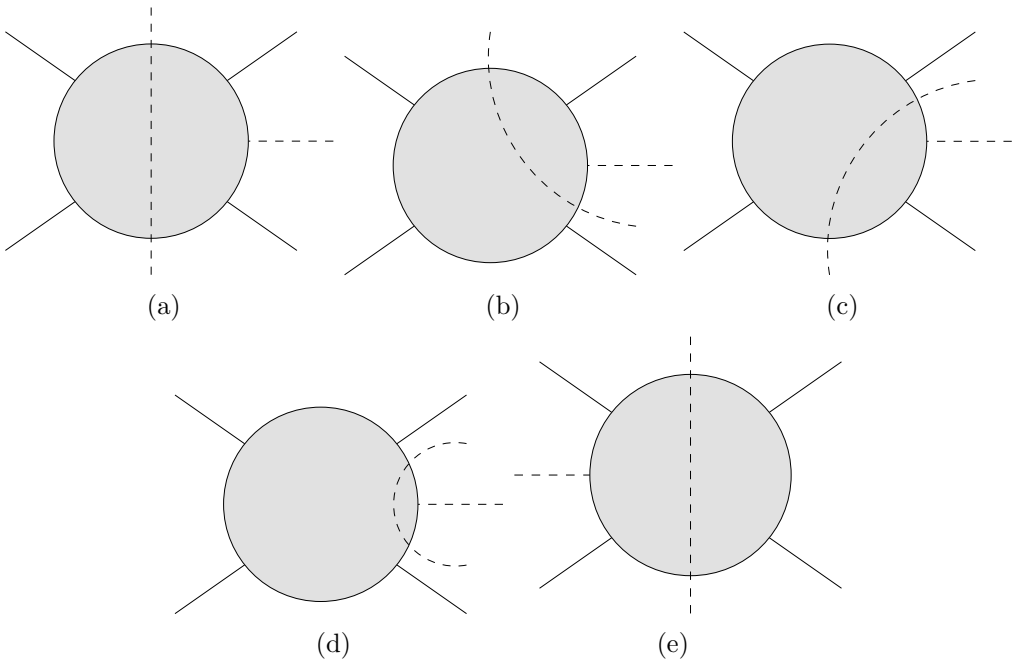

Figure 4.3: The allowed cuts of the CEP amplitude.

that the upper quark line is now connected to the lower part of the diagram by a single gluon. The key point now is that we are dealing with colour singlet exchange, however, such diagrams contribute only to the octet exchange part of the amplitude. We may therefore neglect them.

This situation generalises to all orders. We need not consider the cuts 4.3(b)-4.3(d) since they never make a leading contribution to the colour singlet exchange amplitude.

4.4 All orders Higgs production

4.4.1 Hard collinear emissions

Corrections factorised into the pdfs

As previously mentioned, the inclusion of large logarithms appearing at all-orders in the perturbation series is crucial if we are to obtain the correct CEP amplitude.

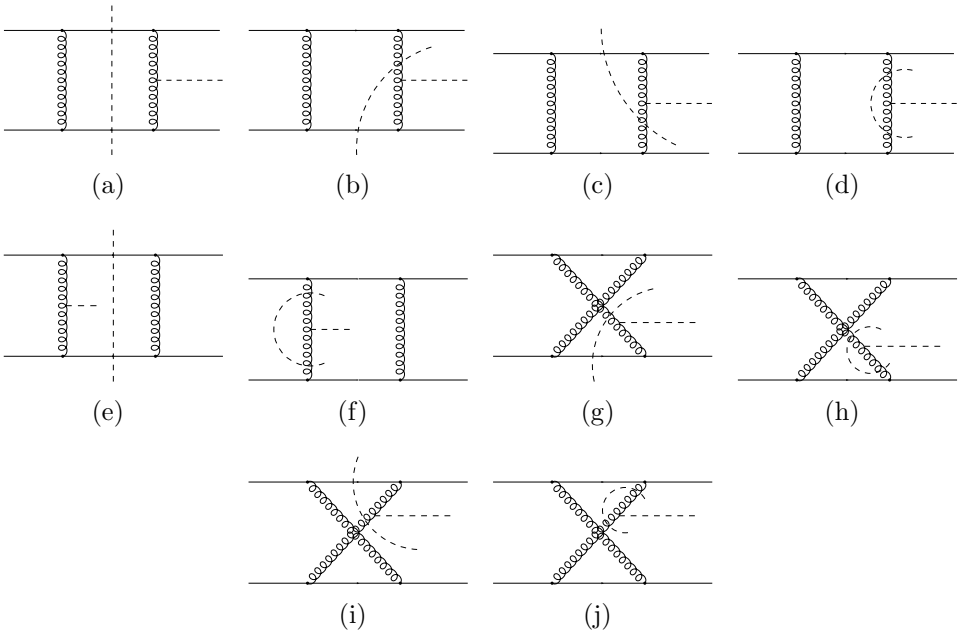

Figure 4.4: The possible cuts of the lowest order diagrams.

Indeed, as we saw at lowest order, the result is divergent without them[2]. From chapter 2 we know that the enhanced terms correspond to emissions which are collinear with external particles and/or soft. In this section we shall discuss the subset of these corrections corresponding to hard collinear emissions.

We begin with the ansatz that the central-exclusive Higgs production amplitude, $\mathcal{A}_{\rm CEP}$, factorises at some scale, μ_F, much lower than all other scales in the problem. The amplitude may then be written, for small x_i, as (see equation (2.78))

$$\mathcal{A}_{\rm CEP} \approx \frac{s}{2}\sum_{a_0,\bar{a}_0}\int d\xi_0 \int d\bar{\xi}_0 H_{a_0}(\xi_0,\eta;\mu_F^2)H_{\bar{a}_0}(\bar{\xi}_0,\bar{\eta};\mu_F^2) \times C^{a_0\bar{a}_0}(\xi_0,\eta,\mu_F^2;\bar{\xi}_0,\bar{\eta},\mu_F^2) \tag{4.26}$$

[2]Actually, the amplitude must be finite even without the inclusion of Sudakov effects, since as $\boldsymbol{Q}_\perp \to 0$ the wavelength of the exchanged gluons becomes too large to resolve the colourless protons. Such an effect however lies beyond perturbation theory, though it has been studied in [65], using a simple non-perturbative model [66, 67].

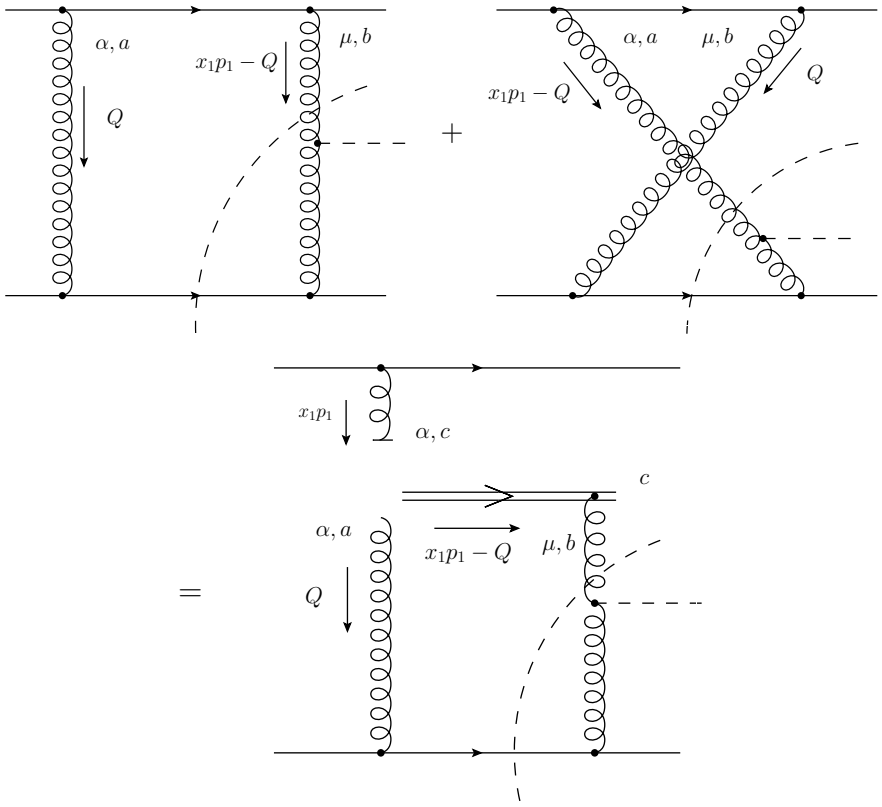

Figure 4.5: Rewriting a sum of cuts in terms of an insertion onto an eikonal line.

where the kinematics are shown in figure 4.6 and we define

$$p^\mu = p_1^\mu + p_1'^\mu \,, \tag{4.27}$$

$$\bar{p}^\mu = p_2^\mu + p_2'^\mu \,. \tag{4.28}$$

The large logarithmic corrections to the coefficient function, $C^{a_0\bar{a}_0}$, may be computed by cutting off the parton transverse momenta at μ_F, which is equivalent to dimensional regularisation in the $\overline{\text{MS}}$ scheme [68]. In addition, $C^{a_0\bar{a}_0}$, is obtained from Feynman diagrams in the same manner as C^q and C^g in equations (2.82) and (2.111) respectively. We may now follow the same method as we employed to derive equations (2.113) and (2.114). In this case however, there is a mismatch between the corrections which have the form of a self-energy, such as the first eikonal line diagram in figure 2.15 and those which involve the exchange of a

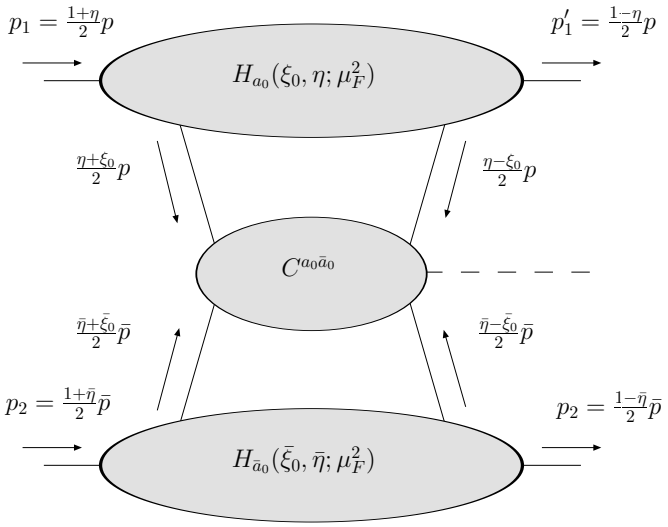

Figure 4.6: Factorisation of the central exclusive Higgs production amplitude.

parton in the s-channel. The mismatch occurs because diagrams, such as the one shown in figure 4.7(b), not involving at least one s-channel parton collinear to each hadron, are suppressed by the centre-of-mass energy. Given this, we iterate the formula for collinear emissions, (2.113), until there is only one s-channel emission left associated with each hadron:

$$\begin{aligned} C^{a_0\bar{a}_0}(\xi_0, \eta, \mu_F^2; \bar{\xi}_0, \bar{\eta}, \mu_F^2) = \sum_{n=0}^{\infty} \Bigg[\Bigg(-\sum_{a_1} \int_{\mu_F^2}^{l_2^2} \frac{dl_1^2}{l_1^2} \frac{\alpha_s(l_1^2)}{4\pi} \int d\xi_1 K_{(0)}^{a_1 a_0} \Bigg) \\ \cdots \Bigg(-\sum_{a_n} \int_{\mu_F^2}^{\boldsymbol{Q}_\perp^2} \frac{dl_n^2}{l_n^2} \frac{\alpha_s(l_n^2)}{4\pi} \int d\xi_n K_{(0)}^{a_n a_{n-1}} \Bigg) \Bigg] \\ \times \sum_{\bar{n}=0}^{\infty} \Bigg[\Bigg(-\sum_{\bar{a}_1} \int_{\mu_F^2}^{\bar{l}_2^2} \frac{d\bar{l}_1^2}{\bar{l}_1^2} \frac{\alpha_s(\bar{l}_1^2)}{4\pi} \int d\bar{\xi}_1 K_{(0)}^{\bar{a}_1 \bar{a}_0} \Bigg) \\ \cdots \Bigg(-\sum_{\bar{a}_{\bar{n}}} \int_{\mu_F^2}^{\bar{\boldsymbol{Q}}_\perp^2} \frac{d\bar{l}_{\bar{n}}^2}{\bar{l}_{\bar{n}}^2} \frac{\alpha_s(\bar{l}_{\bar{n}}^2)}{4\pi} \int d\bar{\xi}_{\bar{n}} K_{(0)}^{\bar{a}_{\bar{n}} \bar{a}_{\bar{n}-1}} \Bigg) \Bigg] \\ \times C_{2 \text{ s-channel}}^{a_n \bar{a}_{\bar{n}}}(\xi_n, \eta; \bar{\xi}_{\bar{n}}, \bar{\eta}) \end{aligned} \tag{4.29}$$

where $\boldsymbol{Q}_\perp$ and $\bar{\boldsymbol{Q}}_\perp$ are the transverse momenta of the final two s-channel emissions, which are contained in $C_{2 \text{ s-channel}}^{a_n \bar{a}_{\bar{n}}}$.

Now, as in section 2.5.4, the collinear logarithms may be absorbed into the

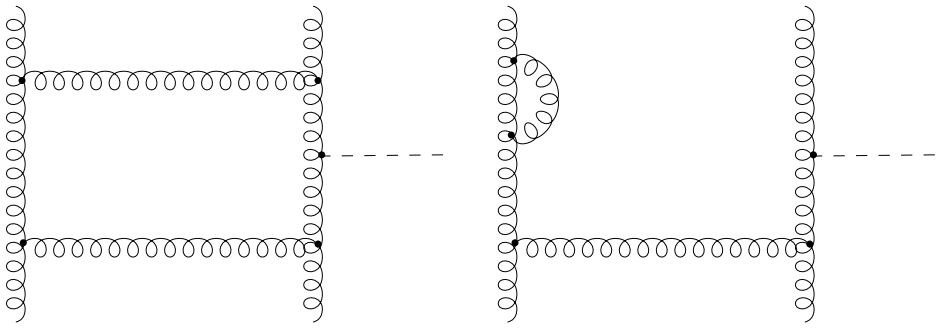

Figure 4.7: Two diagrams contributing to CEP. The left-hand diagram makes a leading contribution, whereas the right-hand diagram is suppressed by the centre-of-mass energy.

pdfs:

$$\mathcal{A}_{\text{CEP}} \approx \frac{s}{2} \sum_{a,\bar{a}} \int d\xi \int d\bar{\xi} H_a(\xi, \eta; \boldsymbol{Q}_\perp^2) H_{\bar{a}}(\bar{\xi}, \bar{\eta}; \bar{\boldsymbol{Q}}_\perp^2) C_{2\text{ s-channel}}^{a\bar{a}}(\xi, \eta; \bar{\xi}, \bar{\eta}) \quad (4.30)$$

where

$$\begin{aligned} H_a(\xi, \eta; \boldsymbol{Q}_\perp^2) = H_a(\xi, \eta; \mu_F^2) + \sum_{a_0} \int d\xi_0 \; H_{a_0}(\xi_0, \eta; \mu_F^2) \\ \times \sum_{n=1}^{\infty} \left(- \prod_{j=1}^{n-1} \sum_{a_j} \int_{\mu_F^2}^{l_{j+1}^2} \frac{dl_j^2}{l_j^2} \frac{\alpha_s(l_j^2)}{4\pi} \int d\xi_j \; K_{(0)}^{a_j a_{j-1}} \right) \\ \times \left(- \int_{\mu_F^2}^{\boldsymbol{Q}_\perp^2} \frac{dl_n^2}{l_n^2} \frac{\alpha_s(l_n^2)}{4\pi} K_{(0)}^{a a_{n-1}} \left(\frac{\eta + \xi}{2}, \frac{\eta - \xi}{2} \middle| \frac{\eta + \xi_{n-1}}{2}, \frac{\eta - \xi_{n-1}}{2} \right) \right) \end{aligned} \quad (4.31)$$

and likewise for $H_{\bar{a}}(\bar{\xi}, \bar{\eta}; \bar{\boldsymbol{Q}}_\perp^2)$.

To study the remaining coefficient function, we take $\{a, \bar{a}\} = \{q, q\}$ as an example. The diagrams contributing to $C_{2\text{ s-channel}}^{qq}$ are shown in figure 4.8. The

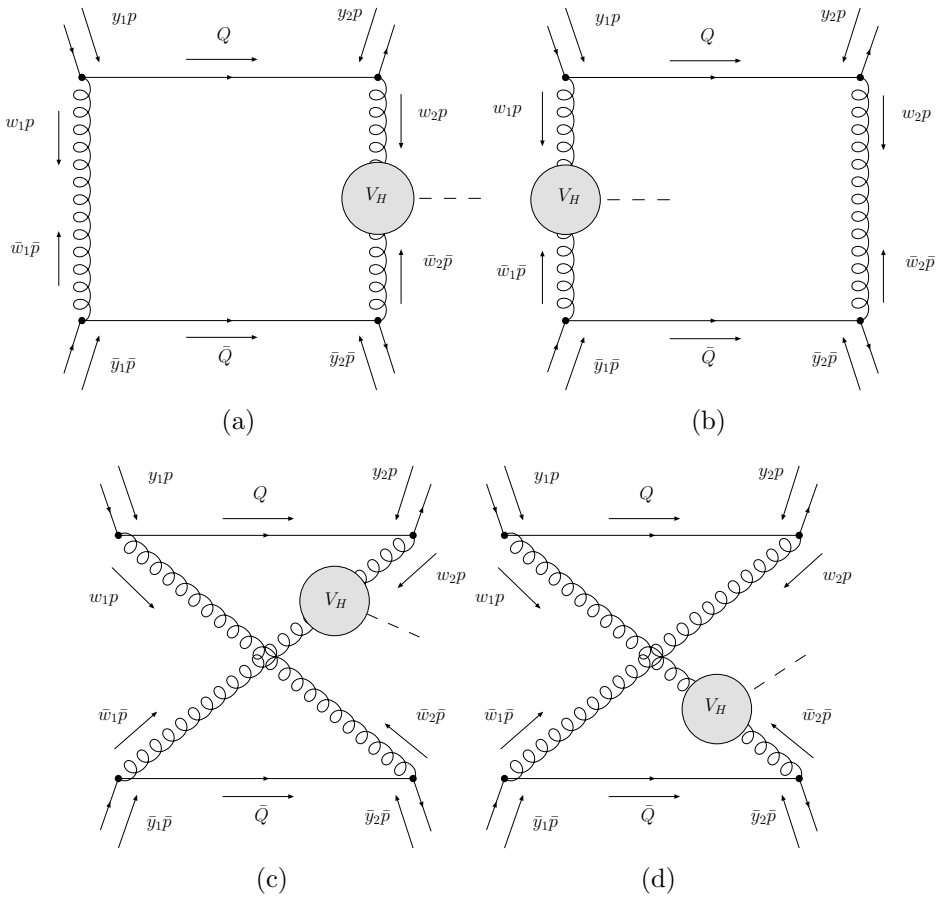

Figure 4.8: Diagrams contributing to $C_{2\text{ s-channel}}^{qq}$.

contribution from figure 4.8(a), for example, may be written:

$$\begin{aligned} C_{2\text{ s-channel}}^{qq}(\xi,\eta;\bar{\xi},\bar{\eta})|_{4.8(\text{a})} = \\ &\times \left(\frac{ig^2T_F}{4N}\sum_a \int \frac{d^4Q}{(2\pi)^4}\frac{\text{Tr}\left[\gamma^-\gamma^\mu \not{Q}\gamma^\alpha\right]}{[Q^2+i\varepsilon][(y_1p-Q)^2+i\varepsilon][(y_2p+Q)^2+i\varepsilon]}\right) \\ &\times \left(\frac{ig^2T_F}{4N}\sum_{\bar{a}} \int \frac{d^4\bar{Q}}{(2\pi)^4}\frac{\text{Tr}\left[\gamma^+\gamma^\nu \bar{\not{Q}}\gamma_\alpha\right]}{[\bar{Q}^2+i\varepsilon][(\bar{y}_1\bar{p}-\bar{Q})^2+i\varepsilon][(\bar{y}_2\bar{p}+\bar{Q})^2+i\varepsilon]}\right) \\ &\times i(y_1p-Q)^2(2\pi)^4\delta^{(4)}(y_1p+\bar{y}_1\bar{p}-Q-\bar{Q})V_{H\mu\nu}^{a\bar{a}}(y_2p+Q,\bar{y}_2\bar{p}+\bar{Q})\ . \end{aligned} \tag{4.32}$$

We may approximate the delta-function as

$$\delta^{(4)}(y_1p+\bar{y}_1\bar{p}-Q-\bar{Q}) \approx \delta(w_1p^+)\delta(\bar{w}_1\bar{p}^-)\delta^{(2)}(Q_\perp+\bar{Q}_\perp) \tag{4.33}$$

which decouples the momentum fraction integrals of the upper and lower sections of the diagram. In addition, we may simplify the trace structure in equation (4.32) as follows. Evaluating one of the traces gives:

$$\begin{aligned}\mathrm{Tr}\left[\gamma^-\gamma^\mu \not{Q}\gamma^\alpha\right] &= \frac{4}{p^+}\left(p^\mu Q^\alpha + p^\alpha Q^\mu - p\cdot Q g^{\mu\alpha}\right) \\ &\approx \frac{4}{p^+}\left(p^\mu Q^\alpha + p^\alpha Q^\mu\right)\end{aligned} \tag{4.34}$$

where we took

$$Q^\mu \approx y_1 p^\mu + Q_\perp^\mu \,, \tag{4.35}$$

which is correct up to terms which do not generate a power divergence and hence $p\cdot Q = 0$. Next, we use the gauge invariance of the Higgs vertex:

$$\left(Q^\mu + y_2 p^\mu\right) V_{H\mu\nu}^{a\bar{a}} = 0 \tag{4.36}$$

to make the replacements

$$\begin{aligned}Q^\mu &\equiv -y_2 p^\mu \\ p^\mu &\equiv -\frac{Q_\perp^\mu}{(y_1+y_2)} \,.\end{aligned} \tag{4.37}$$

Thus we find:

$$\mathrm{Tr}\left[\gamma^-\gamma^\mu \not{Q}\gamma^\alpha\right] \approx \frac{8}{p^+}(y_2 - y_1)\frac{Q_\perp^\mu p^\alpha}{x_1} \tag{4.38}$$

where we dropped a term quadratic in $Q_\perp$ and used:

$$y_1 + y_2 = \frac{x_1}{2-x_1} \approx \frac{x_1}{2} \,. \tag{4.39}$$

The other trace appearing in equation (4.32) may be treated in an entirely analogous manner, with the result

$$\mathrm{Tr}\left[\gamma^+\gamma^\nu \bar{\not{Q}}\gamma_\alpha\right] \approx \frac{8}{\bar{p}^-}(\bar{y}_2 - \bar{y}_1)\frac{\bar{Q}_\perp^\nu \bar{p}_\alpha}{x_2} \,. \tag{4.40}$$

Furthermore, we may write

$$\frac{Q_\perp^\mu \bar{Q}_\perp^\nu}{\boldsymbol{Q}_\perp^2} V_{H\mu\nu}^{a\bar{a}} = \bar{V}_H \delta^{a\bar{a}}$$
$$= \delta^{a\bar{a}} \frac{1}{2} \frac{1}{N^2-1} \sum_{a_1 a_2} \sum_{\epsilon_1 \epsilon_2} \delta^{a_1 a_2} \delta_{\epsilon_1 - \epsilon_2} \epsilon_1^\mu \epsilon_2^\nu V_{H\mu\nu}^{a_1 a_2} \tag{4.41}$$

This is the origin of the requirement that the gluons fusing to produce the Higgs have equal helicities, as in equation (4.9).

Collecting everything together, we have

$$s\, C_{2\,\text{s-channel}}^{qq}(\xi, \eta; \bar{\xi}, \bar{\eta})|_{4.8(\text{a})} \approx \int \frac{d\boldsymbol{Q}_\perp^2}{\boldsymbol{Q}_\perp^4} \left(-\frac{1}{2} K^{gq}\left(0, \frac{x_1}{2}\middle| y_1, y_2\right)\right)$$
$$\times \left(-\frac{1}{2} K^{gq}\left(0, \frac{x_2}{2}\middle| \bar{y}_1, \bar{y}_2\right)\right)$$
$$\times \frac{\pi^3 2^3 (-i)}{x_1 x_2 (N^2-1)} \bar{V}_H \,. \tag{4.42}$$

Including the other diagrams, 4.8(b)-4.8(d) and incoming gluons, we find

$$\mathcal{A}_{\text{CEP}} \approx \int \frac{d\boldsymbol{Q}_\perp^2}{\boldsymbol{Q}_\perp^4} \sum_{a,\bar{a}} \int d\xi \int d\bar{\xi} H_a(\xi, \eta; \boldsymbol{Q}_\perp^2) H_{\bar{a}}(\bar{\xi}, \bar{\eta}; \boldsymbol{Q}_\perp^2)$$
$$\times \left(-\frac{1}{2} \tilde{K}^{ga}\left(0, \frac{x_1}{2}\middle| y_1, y_2\right) - \frac{1}{2} \tilde{K}^{ga}\left(\frac{x_1}{2}, 0\middle| y_1, y_2\right)\right)$$
$$\times \left(-\frac{1}{2} \tilde{K}^{g\bar{a}}\left(0, \frac{x_2}{2}\middle| \bar{y}_1, \bar{y}_2\right) - \frac{1}{2} \tilde{K}^{g\bar{a}}\left(\frac{x_2}{2}, 0\middle| \bar{y}_1, \bar{y}_2\right)\right)$$
$$\times \frac{\pi^3 2^2 (-i)}{x_1 x_2 (N^2-1)} \bar{V}_H \,. \tag{4.43}$$

Here, the $\tilde{K}$ denote the unregularised splitting kernels, that is, the kernels of equations (2.69) but without the plus-prescription. This is due to the requirement that the last two emissions are not of the self-energy type. For now, we shall simply replace them with the regularised kernels; this point requires a proper treatment of soft gluon effects, which we shall cover in the next section. After this replacement, we may use the evolution equation, (2.63) and the symmetry

relation, $H_g(-\xi,\eta;\boldsymbol{Q}_\perp^2) = H_g(\xi,\eta;\boldsymbol{Q}_\perp^2)$ [17], to write

$$\mathcal{A}_{\rm CEP} \approx \int \frac{d\boldsymbol{Q}_\perp^2}{\boldsymbol{Q}_\perp^4} \frac{\partial}{\partial \ln(\boldsymbol{Q}_\perp^2)} \left[H_g\left(\frac{x_1}{2},\frac{x_1}{2};\boldsymbol{Q}_\perp^2\right)\right] \frac{\partial}{\partial \ln(\boldsymbol{Q}_\perp^2)} \left[H_g\left(\frac{x_2}{2},\frac{x_2}{2};\boldsymbol{Q}_\perp^2\right)\right] \times \frac{\pi^3 2^4(-i)}{x_1 x_2 (N^2-1)} \bar{V}_H \ . \tag{4.44}$$

Corrections which generate the Sudakov factor

Although we have now dealt with all emissions which factorise into the pdfs, there are still large logarithms contained in $\bar{V}_H$. Again, we may follow the same logic to extract these emissions, though this time only the self-energy type diagrams contribute. The diagrams relevant for emissions collinear to k_2, after factorisation onto an eikonal line, are shown in figure 4.9, with an equivalent pair of diagrams for emissions collinear to k_1 not shown.

Using the eikonal Feynman rules of figure 2.9, but with $u^\mu = \delta^\mu_-$ replaced by $v^\mu = \delta^\mu_+$, since k_2 moves dominantly in the minus direction, we find for figure 4.9(a)

$$V^{ab}_{H\mu\nu}|_{4.9(\rm a)} = \int \frac{d^4q}{(2\pi)^4} \frac{(-i)}{k_2'^2+i\epsilon} \frac{(-i)}{q^2+i\epsilon} f^{cbd} V_{3\alpha\nu\beta}(-k_2',k_2,-q) \frac{i}{(-q\cdot v)} \times igv^\beta (-if^{dec}) V^{ae}_{H\mu\alpha} \tag{4.45}$$

The three-gluon vertex here becomes

$$V_{3\alpha\nu\beta}(-k_2',k_2,-q) = g(g_{\alpha\nu}(-k_2'-k_2)_\beta + g_{\nu\beta}(k_2+q)_\alpha + g_{\beta\alpha}(k_2'-q)_\nu) \to -g g_{\alpha\nu}(2-\alpha)k_{2\beta} \tag{4.46}$$

where we introduced the following Sudakov decomposition of q

$$q^\mu = \alpha \hat{k}_2^\mu + \beta v^\mu + q_\perp \tag{4.47}$$

with

$$\hat{k}_2^\mu = k_2^\mu - \frac{k_2^2}{2k_2\cdot v} v^\mu \ , \qquad \hat{k}_2^2 = 0 \ . \tag{4.48}$$

In equation (4.46) we first used the fact that we may replace $q^\mu \approx \alpha k_2^\mu$ in the numerator, up to terms that do not generate a logarithm. Following this, we used the transversality of the incoming gluons and the Higgs vertex to set $k_2^\nu, k_2^\alpha \to 0$. Now, doing the β integral by contour integration, we find

$$V^{ab}_{H\mu\nu}|_{4.9(\mathrm{a})} \approx -\frac{\alpha_s}{4\pi} C_A \int_0^1 d\alpha \int_{-(1-\alpha)\alpha k_2^2} \frac{dl_1^2}{l_1^2} \frac{(2-\alpha)}{\alpha} V^{ab}_{H\mu\nu} \,, \tag{4.49}$$

with $l_1^2 = \boldsymbol{q}_\perp^2 - (1-\alpha)\alpha k_2^2$. Note that, since we are only concerned with the logarithmic terms, we may replace the lower limit on the l_1^2 integral as $-(1-\alpha)\alpha k_2^2 \to -\alpha k_2^2$. The one-loop gluon propagator corrections (see for example [23]) give for figure 4.9(b)

$$V^{ab}_{H\mu\nu}|_{4.9(\mathrm{b})} \approx \frac{\alpha_s}{4\pi} \left(\frac{10}{12} C_A - \frac{2 T_F n_f}{3} \right) \int_{-k_2^2}^{\mu_R^2} \frac{dl_1^2}{l_1^2} V^{ab}_{H\mu\nu} \tag{4.50}$$

where μ_R is the renormalisation scale. The regions for which the emission is collinear to k_1 give an equal contribution and the full result may be written

$$\begin{aligned} \bar{V}_H|_{\text{n collinear emissions}} = -2 \int_0^1 dz \left(z\tilde{P}_{gg}(z) + n_f P_{qg}(z) \right) \int_{(1-z)\boldsymbol{Q}_\perp^2} \frac{dl_1^2}{l_1^2} \frac{\alpha_s(l_1^2)}{4\pi} \\ \times \bar{V}_H|_{\text{n-1 collinear emissions}} \end{aligned} \tag{4.51}$$

where we made the replacements $k_2^2 \approx -\boldsymbol{Q}_\perp^2$ and $\alpha = 1 - z$ and the tilde again indicates the splitting function without the plus prescription. As in section 2.5.3, the upper limit on the l_1^2 integral is l_2^2, the (shifted) transverse momentum of the next emission and the strong coupling now runs with l_1^2. These logarithmic corrections are going to generate the Sudakov factors, however, observe that the transverse momentum integral here extends down to $(1-z)\boldsymbol{Q}_\perp^2$. This is in contrast to the integral in the Sudakov factor, which is cut off at $\boldsymbol{Q}_\perp^2$, though note that the difference is only relevant for the $(1-z)^{-1}$ term in $\tilde{P}_{gg}(z)$. It appears then that, if we cut off the z-integral at $1 - z \sim q_\perp/m_H$ (see section 4.4.2), this piece will generate a Sudakov factor with twice the double logarithmic contribution of equation (4.13). This is not the case however. The contribution from the region

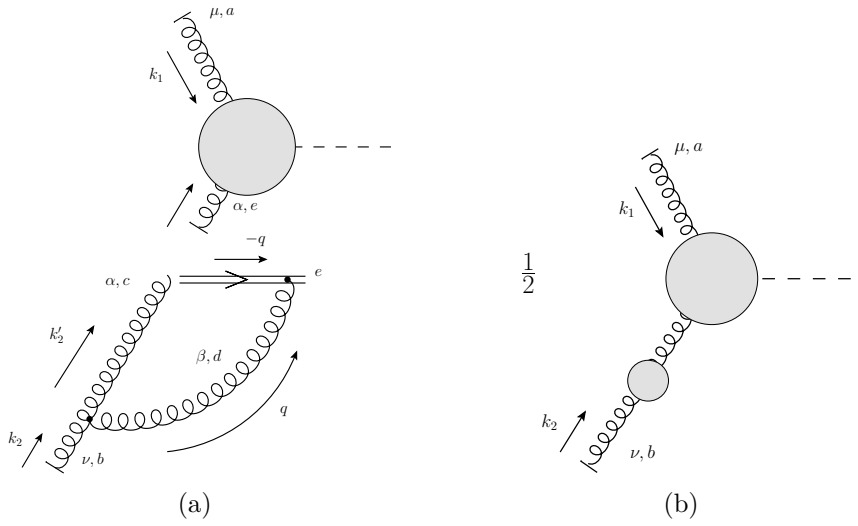

Figure 4.9: Form of large logarithmic corrections to V_H due to emissions collinear to k_2.

$q_\perp^2 < \boldsymbol{Q}_\perp^2$, with the $(1-z)^{-1}$ piece of $\tilde{P}_{gg}(z)$ generating a logarithm, is included in the BFKL corrections (which we have so far ignored) and as such, factorises into the unintegrated gluon pdfs. Furthermore, the infrared finiteness of the BFKL equation guarantees that there is in fact no large logarithm generated by the transverse momentum integral in this region. To illustrate these points a little more clearly, we shall now sketch the details of the argument, referring the reader to [28] for details of the BFKL formalism.

Consider the one-loop corrections to C^{qq} in the BFKL region, displayed in figure 4.10, where we calculate the amplitude from cuts as described in section 4.3. In this region, the full set of virtual correction to either side of the cut, which include the $q_\perp \sim |\boldsymbol{Q}_\perp|$ piece of $\bar{V}_H$ we have been discussing, are summed up in the Reggeised gluon propagator (denoted by a slash). In this case these corrections amount to the replacement in the lowest order graphs:

$$\frac{1}{Q^2(x_1 p_- Q)^2(x_2 p_2 + Q)^2} \to \frac{1}{Q^2(x_1 p_1 - Q)^2(x_2 p_2 + Q)^2} \left(\frac{s}{\boldsymbol{Q}_\perp^2}\right)^{2\epsilon_G(Q^2)} \tag{4.52}$$

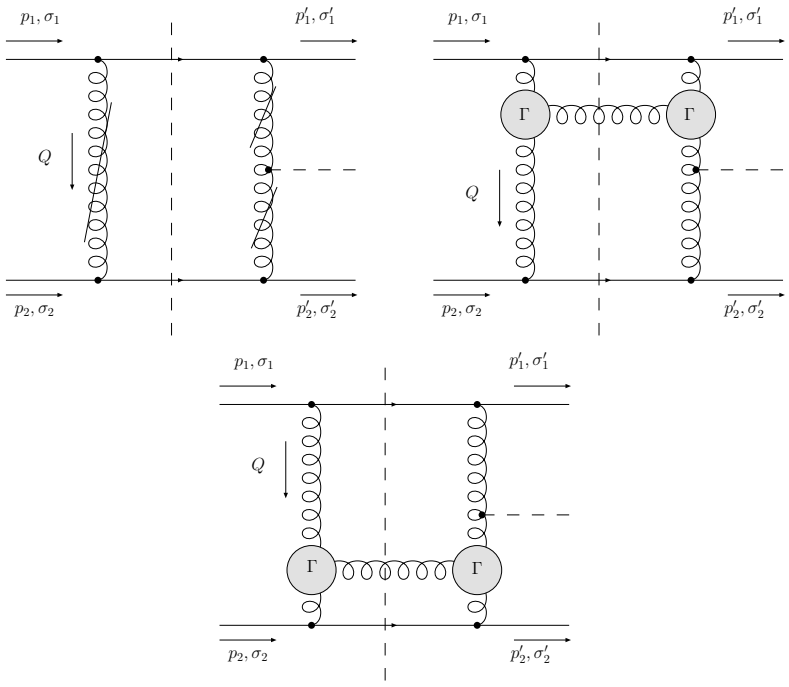

Figure 4.10: Next-to-leading order corrections to quark-quark central exclusive production in the BFKL formalism. Slashed gluon propagators and vertices labelled Γ indicate Reggeised gluons and Lipatov vertices respectively, see [28].

where the gluon Regge trajectory, $\epsilon_G(Q^2)$, is given by

$$\begin{aligned}\epsilon_G(Q^2) &= -\frac{C_A\alpha_s}{(2\pi)^{d-2}}\int d^{d-2}\boldsymbol{k}_\perp \frac{\boldsymbol{Q}_\perp^2}{\boldsymbol{k}_\perp^2(\boldsymbol{k}_\perp-\boldsymbol{Q}_\perp)^2} \\ &= -\frac{2C_A\alpha_s}{(2\pi)^{d-2}}\int d^{d-2}\boldsymbol{k}_\perp \frac{\boldsymbol{Q}_\perp^2}{(\boldsymbol{k}_\perp-\boldsymbol{Q}_\perp)^2[\boldsymbol{k}_\perp^2+(\boldsymbol{k}_\perp-\boldsymbol{Q}_\perp)^2]} \\ &= \frac{C_A\alpha_s}{2\pi}\frac{(4\pi)^\epsilon}{\Gamma(1-\epsilon)}\frac{(\boldsymbol{Q}_\perp^2)^{-\epsilon}}{\epsilon}\ . \end{aligned} \tag{4.53}$$

Note that the transverse momentum integral in $\epsilon_G(Q^2)$ only generates a logarithm for $k_\perp^2 < \boldsymbol{Q}_\perp^2$. So as stated, these corrections only include this region of the correction to $\bar{V}_H$. Since we take the $k_\perp$ integral down to zero, it is not clear precisely what logarithm is generated here, as we must introduce a regulator. However, we will show in a moment that this is irrelevant, since the divergence is cancelled. It will be instructive to observe how this form is built up in section 4.5.1, where we

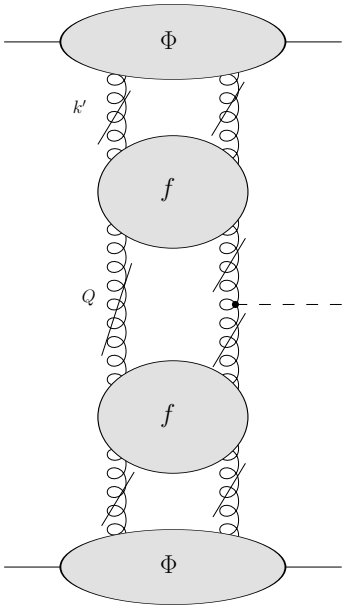

Figure 4.11: Schematic form of the central exclusive production amplitude in the BFKL formalism. The functions f are related to the four-gluon Green function and Φ are proton impact factors, see [28].

present a calculation of the next-to-leading order corrections to C^{qq}. The emissions crossing the cut are written in terms of the Lipatov vertex, $\Gamma^{\sigma}_{\mu\nu}$ (see [28] equation (3.11)).

These corrections are the first terms in the expansion of a non-perturbative function, $f(\omega, \boldsymbol{k}_\perp, \boldsymbol{Q}_\perp)$, related to the Green function with four off-shell gluons (see [28] equation (4.8))[3]. At all orders, in the BFKL limit, the amplitude may be written in terms of these functions, as depicted schematically in figure 4.11. These non-perturbative functions are then associated with the unintegrated gluon pdfs. We might still worry that we have a large logarithm generated by the region $k_\perp^2 < \boldsymbol{Q}_\perp^2$, however, we now show that this is not the case. The important point is that $f(\omega, \boldsymbol{k}_\perp, \boldsymbol{Q}_\perp)$ obeys an integral equation, the BFKL equation, shown

[3] ω is a Mellin transform variable, conjugate to the centre-of-mass energy.

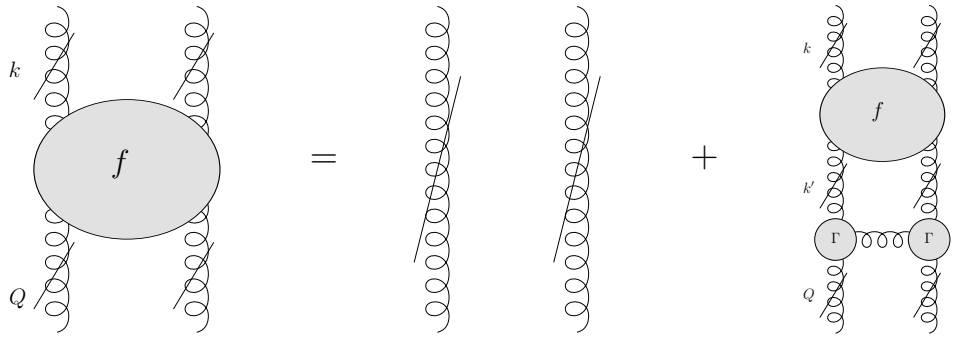

Figure 4.12: The BFKL integral equation in diagrammatic form.

diagrammatically in figure 4.12. This may be written

$$\begin{aligned}\omega f(\omega, \boldsymbol{Q}_\perp, \boldsymbol{k}_\perp) &= \delta^{(2)}(\boldsymbol{Q}_\perp - \boldsymbol{k}_\perp) + \frac{C_A \alpha_s}{\pi^2} \int \frac{d^2\boldsymbol{k}'_\perp}{(\boldsymbol{k}'_\perp - \boldsymbol{Q}_\perp)^2} f(\omega, \boldsymbol{k}'_\perp, \boldsymbol{k}_\perp) \\ &\quad + 2\epsilon_G(-\boldsymbol{Q}_\perp^2) f(\omega, \boldsymbol{Q}_\perp, \boldsymbol{k}_\perp) \\ &= \delta^{(2)}(\boldsymbol{Q}_\perp - \boldsymbol{k}_\perp) \\ &\quad + \frac{C_A \alpha_s}{\pi^2} \int \frac{d^2\boldsymbol{k}'_\perp}{(\boldsymbol{k}'_\perp - \boldsymbol{Q}_\perp)^2} \left(f(\omega, \boldsymbol{k}'_\perp, \boldsymbol{k}_\perp) - \frac{\boldsymbol{Q}_\perp^2 f(\omega, \boldsymbol{Q}_\perp, \boldsymbol{k}_\perp)}{[\boldsymbol{k}'^2_\perp + (\boldsymbol{k}'_\perp - \boldsymbol{Q}_\perp)^2]} \right)\end{aligned} \tag{4.54}$$

Now observe that, for $k'^2_\perp \ll \boldsymbol{Q}_\perp^2$, the first and second terms in parenthesis, corresponding to real and virtual corrections respectively, cancel one another. Thus we see that there is indeed no logarithm associated with the transverse momentum integral in this region.

The above is essentially the same argument, though presented in slightly different terms, that the Durham group use to set the lower limit on the Sudakov factor in equation (4.16). We will verify this argument explicitly in section 4.5.1, where we detail the results of a full next-to-leading order calculation of the virtual corrections which contribute to the Sudakov factor.

Returning to the previous discussion, we now note that, even after the replacement $(1-z)\boldsymbol{Q}_\perp^2 \to \boldsymbol{Q}_\perp^2$, equation (4.51) is incorrect as it stands, since the integral diverges in the soft limit, $z \to 1$. This is an artifact of our hard collinear

approximation however, for fixed, finite, transverse momentum, a soft gluon's energy cannot vanish. We shall discuss how this problem is rectified in the next section. For now, we ignore the divergence and iterate (4.51) until we are left with the tree level vertex:

$$\begin{aligned}\bar{V}_H = &\sum_{n=0}^{\infty}\prod_{i=1}^{n}\left(-\int_{\boldsymbol{Q}_\perp^2}^{l_{i+1}^2}\frac{dl_i^2}{l_i^2}\frac{\alpha_s(l_i^2)}{4\pi}\int_0^1 dz\left(z\tilde{P}_{gg}(z)+n_f P_{qg}(z)\right)\right)\\ &\times\sum_{\bar{n}=0}^{\infty}\prod_{\bar{i}=1}^{\bar{n}}\left(-\int_{\boldsymbol{Q}_\perp^2}^{\bar{l}_{i+1}^2}\frac{d\bar{l}_{\bar{i}}^2}{\bar{l}_{\bar{i}}^2}\frac{\alpha_s(\bar{l}_{\bar{i}}^2)}{4\pi}\int_0^1 dz\left(z\tilde{P}_{gg}(z)+n_f P_{qg}(z)\right)\right)\\ &\times\bar{\mathcal{M}}(gg\to H)\end{aligned} \tag{4.55}$$

where $l_{n+1}^2=\bar{l}_{\bar{n}+1}^2=m_H^2$ and $\bar{\mathcal{M}}$ is as defined in equation (4.9). We may then use the following identity for ordered integrals

$$\int_{\boldsymbol{Q}_\perp^2}^{l_2^2}dl_1^2\cdots\int_{\boldsymbol{Q}_\perp^2}^{m_H^2}dl_n^2=\frac{1}{n!}\prod_{j=1}^{n}\int_{\boldsymbol{Q}_\perp^2}^{m_H^2}dl_j^2 \tag{4.56}$$

which allows us to rewrite equation (4.55) in terms of exponentials

$$\begin{aligned}\bar{V}_H = &\exp\left[-\int_{\boldsymbol{Q}_\perp^2}^{m_H^2}\frac{dl^2}{l^2}\frac{\alpha_s(l^2)}{4\pi}\int_0^1 dz\left(z\tilde{P}_{gg}(z)+n_f P_{qg}(z)\right)\right]\\ &\times\exp\left[-\int_{\boldsymbol{Q}_\perp^2}^{m_H^2}\frac{d\bar{l}^2}{\bar{l}^2}\frac{\alpha_s(\bar{l}^2)}{4\pi}\int_0^1 dz\left(z\tilde{P}_{gg}(z)+n_f P_{qg}(z)\right)\right]\\ &\times\bar{\mathcal{M}}(gg\to H)\,.\end{aligned} \tag{4.57}$$

Thus we begin to see the emergence of the Sudakov factors. To go any further at this point we must include soft effects, to which we now turn.

4.4.2 Soft effects

The Sudakov factor

We shall begin our discussion of soft effects by dealing with the $z\to 1$ divergence in the Higgs vertex corrections. The softest gluon must attach to both gluons

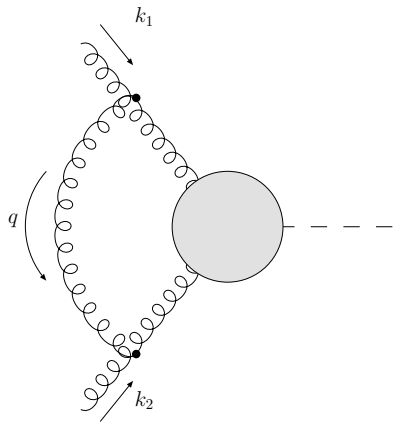

Figure 4.13: Form of the softest gluon attachment to the Higgs vertex.

fusing to produce the Higgs, as shown in figure 4.13. This contribution has the form

$$\bar{V}_H|_{\text{n soft emissions}} = \frac{iC_A g^2 m_H^2}{(2\pi)^4} \int d^2q_\perp \int d\alpha \int d\beta \times \frac{\bar{V}_H|_{\text{n-1 soft emissions}}}{[q^2+i\varepsilon][(q-k_1)^2+i\varepsilon][(q+k_2)^2+i\varepsilon]} \quad (4.58)$$

where

$$q^\mu = \alpha k_1^\mu + \beta k_2^\mu + q_\perp^\mu \, . \quad (4.59)$$

This diagram contains divergences both when q is collinear to k_1 and when it is collinear to k_2. In order to bring the result into the form of equation (4.51) we must separate out these two regions. An effective way to accomplish this is to multiply the integrand of (4.58) by

$$1 = \text{PV}\left(\frac{\alpha}{\alpha+\beta}\right) + \text{PV}\left(\frac{\beta}{\alpha+\beta}\right) \quad (4.60)$$

where PV denotes the Cauchy principal value. Now the term proportional to $\alpha/(\alpha+\beta)$ possesses only a collinear divergence with respect to k_1, whereas the other piece has only a collinear divergence when $q \propto k_2$. We may then perform the $\beta(\alpha)$ integrals in the first(second) term by contour integration. Only the piece

coming from the $[q^2 + i\varepsilon]$ pole is relevant to the $(1-z)^{-1}$ divergence. Keeping just this piece then, we obtain

$$\bar{V}_H|_{\text{n soft emissions}} = -\frac{\alpha_s}{2\pi} C_A \int \frac{d\boldsymbol{q}_\perp^2}{\boldsymbol{q}_\perp^2} \left(\int_0^1 d\alpha \frac{1}{\alpha + \frac{\boldsymbol{q}_\perp^2}{\alpha m_H^2}} + \int_0^1 d|\beta| \frac{1}{|\beta| + \frac{\boldsymbol{q}_\perp^2}{|\beta| m_H^2}} \right) \times \bar{V}_H|_{\text{n-1 soft emissions}} \tag{4.61}$$

Changing variables as $\alpha = 1 - z$, $|\beta| = 1 - z$ and noting that the momentum fraction integrals are effectively cutoff at $|\boldsymbol{q}_\perp|/m_H$, this becomes

$$\bar{V}_H|_{\text{n soft emissions}} = -2\frac{\alpha_s}{2\pi} C_A \int \frac{d\boldsymbol{q}_\perp^2}{\boldsymbol{q}_\perp^2} \int_0^{1-|\boldsymbol{q}_\perp|/m_H} \frac{dz}{1-z} \bar{V}_H|_{\text{n-1 soft emissions}} \tag{4.62}$$

and so equation (4.57) becomes

$$\bar{V}_H = T(\boldsymbol{Q}_\perp, m_H) \bar{\mathcal{M}}(gg \to H) \, . \tag{4.63}$$

Note that, as stated earlier, this result differs from the Durham group's. In section 4.5 we shall provide further evidence that this is indeed the correct form of the Sudakov factor and not equations (4.13)-(4.15).

The Sudakov derivative

We now turn our attention to a proper treatment of the (unregularised) splitting kernels entering due to the final two s-channel emissions. The only issue is with the K^{gg} kernel, which diverges in the soft limit ($w_1 \to y_1$ or $w_2 \to y_2$). In order to understand how to treat this region correctly we focus on the final emission collinear to the upper hadron, assuming all previous emissions have been collected into the pdf.

As discussed in section 4.3, we may compute the amplitude by taking the cuts shown in figures 4.3(a) and 4.3(e) only. Furthermore, if we wish to study the soft limit of the final emission, only the diagrams shown in figure 4.14 and the analogous diagrams with the Higgs emitted on the other side of the cut, will

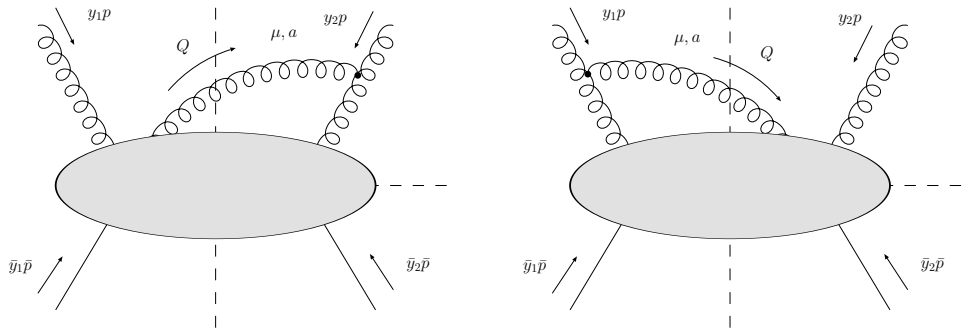

Figure 4.14: Diagrams for the last emission collinear to the upper hadron which generate the soft part of the splitting kernel.

contribute. Since we are only interested in the limit in which Q is soft we may simplify these diagrams further and only consider the sub-set in which Q attaches to on-shell particles. The result is then given by the soft insertion rules (see for example [69]). After summing the two diagrams in figure 4.14, for example, the amplitude to the left of the cut, $|L_1\rangle^{\mu,a}$, may be written

$$|L_1\rangle^{\mu,a} = \sum_{i=0}^{n+1} \left(\frac{-g l_i^\mu}{l_i \cdot Q} \right) \boldsymbol{T}_{l_i}^a |L_0\rangle \tag{4.64}$$

where $l_0 = y_1 p$, $l_{n+1} = \bar{y}_2 \bar{p}$ and the other l_i are the momenta of the particles crossing the cut. The amplitude without the soft gluon is represented by $|L_0\rangle$. Since Q is the last emission collinear to the upper proton, we may take $l_i \propto \bar{p}$ for $i \neq 0$. Including the amplitude to the right of the cut, $|R_1\rangle$, using the same soft insertion formula and including an integration over the intermediate phase-space, we obtain

$$\begin{aligned} A|_{4.14} = &- \int d(PS^n) \int \frac{d^4Q}{(2\pi)^3} \delta_{(+)}(Q^2) \frac{g^2 p \cdot \bar{p}}{p \cdot Q \bar{p} \cdot Q} \\ &\times \sum_{i=1}^{n+1} \left(\langle R_0 | \left(\boldsymbol{T}_{l_i}^a\right)^\dagger \boldsymbol{T}_{l_0}^a |L_0\rangle + \langle R_0 | \left(\boldsymbol{T}_{l_0}^a\right)^\dagger \boldsymbol{T}_{l_i}^a |L_0\rangle \right) \end{aligned} \tag{4.65}$$

where $d(PS^n)$ is the phase-space of the cut diagram without the soft gluon. Then,

using colour conservation:

$$\sum_{i=1}^{n+1} \boldsymbol{T}_{l_i}^a = -\boldsymbol{T}_{l_0}^a \ , \tag{4.66}$$

$$(\boldsymbol{T}_{l_0}^a)^\dagger \boldsymbol{T}_{l_0}^a = C_A \ , \tag{4.67}$$

we find

$$A|_{4.14} = \int d(PS^n) \int \frac{d^4Q}{(2\pi)^3} \delta_{(+)}(Q^2) \frac{C_A g^2 p\cdot\bar{p}}{p\cdot Q \bar{p}\cdot Q} 2 \left\langle R_0 | L_0 \right\rangle \ . \tag{4.68}$$

Now note that (4.68) possesses divergences when Q becomes collinear to either p or $\bar{p}$. As in the case of the Sudakov factor, we may separate out these regions by multiplying the integrand by $1 = (\alpha+\beta)/(\alpha+\beta)$, where this time

$$Q^\mu = \alpha p^\mu + \beta \bar{p}^\mu + Q_\perp^\mu \ . \tag{4.69}$$

Since we are interested in the divergences with respect to the upper hadron, we keep only the $\alpha/(\alpha+\beta)$ piece. The only effect of the phase-space on Q is to introduce the constraint $\Theta(y_1 p^+ - Q^+)$. Thus, (4.68) becomes:

$$A|_{4.14} = \frac{2g^2 C_A}{(2\pi)^3} \int \frac{d^2\boldsymbol{Q}_\perp}{\boldsymbol{Q}_\perp^2} \int_0^{y_1} d\alpha \frac{1}{\alpha + \frac{\boldsymbol{Q}_\perp^2}{4\alpha s}} \int d(PS^n) \left\langle R_0 | L_0 \right\rangle \ . \tag{4.70}$$

Comparing this to the results obtained in section 2.5.3, by taking the limit $x_i \to y_i$ in equation (2.69), we see that the correct form of the unregularised splitting kernel is

$$\begin{aligned} \tilde{K}_{(0)}^{gg}(x_1,x_2|y_1,y_2) = C_A \Bigg[& \frac{x_1}{y_1} \frac{x_1\, \vartheta_{11}^0(x_1, x_1-y_1)}{\left(x_1 - y_1 + \frac{\boldsymbol{Q}_\perp^2}{(x_1-y_1)4s}\right)} \\ & + \frac{x_2}{y_2} \frac{x_2\, \vartheta_{11}^0(x_2, x_2-y_2)}{\left(x_2 - y_2 + \frac{\boldsymbol{Q}_\perp^2}{(x_2-y_2)4s}\right)} \\ & + 2\frac{x_1x_2 + y_1y_2}{y_1y_2} \vartheta_{111}^0(x_1, -x_2, x_1-y_1) \\ & + 2\frac{x_1x_2}{y_1y_2} \frac{x_1y_1 + x_2y_2}{(x_1+x_2)^2} \vartheta_{11}^0(x_1,-x_2) \Bigg] \ . \end{aligned} \tag{4.71}$$

To the soft divergent pieces here we may now add and subtract a term proportional to a delta-function:

$$\frac{x}{y}\frac{x\,\vartheta_{11}^0(x,x-y)}{\left(x-y+\frac{\boldsymbol{Q}_\perp^2}{(x-y)4s}\right)} = \frac{x}{y}\left[\frac{x\,\vartheta_{11}^0(x,x-y)}{\left(x-y+\frac{\boldsymbol{Q}_\perp^2}{(x-y)4s}\right)} - \delta(x-y)\int dx' \frac{x'\vartheta_{11}^0(x',x'-y)}{\left(x'-y+\frac{\boldsymbol{Q}_\perp^2}{(x'-y)4s}\right)}\right] + \delta(x-y)\int dx' \frac{x'\vartheta_{11}^0(x',x'-y)}{\left(x'-y+\frac{\boldsymbol{Q}_\perp^2}{(x'-y)4s}\right)}\,. \tag{4.72}$$

In the first term, contained in square brackets, we may take the $\boldsymbol{Q}_\perp \to 0$ limit since the soft region cancels, leaving us with something regularised by the plus-prescription. The integral in the second term may be done explicitly, giving a logarithm plus non-logarithmic terms which we neglect. Substituting this identity into equation (4.71) it becomes

$$\tilde{K}^{gg}(x_1,x_2|y_1,y_2) = K^{gg}(x_1,x_2|y_1,y_2) - \frac{\alpha_s}{4\pi}C_A\delta(x_1-y_1)\ln\left(\frac{4y_1^2s+\boldsymbol{Q}_\perp^2}{\boldsymbol{Q}_\perp^2}\right) - \frac{\alpha_s}{4\pi}C_A\delta(x_2-y_2)\ln\left(\frac{4y_2^2s+\boldsymbol{Q}_\perp^2}{\boldsymbol{Q}_\perp^2}\right)\,. \tag{4.73}$$

Applying this to the splitting kernels appearing in equation (4.43) gives, for example

$$\tilde{K}^{ga}\left(\frac{x_1}{2},0\middle|y_1,y_2\right) = K^{ga}\left(\frac{x_1}{2},0\middle|y_1,y_2\right) - \delta^{ga}\frac{\alpha_s}{2\pi}C_A\delta\left(\xi-\frac{x_1}{2}\right)\ln\left(\frac{m_H^2}{\boldsymbol{Q}_\perp^2}\right) \tag{4.74}$$

where we replaced $x_1^2 s \to m_H^2$, which is correct to logarithmic accuracy. This logarithm in the Higgs mass may then be written in terms of the derivative of the Sudakov factor:

$$\tilde{K}^{ga}\left(\frac{x_1}{2},0\middle|y_1,y_2\right) = K^{ga}\left(\frac{x_1}{2},0\middle|y_1,y_2\right) - \delta^{ga}\delta\left(\xi-\frac{x_1}{2}\right)\frac{2}{\sqrt{T(\boldsymbol{Q}_\perp,m_H)}}\frac{\partial\sqrt{T(\boldsymbol{Q}_\perp,m_H)}}{\partial\ln(\boldsymbol{Q}_\perp^2)}\,. \tag{4.75}$$

All together then, including the Sudakov factor, equation (4.44) becomes

$$\begin{aligned}\mathcal{A}_{\rm CEP} \approx \int \frac{d\boldsymbol{Q}_\perp^2}{\boldsymbol{Q}_\perp^4} \frac{\partial}{\partial \ln(\boldsymbol{Q}_\perp^2)} \left[H_g\left(\frac{x_1}{2}, \frac{x_1}{2}; \boldsymbol{Q}_\perp^2\right) \sqrt{T(\boldsymbol{Q}_\perp, m_H)} \right] \\ \times \frac{\partial}{\partial \ln(\boldsymbol{Q}_\perp^2)} \left[H_g\left(\frac{x_2}{2}, \frac{x_2}{2}; \boldsymbol{Q}_\perp^2\right) \sqrt{T(\boldsymbol{Q}_\perp, m_H)} \right] \\ \times \frac{\pi^3 2^4 (-i)}{x_1 x_2 (N^2-1)} \bar{\mathcal{M}}(gg \to H) \,. \end{aligned} \tag{4.76}$$

Finally, using equation (4.12) and assuming that R_g depends only weakly on $\boldsymbol{Q}_\perp^2$, we find:

$$\begin{aligned}\mathcal{A}_{\rm CEP} \approx \int \frac{d\boldsymbol{Q}_\perp^2}{\boldsymbol{Q}_\perp^4} f_g(x_1, 0, \boldsymbol{Q}_\perp^2, m_H^2) f_g(x_2, 0, \boldsymbol{Q}_\perp^2, m_H^2) \\ \times \frac{\pi^3 2^4 (-i)}{x_1 x_2 (N^2-1)} \bar{\mathcal{M}}(gg \to H) \,. \end{aligned} \tag{4.77}$$

4.5 Fixed order calculations of Higgs production

4.5.1 Explicit next-to-leading order calculation

Having discussed the result at all orders, we now turn to a description of our next-to-leading order calculation of the amplitude for two quarks of different flavour to scatter into two quarks and a Higgs. This calculation will serve as an explicit check of the all orders result presented in the previous section and also offers the possibility to extend the Durham result to next-to-leading order accuracy[4].

As stated in section 4.3, we may calculate the amplitude from the cuts 4.3(a), 4.3(e). We limit ourselves to a calculation of the virtual corrections to one side of a cut; it is the Sudakov factor we are interested in probing here and we expect only this set of diagrams to contribute to it. After presenting our results we shall

[4]The Durham group do include a K-factor in their calculation of central exclusive Higgs production [46], taken from the calculation of inclusive Higgs production at next-to-leading order [70, 71]. They do not however explicitly evaluate the next-to-leading order contribution.

comment on why the diagrams with an additional gluon crossing the cut cannot contribute to the Sudakov factor.

The set of diagrams we must calculate when the Higgs is to the right of the cut are shown in figure 4.15, with a similar set for the Higgs to the left of the cut not shown. All other diagrams may be obtained by exchanging x_1 and x_2. We perform the loop integrals using the techniques described in chapter 3 which we have implemented using the programs Mathematica [72] and FORM [73]. We also use the Mathematica package FeynCalc [74] to simplify the numerator algebra. All of our calculations are performed in Feynman gauge and using the large top mass effective theory described in appendix B.

In addition, we keep only terms not suppressed by additional powers of x_i or $\boldsymbol{Q}_\perp^2$, relative to the lowest order case. The cut sets

$$Q^\pm \approx \frac{\pm \boldsymbol{Q}_\perp^2}{\sqrt{2s}} \tag{4.78}$$

and we may also make the approximation

$$\bar{\Psi}^{(+)}_{p_i',\sigma_i} \approx \bar{\Psi}^{(+)}_{p_i,\sigma_i} \,, \tag{4.79}$$

for the final-state quark spinor wavefunctions. This allows us to make the replacement

$$\Psi^{(+)}_{p_i,\sigma_i} \bar{\Psi}^{(+)}_{p_i',\sigma_i} \to \frac{\not{p}_i}{2} \tag{4.80}$$

where we have dropped a term proportional to γ^5, which is not relevant since the amplitude is CP-invariant. We shall also present here only those terms either enhanced by a logarithm or divergent as $\epsilon \to 0$.

Working in dimensional regularisation, with $d = 4-2\epsilon$ space-time dimensions,

the results for each cut diagram are

$$C_{\rm NLO}|_{4.15(a)} = A_0(\mu)\int\frac{d\boldsymbol{Q}_\perp^2}{\boldsymbol{Q}_\perp^4}\frac{C_A\alpha_s}{\pi}\left(\frac{11\mathcal{N}}{12\epsilon}+\frac{11}{12}\ln\left(\frac{\mu^2}{\boldsymbol{Q}_\perp^2}\right)-\frac{1}{2}\ln^2\left(\frac{m_H^2}{\boldsymbol{Q}_\perp^2}\right)\right.$$
$$+\left(\frac{3}{8}-i\pi\right)\ln\left(\frac{m_H^2}{\boldsymbol{Q}_\perp^2}\right)+\frac{m_H^2}{\boldsymbol{Q}_\perp^2}\left[\frac{7\mathcal{N}}{24\epsilon}\right.$$
$$\left.\left.+\frac{7}{24}\ln\left(\frac{\mu^2}{m_H^2}\right)-\frac{7i\pi}{24}+\frac{49}{144}\right]\right) \tag{4.81}$$

$$C_{\rm NLO}|_{4.15(b)} = A_0(\mu)\int\frac{d\boldsymbol{Q}_\perp^2}{\boldsymbol{Q}_\perp^4}\frac{C_A\alpha_s}{\pi}\left(-\frac{19\mathcal{N}}{48\epsilon}-\frac{19}{48}\ln\left(\frac{\mu^2}{\boldsymbol{Q}_\perp^2}\right)\right) \tag{4.82}$$

$$C_{\rm NLO}|_{4.15(c)} = A_0(\mu)\int\frac{d\boldsymbol{Q}_\perp^2}{\boldsymbol{Q}_\perp^4}\frac{C_A\alpha_s}{\pi}\frac{m_H^2}{\boldsymbol{Q}_\perp^2}\left(-\frac{7\mathcal{N}}{24\epsilon}-\frac{7}{24}\ln\left(\frac{\mu^2}{m_H^2}\right)+\frac{7i\pi}{24}-\frac{49}{144}\right) \tag{4.83}$$

$$C_{\rm NLO}|_{4.15(d)} = A_0(\mu)\int\frac{d\boldsymbol{Q}_\perp^2}{\boldsymbol{Q}_\perp^4}\frac{C_A\alpha_s}{\pi}\left(-\frac{\mathcal{N}}{8\epsilon}-\frac{1}{8}\ln\left(\frac{\mu^2}{\boldsymbol{Q}_\perp^2}\right)\right) \tag{4.84}$$

$$C_{\rm NLO}|_{4.15(e)} = A_0(\mu)\int\frac{d\boldsymbol{Q}_\perp^2}{\boldsymbol{Q}_\perp^4}(C_A-2C_F)\frac{\alpha_s}{\pi}\left(\frac{\mathcal{N}}{4\epsilon^2}\left(\frac{\mu^2}{\boldsymbol{Q}_\perp^2}\right)^\epsilon+\frac{3\mathcal{N}}{8\epsilon}+\frac{3}{8}\ln\left(\frac{\mu^2}{\boldsymbol{Q}_\perp^2}\right)\right) \tag{4.85}$$

$$C_{\rm NLO}|_{4.15(f)} = A_0(\mu)\int\frac{d\boldsymbol{Q}_\perp^2}{\boldsymbol{Q}_\perp^4}(5C_A-2n_f)\frac{\alpha_s}{\pi}\left(\frac{\mathcal{N}}{12\epsilon}+\frac{1}{12}\ln\left(\frac{\mu^2}{\boldsymbol{Q}_\perp^2}\right)\right) \tag{4.86}$$

$$C_{\rm NLO}|_{4.15(g)} = A_0(\mu)\int\frac{d\boldsymbol{Q}_\perp^2}{\boldsymbol{Q}_\perp^4}\left(\frac{C_A\alpha_s}{32\pi}\frac{\mathcal{N}}{\epsilon}+\frac{C_A\alpha_s}{32\pi}\ln\left(\frac{\mu^2}{m_H^2}\right)+\frac{C_A\alpha_s}{8\pi}\ln^2\left(\frac{m_H^2}{\boldsymbol{Q}_\perp^2}\right)\right.$$
$$+\frac{C_A\alpha_s}{16\pi}(4i\pi-1)\ln\left(\frac{m_H^2}{\boldsymbol{Q}_\perp^2}\right)+\frac{C_A\alpha_s}{16\pi}\ln(x_1)$$
$$\left.+\frac{\epsilon_G(Q^2)}{2}\left(\ln\left(\frac{x_2 s}{\boldsymbol{Q}_\perp^2}\right)+i\pi\right)\right) \tag{4.87}$$

$$C_{\rm NLO}|_{4.15(\rm h)} = A_0(\mu)\int\frac{d\boldsymbol{Q}_\perp^2}{\boldsymbol{Q}_\perp^4}\left(\frac{C_A\alpha_s}{32\pi}\frac{\mathcal{N}}{\epsilon}+\frac{C_A\alpha_s}{32\pi}\ln\left(\frac{\mu^2}{m_H^2}\right)+\frac{C_A\alpha_s}{8\pi}\ln^2\left(\frac{m_H^2}{\boldsymbol{Q}_\perp^2}\right)\right.$$
$$+\frac{C_A\alpha_s}{16\pi}(4i\pi-1)\ln\left(\frac{m_H^2}{\boldsymbol{Q}_\perp^2}\right)+\frac{C_A\alpha_s}{16\pi}\ln(x_1)$$
$$\left.+\frac{\epsilon_G(Q^2)}{2}\ln\left(\frac{x_2 s}{\boldsymbol{Q}_\perp^2}\right)\right) \tag{4.88}$$

$$C_{\rm NLO}|_{4.15(\rm i)} = A_0(\mu)\int\frac{d\boldsymbol{Q}_\perp^2}{\boldsymbol{Q}_\perp^4}\frac{C_A\alpha_s}{\pi}\left(\frac{\mathcal{N}}{8\epsilon}+\frac{1}{8}\ln\left(\frac{\mu^2}{\boldsymbol{Q}_\perp^2}\right)\right) \tag{4.89}$$

$$C_{\rm NLO}|_{4.15(\rm j)} = A_0(\mu)\int\frac{d\boldsymbol{Q}_\perp^2}{\boldsymbol{Q}_\perp^4}(C_A-2C_F)\frac{\alpha_s}{8\pi}\ln\left(\frac{1}{x_1}\right) \tag{4.90}$$

$$C_{\rm NLO}|_{4.15(\rm k)} = C_{\rm NLO}|_{4.15(\rm l)} = A_0(\mu)\int\frac{d\boldsymbol{Q}_\perp^2}{\boldsymbol{Q}_\perp^4}\frac{C_F\alpha_s}{8\pi}\ln\left(\frac{1}{x_1}\right) \tag{4.91}$$

$$C_{\rm NLO}|_{4.15(\rm m)} = A_0(\mu)\int\frac{d\boldsymbol{Q}_\perp^2}{\boldsymbol{Q}_\perp^4}\left(-\frac{1}{N}\right)\left(\frac{\alpha_s}{2\pi}\frac{\mathcal{N}}{\epsilon^2}\left(\frac{\mu^2}{\boldsymbol{Q}_\perp^2}\right)^\epsilon+\frac{\alpha_s}{4\pi}\ln^2\left(\frac{m_H^2}{\boldsymbol{Q}_\perp^2}\right)\right.$$
$$\left.+\frac{\alpha_s}{2\pi}i\pi\ln\left(\frac{m_H^2}{\boldsymbol{Q}_\perp^2}\right)+\frac{\epsilon_G(Q^2)}{C_A}\left(\ln\left(\frac{m_H^2}{\boldsymbol{Q}_\perp^2}\right)+i\pi\right)\right) \tag{4.92}$$

$$C_{\rm NLO}|_{4.15(\rm n)} = C_{\rm NLO}|_{4.15(\rm m)} + A_0(\mu)\int\frac{d\boldsymbol{Q}_\perp^2}{\boldsymbol{Q}_\perp^4}\frac{i\pi}{N}\frac{\alpha_s}{\pi}\left(\frac{\mathcal{N}}{2\epsilon}+\frac{1}{2}\ln\left(\frac{\mu^2}{\boldsymbol{Q}_\perp^2}\right)\right) \tag{4.93}$$

$$C_{\rm NLO}|_{4.15(\rm o)} = C_{\rm NLO}|_{4.15(\rm p)} = A_0(\mu)\int\frac{d\boldsymbol{Q}_\perp^2}{\boldsymbol{Q}_\perp^4}\left(\frac{1}{N}-\frac{C_A}{2}\right)\left(\frac{\alpha_s}{2\pi}\frac{\mathcal{N}}{\epsilon^2}\left(\frac{\mu^2}{\boldsymbol{Q}_\perp^2}\right)^\epsilon\right.$$
$$+\frac{\alpha_s}{4\pi}\ln^2\left(\frac{m_H^2}{\boldsymbol{Q}_\perp^2}\right)+\frac{\alpha_s}{2\pi}i\pi\ln\left(\frac{m_H^2}{\boldsymbol{Q}_\perp^2}\right)$$
$$\left.+\frac{\epsilon_G(Q^2)}{C_A}\left(\ln\left(\frac{m_H^2}{\boldsymbol{Q}_\perp^2}\right)+i\pi\right)\right) \tag{4.94}$$

$$C_{\rm NLO}|_{4.15({\rm q})} = A_0(\mu)\int\frac{d\boldsymbol{Q}_\perp^2}{\boldsymbol{Q}_\perp^4}\frac{1}{N}\left(-\frac{\alpha_s}{\pi}\frac{\mathcal{N}}{\epsilon^2}\left(\frac{\mu^2}{\boldsymbol{Q}_\perp^2}\right)^\epsilon + \frac{2\epsilon_G(Q^2)}{C_A}\left(\ln\left(\frac{s}{\boldsymbol{Q}_\perp^2}\right) - i\pi\right)\right) \tag{4.95}$$

$$C_{\rm NLO}|_{4.15({\rm r})} = A_0(\mu)\int\frac{d\boldsymbol{Q}_\perp^2}{\boldsymbol{Q}_\perp^4}\left(\frac{C_A}{2}-\frac{1}{N}\right)\left(-\frac{\alpha_s}{\pi}\frac{\mathcal{N}}{\epsilon^2}\left(\frac{\mu^2}{\boldsymbol{Q}_\perp^2}\right)^\epsilon + \frac{2\epsilon_G(Q^2)}{C_A}\ln\left(\frac{s}{\boldsymbol{Q}_\perp^2}\right)\right) \tag{4.96}$$

$$C_{\rm NLO}|_{4.15({\rm s})} = C_{\rm NLO}|_{4.15({\rm d})} \tag{4.97}$$

$$C_{\rm NLO}|_{4.15({\rm t})} = C_{\rm NLO}|_{4.15({\rm e})} \tag{4.98}$$

$$C_{\rm NLO}|_{4.15({\rm u})} = C_{\rm NLO}|_{4.15({\rm f})} \tag{4.99}$$

where the usual $\overline{\rm MS}$ factor is given by

$$\mathcal{N} = \exp\left[\epsilon(-\gamma_E + \ln(4\pi))\right] \tag{4.100}$$

and γ_E is the Euler-Mascheroni constant. The full set of counter terms for the diagrams with the Higgs to the right of the cut give

$$C_{\rm NLO}|_{\rm counter\ terms} = A_0(\mu)\int\frac{d\boldsymbol{Q}_\perp^2}{\boldsymbol{Q}_\perp^4}\left(-3\beta_0\frac{\alpha_s}{\pi}\frac{\mathcal{N}}{\epsilon}\right)\ , \tag{4.101}$$

where β_0 is the first component of the QCD beta-function and is given by

$$\beta_0 = \frac{11C_A - 4T_F n_f}{12}\ . \tag{4.102}$$

Collecting these results together and including those related by interchanging $x_1 \leftrightarrow x_2$ and those generated by the diagrams with the Higgs to the left of the

cut, we obtain

$$A_{\rm NLO} = A_0(\mu)\int \frac{d\boldsymbol{Q}_\perp^2}{\boldsymbol{Q}_\perp^4}\left(-2C_F\frac{\alpha_s}{\pi}\frac{\mathcal{N}}{\epsilon^2}\left(\frac{\mu^2}{\boldsymbol{Q}_\perp^2}\right)^\epsilon - 3C_F\frac{\alpha_s}{\pi}\frac{\mathcal{N}}{\epsilon}\left(\frac{\mu^2}{\boldsymbol{Q}_\perp^2}\right)^\epsilon \right.$$
$$- C_A\frac{\alpha_s}{4\pi}\ln^2\left(\frac{m_H^2}{\boldsymbol{Q}_\perp^2}\right) + 3\beta_0\frac{\alpha_s}{\pi}\ln\left(\frac{\mu^2}{\boldsymbol{Q}_\perp^2}\right)$$
$$\left. +2\epsilon_G(Q^2)\ln\left(\frac{s}{\boldsymbol{Q}_\perp^2}\right)\right)\ . \qquad (4.103)$$

The $1/\epsilon$ poles here are due to collinear and soft divergences and may be written in terms of the quark-quark splitting function using the following identity

$$C_F\left(\frac{(\boldsymbol{Q}_\perp^2)^{-\epsilon}}{\epsilon^2} + \frac{3}{2}\frac{(\boldsymbol{Q}_\perp^2)^{-\epsilon}}{\epsilon}\right) \approx \int_0^{\boldsymbol{Q}_\perp^2}\frac{dq_\perp^2}{(q_\perp^2)^{1+\epsilon}}\int_0^{1-q_\perp/|\boldsymbol{Q}_\perp|} dz\ P_{qq}(z) \qquad (4.104)$$

which holds up to terms not involving either $1/\epsilon$ poles or logarithms of $\boldsymbol{Q}_\perp$. Each of these factors, proportional to P_{qq}, is due to a parton becoming collinear with one of the, on-mass-shell, external quark lines. The (final state) contributions associated with the cut quark lines will cancel with an equal and opposite term coming from final-state divergences associated with a gluon emitted across the cut. If we take $\mu^2 = \boldsymbol{Q}_\perp^2$, then the remaining factors of P_{qq} are simply the virtual contribution to the expansion of the pdf, $H_q(\boldsymbol{Q}_\perp^2)$. Finally, we see the factor associated with the Reggeisation of the gluon, written in terms of the gluon Regge trajectory (see equations 4.52 and 4.53). This has precisely the form predicted in equation (4.52) and is also expected to factorise into the unintegrated gluon pdf.

What remains then, after accounting for all of these pieces, must be the $\mathcal{O}(\alpha_s)$ expansion of the Sudakov factor:

$$A_{\rm NLO}|_{\rm Sudakov} = \int\frac{d\boldsymbol{Q}_\perp^2}{\boldsymbol{Q}_\perp^4}A_0(\boldsymbol{Q}_\perp)\left(-C_A\frac{\alpha_s(\boldsymbol{Q}_\perp^2)}{4\pi}\ln^2\left(\frac{m_H^2}{\boldsymbol{Q}_\perp^2}\right)\right)\ . \qquad (4.105)$$

It is interesting to see which diagrams this double logarithm derives from. If we simply took the vertex correction of figure 4.15(a), we would obtain twice the double logarithmic contribution we have in the full answer, consistent with our discussion of the corrections to $\bar{V}_H$ in section 4.4.1. This additional double

logarithm is cancelled when we include the diagrams 4.15(g), 4.15(h) and 4.15(m)-4.15(p) (and those related by $x_1 \leftrightarrow x_2$). It is also the sum of these diagrams which generates the Reggeisation of the gluons to the right of the cut.

In order to compare equation (4.105) to the Durham result, we must first exchange $A_0(\boldsymbol{Q}_\perp)$ for $A_0(m_H)$. This may be accomplished using the leading order coupling constant evolution

$$\alpha_s(\mu_1^2) = \alpha_s(\mu_2^2) \exp\left[-\int_{\mu_2^2}^{\mu_1^2} \frac{dk_\perp^2}{k_\perp^2} \frac{\alpha_s(k_\perp^2)}{\pi} \beta_0\right] \tag{4.106}$$

which implies at next-to-leading order

$$A_0(\boldsymbol{Q}_\perp) = A_0(m_H)\left(1 + \int_{\boldsymbol{Q}_\perp^2}^{m_H^2} \frac{dk_\perp^2}{k_\perp^2} \frac{\alpha_s(k_\perp^2)}{\pi} \beta_0\right) \tag{4.107}$$

and thus

$$\begin{aligned} A_{\mathrm{NLO}}|_{\mathrm{Sudakov}} &= \int \frac{d\boldsymbol{Q}_\perp^2}{\boldsymbol{Q}_\perp^4} A_0(m_H)\left(-C_A \frac{\alpha_s(\boldsymbol{Q}_\perp^2)}{4\pi} \ln^2\left(\frac{m_H^2}{\boldsymbol{Q}_\perp^2}\right) + \int_{\boldsymbol{Q}_\perp^2}^{m_H^2} \frac{dk_\perp^2}{k_\perp^2} \frac{\alpha_s(k_\perp^2)}{\pi} \beta_0\right) \\ &\approx \int \frac{d\boldsymbol{Q}_\perp^2}{\boldsymbol{Q}_\perp^4} A_0(m_H) \ln\left(T(\boldsymbol{Q}_\perp, m_H)\right) \ . \end{aligned} \tag{4.108}$$

This is exactly the next-to-leading order term one would obtain by expanding out the Sudakov factor (with $\Delta = k_\perp/m_H$) to this order in perturbation theory.

In obtaining this result we have of course neglected the diagrams in which a gluon is emitted across the cut. However, we now argue that such terms cannot possibly contribute to the Sudakov factor.

There are three regions for these diagrams which could potentially produce a logarithm in $m_H^2/\boldsymbol{Q}_\perp^2$. First are the BFKL corrections. However, these are summed into the unintegrated pdfs and so cannot contribute to the Sudakov factor. Secondly, we have hard collinear emission. This was fully accounted for in section 4.4.1, where we saw that the only large logarithms generated by s-channel emissions in this region had transverse momentum less than $\boldsymbol{Q}_\perp$ and so do not form part of the Sudakov factor. Finally then, we have soft emission. To

be included in the Sudakov factor, the additional soft gluon must have a larger transverse momentum than one of the quarks. However, this means it is one of the final two s-channel emissions making up $C_{2\text{ s-channel}}^{qq}$. As shown in section 4.4.2, these soft emissions generate the Sudakov derivative.

With these considerations then, we see that equation (4.108) gives the full contribution to the Sudakov factor at this order in perturbation theory. With this result we have demonstrated that our all-orders Sudakov factor, equation (4.63), is correct and that the Durham Sudakov must be modified by the replacement $\mu = 0.62 m_H \to m_H$. In order to further confirm this result we shall, in the next section, describe a recalculation of the $gg \to Hg$ process, which the Durham group used to derive equation (4.13).

4.5.2 Recalculation of the Sudakov factor in the Durham approach

We now discuss our recalculation of the Sudakov factor using the Durham group's approach. The set of diagrams making up the $gg \to gH$ amplitude is shown in figure 4.16. The cross-section is given by

$$\sigma = \int d\xi_1 \int d\xi_2 \; g(\xi_1;\mu_F^2) g(\xi_2;\mu_F^2) \frac{1}{2\hat{s}} \frac{\hat{s}}{2} \int d\alpha \int d\beta \int \frac{d^2 q_\perp}{(2\pi)^3} \; \delta_{(+)}(q^2) \\ \times (2\pi) \delta_{(+)}((k_1 + k_2 - q)^2 - m_H^2) |\mathcal{M}|^2 \tag{4.109}$$

where the ξ_i denote the momentum fractions of the incoming gluons and we parametrise the final-state gluon momentum, q, in terms of Sudakov variables as in equation (4.59), with

$$\hat{s} = 2 k_1 \cdot k_2 \; . \tag{4.110}$$

The amplitude, $\mathcal{M}$, is summed over equal incoming helicities by contraction with a polarisation vector (in the k_1-k_2 centre-of-mass frame), $e^\mu = (0, \cos\phi, \sin\phi, 0)$

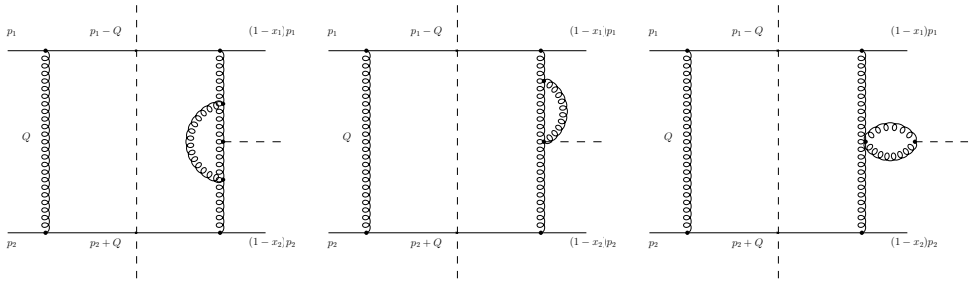

(a) (b) (c)

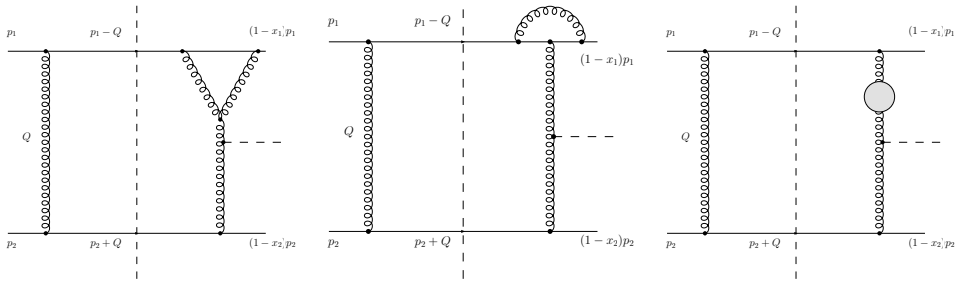

(d) (e) (f)

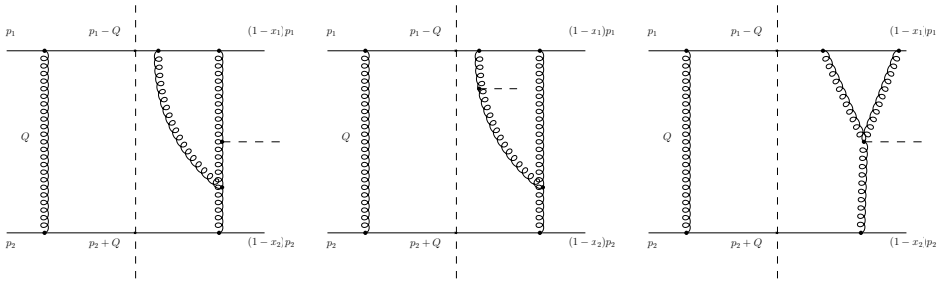

(g) (h) (i)

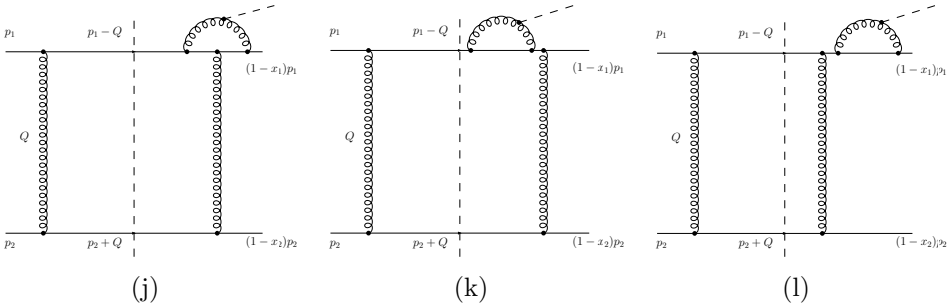

(j) (k) (l)

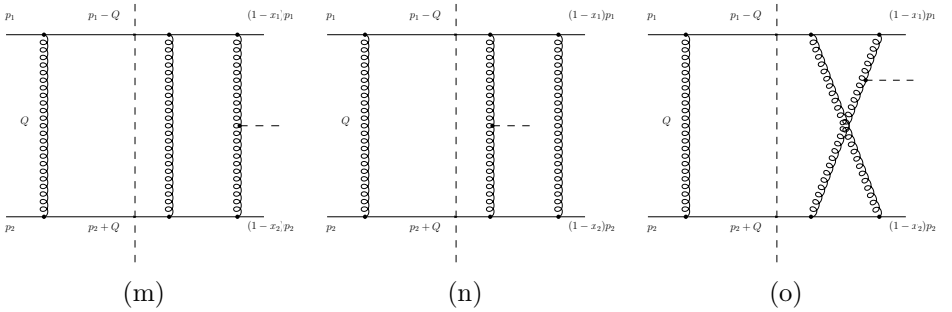

(m) (n) (o)

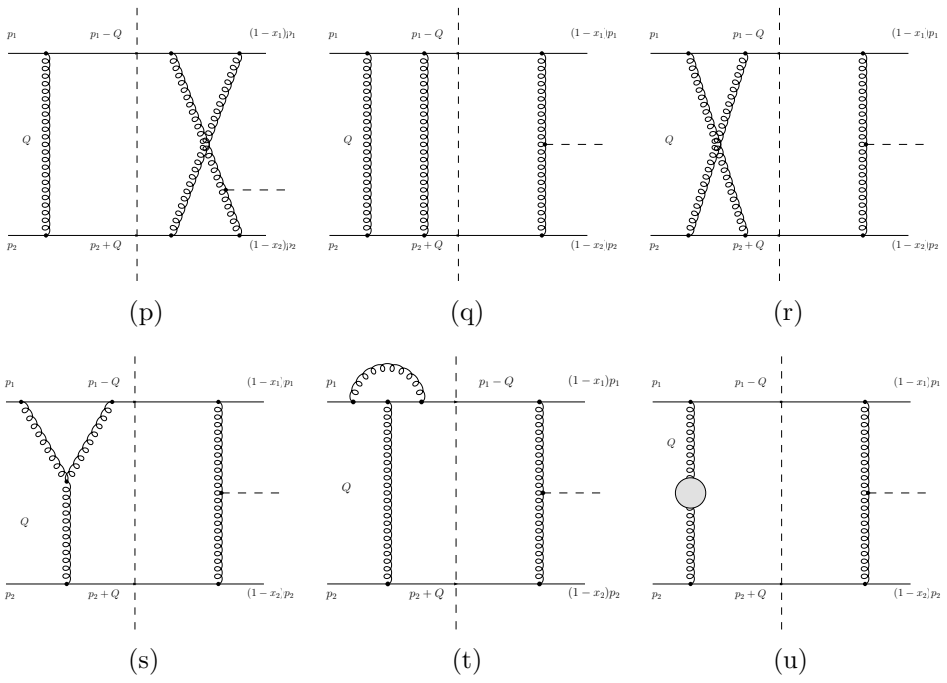

Figure 4.15: Virtual corrections contributing to the cut $qq' \to q \oplus H \oplus q'$ amplitude at next-to-leading order, in the high energy limit. Not shown are those diagrams obtained by exchanging x_1 and x_2 and those in which the Higgs is radiated on the left of the cut.

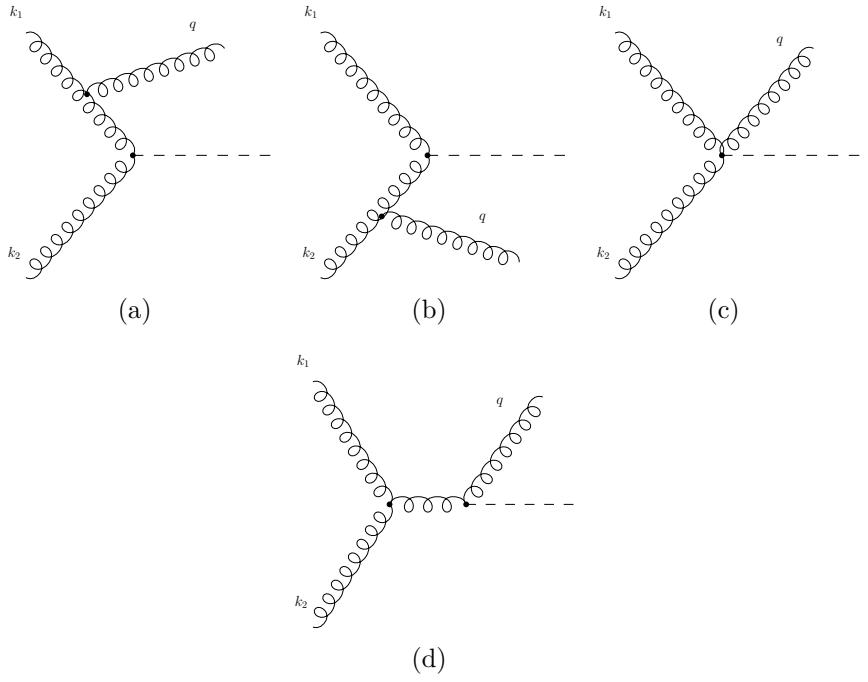

Figure 4.16: Diagrams contributing to the process $gg \to Hg$.

for the incoming gluons, followed by an average over ϕ i.e.

$$\mathcal{M} = \int_0^{2\pi} \frac{d\phi}{2\pi} e^\mu e^\nu \mathcal{M}_{\mu\nu} \, . \tag{4.111}$$

Next, we divide the phase-space of the emitted gluon into the regions $\alpha > \beta$ and $\alpha < \beta$, which is equivalent to dividing the phase-space about zero rapidity. We shall calculate only the contribution from the $\alpha > \beta$ region, however it will be clear that the $\alpha < \beta$ region gives an equal result. In addition, we sum over final state polarisations using[5]

$$\sum_\lambda \varepsilon_\lambda^\rho(k) \varepsilon_\lambda^{*\rho'}(k) = -g^{\rho\rho'} + \frac{k_1^\rho k^{\rho'} + k_1^{\rho'} k^\rho}{k_1 \cdot k} \, . \tag{4.112}$$

We also average over incoming gluon colours, though we stress that changing the treatment of colour in the process affects only the normalisation, since each diagram has identical colour structure. After a little algebra, which is performed using FORM, we find

$$\begin{aligned}
\sigma|_{\alpha>\beta} = \int d\xi_1 \int d\xi_2 \; & g(\xi_1;\mu_F^2) g(\xi_2;\mu_F^2) \frac{1}{2\hat{s}} \int \frac{d^2 q_\perp}{(2\pi)^2} \int_{\frac{q_\perp}{\sqrt{\hat{s}}}}^1 d\alpha \; |\mathcal{M}^{\rm LO}|^2 \; C_A \; g^2 \\
& \times \delta_{(+)}((k_1 + k_2 - q)^2 - m_H^2) \left\{ \frac{1}{q_\perp^2} \left[-4 + \frac{2}{\alpha} + 4\alpha - 2\alpha^2 + \frac{\alpha^3}{2} \right] \right. \\
& + \frac{2}{\hat{s}} \left[-3 + \frac{4}{\alpha} - \frac{2}{\alpha^2} + \alpha \right] + \frac{q_\perp^2}{\hat{s}^2} \left[\frac{3}{\alpha} - \frac{6}{\alpha^2} + \frac{4}{\alpha^3} \right] \\
& \left. + \frac{2q_\perp^4}{\hat{s}^3} \left[\frac{1}{\alpha^3} - \frac{1}{\alpha^4} \right] + \frac{q_\perp^6}{2\hat{s}^4} \frac{1}{\alpha^5} \right\}
\end{aligned} \tag{4.113}$$

where

$$\mathcal{M}^{\rm LO} = \int_0^{2\pi} \frac{d\phi}{2\pi} e^\mu e^\nu \mathcal{M}_{\mu\nu}^{\rm LO} \tag{4.114}$$

is the lowest order $gg \to H$ amplitude summed over equal incoming helicities. Only the term proportional to $1/q_\perp^2$ here can generate a logarithm. Keeping only

[5]It is interesting to note that, in processes involving two or more external gluons, the replacement of the gluon polarisation sum with $g^{\mu\nu}$ is not in general valid [75].

this term then, changing variables as $\alpha = 1 - z$, approximating the delta-function and including the region $\alpha < \beta$, we find

$$\sigma = \int d\xi_1 \int d\xi_2 \; g(\xi_1;\mu_F^2) g(\xi_2;\mu_F^2) \frac{1}{2\hat{s}} \int \frac{dq_\perp^2}{q_\perp^2} \int_0^{1-\frac{q_\perp}{m_H}} dz \\ \times (2\pi)\delta_{(+)}(z\hat{s} - m_H^2) |\mathcal{M}^{\mathrm{LO}}|^2 \frac{\alpha_s}{\pi} \left(z P_{gg}(z) + \frac{C_A}{2}(3z^3 - 5z^2 + 5z - 3)) \right) , \tag{4.115}$$

where we replaced $\sqrt{\hat{s}} \to m_H$ in the upper limit of the z integral, since in this region we may take $z \approx 1$ in the Higgs delta-function. The additional z-dependent piece, not proportional to $P_{gg}(z)$, arises due to the restricted sum over incoming helicities. If the sum is taken over all helicity configurations this term vanishes.

Following the Durham group, we set $z = 1$ in the Higgs delta-function and integrate over z, which is equivalent to an integration over the gluon's polar angle. This gives

$$\sigma \propto \int \frac{dq_\perp^2}{q_\perp^2} \frac{C_A \alpha_s}{\pi} \left(0.339 + \ln\left(\frac{m_H}{2q_\perp}\right) - \frac{11}{12} \right) \tag{4.116}$$

which should be compared with equation (4.17). It is not clear why the two results differ, however, we may comment on the validity of the procedure. The use of unitarity to infer virtual corrections from real corrections is only valid in the soft region (or for final-state collinear divergences). This is obvious from the form of equation (4.115), since the virtual corrections are proportional to the lowest order delta-function, $\delta(\hat{s} - m_H^2)$, whereas this is only true for the real emission result when $z \to 1$. Taking the soft limit in equation (4.115) then, we find

$$\sigma|_{\mathrm{soft}} \propto \int \frac{dq_\perp^2}{q_\perp^2} \frac{C_A \alpha_s}{\pi} \ln\left(\frac{m_H}{q_\perp}\right) = \int \frac{dq_\perp^2}{q_\perp^2} \frac{C_A \alpha_s}{\pi} \int_0^{1-\frac{q_\perp}{m_H}} \frac{dz}{1-z} \, . \tag{4.117}$$

Thus we see that the upper limit of the z integral, corresponding to soft emissions (where the unitarity argument may be applied), is in agreement with the results of equations (4.63) and (4.108) and not with the Durham result of equations (4.13)-(4.15). Put another way, the $gg \to gH$ cross-section receives no single logarithmic

contribution from wide-angle soft gluons, in contrast to the claims of the Durham group.

4.6 Phenomenological impact

Having shown in the previous sections that the Durham group's calculation of central exclusive production requires modification, we now assess the impact this has on predictions of the central exclusive cross-section. The difference between the Durham group's Sudakov factor and our result depends on the logarithm of the sub-process centre-of-mass energy and may be expressed as

$$\ln\left(\frac{T(\boldsymbol{Q}_\perp,\sqrt{\hat{s}})}{T(\boldsymbol{Q}_\perp,0.62\sqrt{\hat{s}})}\right)=\frac{C_A}{2\beta_0 a}\Big(a(L-L')+(1+aL')\ln(1+aL') \\ -(1+aL)\ln(1+aL)\Big)+\ln\left(\frac{1+aL}{1+aL'}\right) \quad (4.118)$$

where

$$L=\ln\left(\frac{\hat{s}}{\boldsymbol{Q}_\perp^2}\right) \qquad L'=\ln\left(\frac{0.62^2\hat{s}}{\boldsymbol{Q}_\perp^2}\right) \quad (4.119)$$

$$a=\frac{\alpha_s(\boldsymbol{Q}_\perp^2)\beta_0}{\pi} \quad (4.120)$$

and in evaluating (4.118) we used the one-loop form of the running coupling constant. The ratio of the two Sudakov factors is plotted in figure 4.17 for a range of sub-process centre-of-mass energies, while keeping $|\boldsymbol{Q}_\perp|$ fixed at 2 GeV. We see that the modified Sudakov factor is smaller than the Durham group's, with its relative size decreasing as we increase $\hat{s}$.

In order to gauge the effect of the modified Sudakov factor on cross-section predictions, we take as an example the cross-section for central exclusive Higgs production at the LHC, with 14 TeV centre-of-mass energy. We compute the cross-section, using the ExHuME Monte Carlo generator [76], placing no cuts on the final-state particles. The results are shown in figure 4.18, for two different

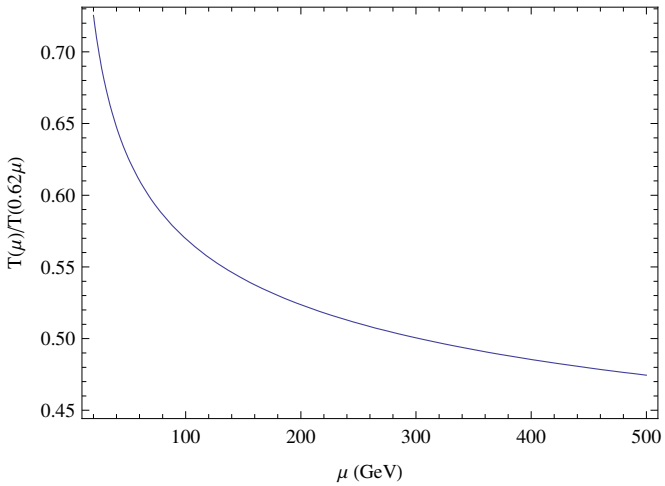

Figure 4.17: Ratio of the Sudakov factors $T(\boldsymbol{Q}_\perp, \mu)$ and $T(\boldsymbol{Q}_\perp, 0.62\mu)$ plotted against the sub-process centre-of-mass energy, μ. $|\boldsymbol{Q}_\perp|$ is held fixed at 2 GeV

parton distribution functions. As in figure 4.17 we see a suppression of the cross-section, relative to the Durham group's predictions, which increases with the Higgs mass.

We see from the figure that the effect of the modified Sudakov factor is to suppress the cross-section by approximately a factor of 2 in this mass range.

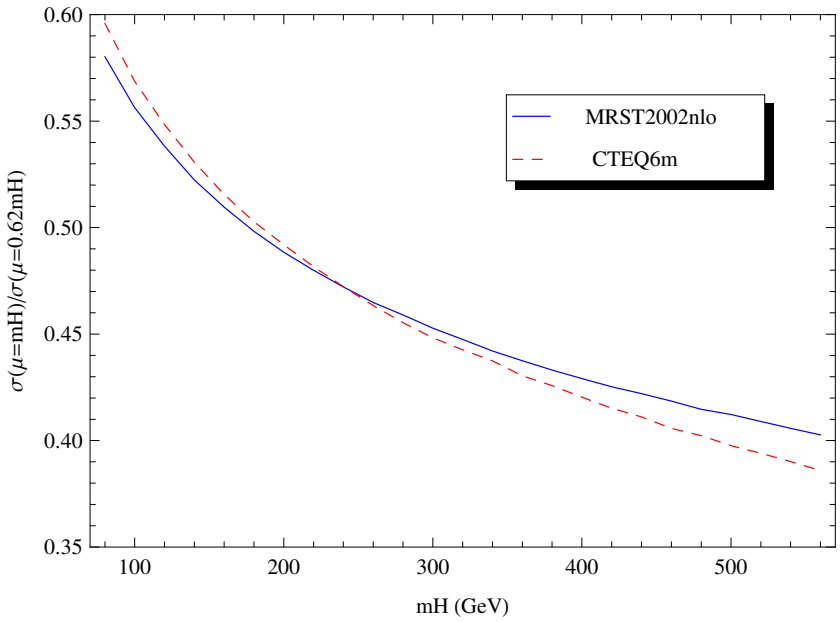

Figure 4.18: Ratio of the cross-section for central exclusive Higgs production at the LHC evaluated with the scale in the Sudakov factor set to $\mu = m_H$ divided by the cross-section with the scale set to $\mu = 0.62 m_H$, plotted as a function of the Higgs mass. The solid blue and dashed red lines were generated using MRST2002nlo [77] and CTEQ6m [78] parton distributions respectively.

Chapter 5

Central exclusive production of long-lived gluinos

5.1 Long lived gluinos

Supersymmetric extensions of the standard model predict a fermionic partner to the gluon, named the gluino (denoted $\tilde{g}$), which can be long-lived. In this chapter we consider the possibility of producing such particles via the central exclusive production mechanism. This chapter is based on the paper [79].

Among the possible extensions to the standard model supersymmetric theories are one of the most well studied. These theories contain at least one extra field partnered to each standard model field. The new fields have the opposite spin-statistics to the standard model fields they are partner to and the resulting Lagrangian is invariant under transformations that mix fermion and boson degrees-of-freedom. In such theories, the gluon is partnered with a particle known as the gluino, which is a spin-$\frac{1}{2}$ Majorana fermion transforming in the adjoint representation of the SU(3) colour group.

One recently proposed supersymmetric model is 'split supersymmetry' [80,81].

In this model the scalar partners of the quarks can acquire very large masses, while the supersymmetric fermions, including the gluino, can still have TeV scale masses. In this case the gluino may be long-lived on collider timescales since it decays through the scalar superpartners. A long-lived gluino has also previously been studied in the context of models in which it is the lightest supersymmetric particle [82–84].

A long-lived gluino can be produced in a bound-state, termed gluinonium [85–88], or can be produced unbound in which case it will hadronize into colour neutral states termed R-hadrons [82]. The gluino lifetime is approximately given by (neglecting electroweak corrections and possible decays to a Goldstino[1]) [89]

$$\tau_{\tilde{g}} = \frac{4 \text{ sec}}{N} \left(\frac{m_S}{10^9 \text{ GeV}} \right)^4 \left(\frac{1 \text{ TeV}}{m_{\tilde{g}}} \right)^5 , \tag{5.1}$$

where m_S is the supersymmetry breaking scale and N depends upon m_S and $m_{\tilde{g}}$ (and very weakly on the supersymmetry parameter $\tan\beta$), but is of order unity. Cosmological considerations of long-lived gluinos in the early universe [90] can place upper bounds on $\tau_{\tilde{g}}$, giving $\tau_{\tilde{g}} \lesssim 100$ s for $m_{\tilde{g}} \gtrsim 500$ GeV and $\tau_{\tilde{g}} \lesssim 10^6$ years for $m_{\tilde{g}} \lesssim 500$ GeV. Clearly these constraints do not rule out gluinos long-lived on collider timescales.

Data from the Tevatron have been used to place the limit $m_{\tilde{g}} \gtrsim 170$ GeV on the mass of a long-lived gluino [91], for the case in which the gluino forms only neutral hadrons which remain neutral as they pass through the detector. In addition, studies of long-lived gluinos which come to rest within the D0 detector at the Tevatron have been performed. For a gluino lifetime $\tau_{\tilde{g}} \lesssim 3$ hours the exclusion derived from such searches is approximately $m_{\tilde{g}} \lesssim 270$ GeV, given certain assumptions [92]. This bound however becomes weaker for longer gluino lifetimes.

[1]The inclusion of decays to a Goldstino can in some cases substantially decrease the gluino lifetime [89].

In the following sections we consider the central exclusive production of both gluinonium and R-hadrons at the LHC. We shall assume that additional proton detectors have been fitted at 420m and 220m from the interaction point and that the LHC is running at its design energy of 14 TeV. The rates of production are calculated using the ExHuME Monte Carlo generator [76], which implements the Durham model described in chapter 4.

5.2 Calculation of the production amplitude

We first describe the calculation of the sub-process amplitude for gluino production. There are two diagrams which contribute at lowest order, see figure 5.1. The invariant amplitude, summed over the colours of the gluinos, is

$$\mathcal{M}^{a_1 a_2}(\lambda_1,\lambda_2;\sigma_1,\sigma_2) = ig^2 \sum_{b_1,b_2,c} f^{a_1 b_1 c} f^{a_2 b_2 c}\, \overline{\Psi}^{(+)}_{p_1,\sigma_1} \left[\frac{\gamma^\mu (\not{p}_1 - \not{k}_1 + m_{\tilde{g}})\gamma^\nu}{2p_1\cdot k_1} + \frac{\gamma^\nu (\not{p}_1 - \not{k}_2 + m_{\tilde{g}})\gamma^\mu}{2p_1\cdot k_2} \right] \Psi^{(-)}_{p_2,\sigma_2}\, \varepsilon^{\lambda_1}_\mu(k_1)\varepsilon^{\lambda_2}_\nu(k_2)\ . \tag{5.2}$$

The Majorana Feynman rules are identical to those for Dirac fermions, with the exception that we must make an arbitrary choice for the fermion number flow arrows (see for example [93]). In addition, the cross-section must only be integrated over half of the final-state phase space in order to account for the identical nature of the gluinos. The full sub-process amplitude is

$$\bar{\mathcal{M}}(\sigma_1,\sigma_2) = \frac{1}{2}\frac{1}{N^2-1}\sum_{a_1,a_2}\delta_{a_1 a_2}\left(\mathcal{M}^{a_1 a_2}(+,+;\sigma_1,\sigma_2) + \mathcal{M}^{a_1 a_2}(-,-;\sigma_1,\sigma_2)\right)\ , \tag{5.3}$$

recalling again that we must sum the incoming gluon helicities at the amplitude level (see equation 4.9).

In order to calculate this amplitude we employ the WvdW technique described in section 3.1. We shall use the following shorthand for the components of the

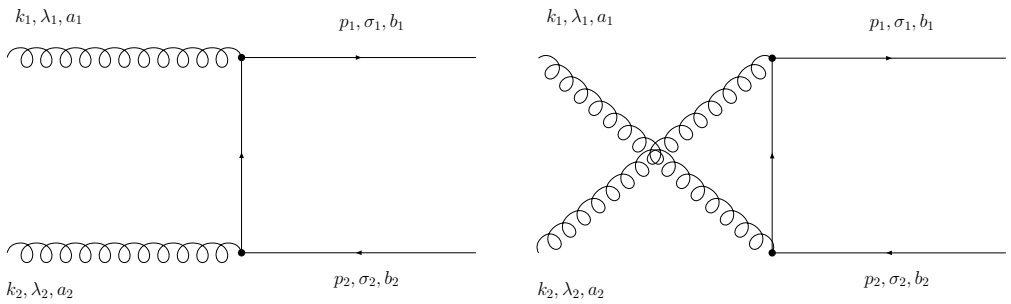

Figure 5.1: The two diagrams contributing to $gg \to \tilde{g}\tilde{g}$.

spinor wave-functions

$$\Psi^{(+)}_{p_1,\sigma_1} = \begin{pmatrix} \phi_{1,\alpha} \\ \psi_1^{\dot{\alpha}} \end{pmatrix} \qquad \Psi^{(-)}_{p_2,\sigma_2} = \begin{pmatrix} \phi_{2,\alpha} \\ \psi_2^{\dot{\alpha}} \end{pmatrix} \ . \tag{5.4}$$

In addition, we take for the gauge spinors associated with $\varepsilon^{\lambda_1}_{\mu}(k_1)$ and $\varepsilon^{\lambda_2}_{\nu}(k_2)$

$$g^{\pm}_{1,\alpha} = p_{1,\alpha\dot{\beta}} k_1^{\dot{\beta}} \ , \tag{5.5}$$

$$g^{\pm}_{2,\alpha} = p_{1,\alpha\dot{\beta}} k_2^{\dot{\beta}} \ . \tag{5.6}$$

After a little algebra, one obtains

$$\frac{1}{N^2-1} \sum_{a_1,a_2} \delta_{a_1 a_2} \mathcal{M}^{a_1 a_2}(+,+;\sigma_1,\sigma_2) = \frac{iC_A g^2 m_{\tilde{g}}}{2p_1\cdot k_1 p_1 \cdot k_2} \langle k_1 k_2\rangle^2 \langle \phi_1 \psi_2\rangle^* \ , \tag{5.7}$$

$$\frac{1}{N^2-1} \sum_{a_1,a_2} \delta_{a_1 a_2} \mathcal{M}^{a_1 a_2}(-,-;\sigma_1,\sigma_2) = \frac{iC_A g^2 m_{\tilde{g}}}{2p_1\cdot k_1 p_1 \cdot k_2} (\langle k_1 k_2\rangle^*)^2 \langle \phi_2 \psi_1\rangle \ . \tag{5.8}$$

The amplitude for a general gluino helicity configuration to be produced can now be calculated using (5.3). To do this we first specialise to the centre of mass frame, taking the gluons to be moving along the z-axis. Thus, their four-vectors are

$$k_1^{\mu} = \left(k^0, \mathbf{0}, +|\boldsymbol{k}|\right) \ , \qquad k_2^{\mu} = \left(k^0, \mathbf{0}, -|\boldsymbol{k}|\right) \ , \tag{5.9}$$

and the gluino four-momenta in this frame are

$$p_1^{\mu} = \left(k^0, +\boldsymbol{p}\right) \ , \qquad p_2^{\mu} = \left(k^0, -\boldsymbol{p}\right) \ , \tag{5.10}$$

with their polar and azimuthal angles related by

$$\theta_{p_2} = \pi - \theta \ , \qquad \theta \equiv \theta_{p_1} \ , \tag{5.11}$$

$$\phi_{p_2} = \phi + \pi \ , \qquad \phi \equiv \phi_{p_1} \ . \tag{5.12}$$

The Weyl spinors $k_{1,\alpha}$ and $k_{2,\alpha}$ then become

$$k_{1,\alpha} = \sqrt{2k^0} \begin{pmatrix} 1 \\ 0 \end{pmatrix} \qquad k_{2,\alpha} = \sqrt{2k^0} \begin{pmatrix} 0 \\ 1 \end{pmatrix} \ . \tag{5.13}$$

There is a small subtlety here connected with the fact that we are summing over incoming gluon helicities at the amplitude level. The representations of the gluon polarisation vectors, (3.30), are not invariant under phase shifts of the $k_{i,\alpha}$. In particular, the positive and negative representations transform differently. This would lead to a non-physical dependence on the azimuthal angle of k_1, ϕ_{k_1} in our amplitude. To rectify this problem, we must ensure that the $k_{i,\alpha}$ are real, which is achieved by setting $\phi_{k_1} = 0$ ($\phi_{k_1} = \pm\pi$ would also have been acceptable.). With this choice we obtain

$$\langle k_1 k_2 \rangle = 2k^0 \ . \tag{5.14}$$

With the system set up as described we may now calculate $\bar{\mathcal{M}}(\sigma_1, \sigma_2)$ for each gluino helicity configuration. The amplitudes are

$$\bar{\mathcal{M}}(1,2) = \bar{\mathcal{M}}(2,1) = \frac{iC_A g^2 m_{\tilde{g}}}{2p_1 \cdot k_1 p_1 \cdot k_2} (2k^0)^2 |\boldsymbol{p}| \tag{5.15}$$

$$\bar{\mathcal{M}}(1,1) = \bar{\mathcal{M}}(2,2) = 0 \ . \tag{5.16}$$

Summing over the gluino helicities and substituting into equation (4.8) one arrives at the differential cross-section:

$$\left(\frac{d\hat{\sigma}}{d\Omega} \right)_{\mathrm{CM}} = \frac{9}{32} \frac{\alpha_s^2 m_{\tilde{g}}^2 \beta_{\tilde{g}}^3}{(m_{\tilde{g}}^2 + |\boldsymbol{p}|^2 \sin^2\theta)^2} \ , \tag{5.17}$$

where $\beta_{\tilde{g}}$ is the modulus of the velocity of either gluino in the centre-of-mass frame.

5.3 Open production - R-hadrons

5.3.1 Production and spectrum

Using the differential cross-section derived in the previous section we now consider the open production of gluino pairs. Following [46, 84, 94] we modify the open production cross-section, equation (5.17), to include a threshold enhancement factor, K:

$$\left(\frac{d\hat{\sigma}}{d\Omega}\right)_{\mathrm{CM}} = \frac{9}{32}\frac{\alpha_s^2(\mu)m_{\tilde{g}}^2\beta_{\tilde{g}}^3}{(m_{\tilde{g}}^2 + |\boldsymbol{p}|^2\sin^2\theta)^2}K \ , \tag{5.18}$$

where

$$K = \frac{Z_g}{1-\exp(-Z_g)}\left(1+\frac{Z_g^2}{4\pi^2}\right) \tag{5.19}$$

and

$$Z_g = \frac{3\pi\alpha_s(\beta_{\tilde{g}}m_{\tilde{g}})}{\beta_{\tilde{g}}}. \tag{5.20}$$

This factor arises from a resummation of diagrams which are enhanced at low β. We also evaluate $\alpha_s(\mu)$ at $\mu = \frac{1}{5}m_{\tilde{g}}$ which is justified by the next to leading order calculations of [95].

The gluino is colour octet and in the case where it is long-lived will hadronize into bound states termed R-hadrons. These are colour neutral states of a single gluino bound with gluons and/or quarks and anti-quarks. There have been several studies of the spectrum of these states and their interactions in the detector [82–84,91,96–104]. It is found that the states are nearly mass degenerate, with the R-mesons ($\tilde{g}\bar{q}q$) being slightly lighter than the lowest gluino-gluon state, R_g^0, [96–98, 101] and the R-baryons ($\tilde{g}qqq$) being about 0.3 GeV heavier than these [97, 101]. Only a small proportion of gluinos are expected to form R-baryons and roughly half of the R-mesons formed will be charged, with the rest neutral. The fraction forming R_g states is unknown and is therefore a free parameter.

5.3.2 Interaction in detectors and triggering

As a R-hadron passes through the detector, it will lose energy through ionisation (if it is charged) and via hadronic interactions in the calorimeters. It is even possible for the R-hadron to become stopped in the detector [104], however we do not consider that possibility here. R-mesons may be converted into R-baryons by scattering off nucleons in the calorimeter, but R-baryon conversion to R-mesons is likely to be negligible [101]. Also, the R_g states are expected to interact in the same way as a neutral R-meson, hence by the time the R-hadron has passed through the calorimeter it may well be an R-baryon, irrespective of how it started. Thus, 75% of all R-hadrons are expected to be charged after passing through the calorimeters (the ratio of charged to neutral R-baryon states is 3:1) [103]. These events will look like a muon within a jet (though more isolated than one resulting from a heavy quark weak decay [103]) but with the particle arriving significantly later at the muon chambers.

The difficulties in triggering on events involving R-hadrons, at the experiment ATLAS, have been discussed in [103]. Essentially, the level 1 triggers based on the energy deposited in the calorimeters (including the missing energy triggers) are useless because the R-hadrons usually leave too little energy in the detector to pass the triggers. The only other option is to use the muon triggers. This presents its own problems however, since the R-hadrons can be so delayed that they do not even arrive at the muon chambers within the same bunch crossing. We therefore impose the following cuts:

- The pseudo-rapidity of each R-hadron should satisfy $|\eta| < 2.4$. This is the limit of the muon trigger at ATLAS.

- Make a cut on the speed of the fastest of the two R-hadrons of $0.6 < \beta < 0.9$. This is the R-hadron which triggers the muon chambers. The upper bound

is chosen in order to eliminate all muon backgrounds whilst the lower bound arises in order that the R-hadron arrives in time to trigger the event.

- For the slower R-hadron we make a cut of $0.25 < \beta < 0.9$ where the lower bound is determined by the requirement that the R-hadron is in the same event record as the faster R-hadron.

When quoting expected numbers of events we must also remember to multiply by a factor 0.75^2 which accounts for the fact that both of the R-hadrons must be charged. The efficiency of the muon trigger and the acceptance of the forward detectors must also be taken into account. For a discussion of these points see [79].

The backgrounds to our signal are any processes which produce a muon or fake a muon. These backgrounds are found to be negligible after the cuts discussed above [79].

5.3.3 Results

Figure 5.2 shows the cross-section, generated using ExHuME, after the cuts described in the previous section, but without the trigger efficiency and detector acceptance factors. We plot results using two different parton distribution function sets and also show the effect of demanding that both R-hadrons pass the level one trigger (i.e. both have $\beta > 0.6$). In figure 5.3 we show the effect of the threshold factor given in equation (5.19). The rate is not large, however the smallness of the backgrounds means we do not need many events to obtain a significant result. As shown in table 5.1, we expect to be able to collect at least 3 events over 3 years high luminosity running, for gluino masses up to 350 GeV. Of course, if long-lived gluinos exist in this mass range, they will be discovered first in inclusive production processes. The advantage of a measurement in the CEP channel is that we may reconstruct the gluino mass using only the measured forward proton momenta and the lab-frame scattering angles of the two gluinos.

As shown in the table, this is enough to measure the mass of the gluino to an accuracy of better than 1%. In contrast, measurements of the gluino mass in inclusive production require an understanding of the energy deposited by a R-hadron as it traverses the detector, leading to large systematic uncertainties in this mass region [102].

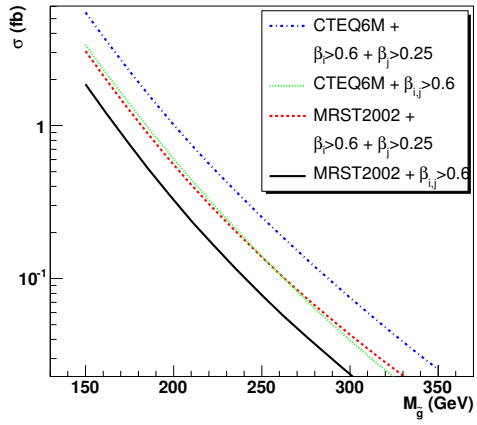

Figure 5.2: The cross-section for exclusive gluino pair production for the MRST2002nlo and CTEQ6m PDF sets with 2 different choices of β cut. β_i represents the highest velocity R-hadron.

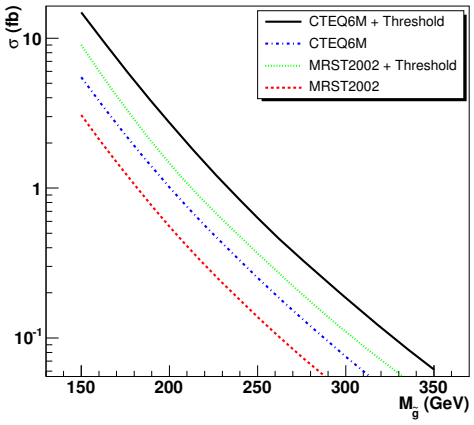

Figure 5.3: The cross-section for exclusive gluino pair production for the MRST2002nlo and CTEQ6m PDF sets with and without the threshold enhancement factor.

$m_{\tilde{g}}$ (GeV)	$\sigma_{m_{\tilde{g}}}$ (GeV)	$\frac{\sigma_{m_{\tilde{g}}}}{\sqrt{N-1}}$ (GeV)	N
200	2.31	0.19	145
250	2.97	0.50	35.0
300	3.50	1.10	10.2
320	3.61	1.54	6.5
350	3.87	2.45	3.5

Table 5.1: Gluino mass resolution, $\sigma_{m_{\tilde{g}}}$ and expected number of events, N, for 300 fb^{-1} of data at the LHC.

5.4 Gluinonium

5.4.1 Cross-section calculation

We now consider the production of gluino pairs in the form of a bound-state termed gluinonium. The gluinos are produced in a colour singlet configuration. Due to the Majorana nature of the gluinos the sum of the spin and angular momentum quantum numbers, $S+L$, of any colour singlet two gluino bound state must be an even number [88]. Applying parity conservation then determines that ${}^3P_0$ is the lowest accessible state.

After production the gluinonium state will decay very rapidly to two gluons, which are then detected as a pair of jets.

Non-relativistically the colour singlet potential between the two gluinos (due to single gluon exchange) is given by

$$V(r) = -\frac{3\alpha_s}{r} , \tag{5.21}$$

where r is the separation of the gluinos.

The state $|{}^3P_0\rangle = |J=0, L=1, S=1\rangle$ may be decomposed in terms of the states $|L, m_L; S, m_S\rangle^z \equiv |L, m_L\rangle^z \otimes |S, m_S\rangle^z$ as

$$|J=0, L=1, S=1\rangle = \frac{1}{\sqrt{3}} \left(|1,1;1,-1\rangle^z - |1,0;1,0\rangle^z + |1,-1;1,1\rangle^z \right) , \tag{5.22}$$

where the z indicates that the spin is quantised along the z-axis. The states $|L, m_L; S, m_S\rangle^z$ can in turn be written as an anti-symmetrised superposition of free particle states, weighted by the Fourier transform of a Schrödinger-like wave function, $\tilde{\psi}_{Lm_L}(\boldsymbol{p})$, appropriate to (5.21) (see for example [105]), i.e.

$$\tilde{\psi}_{Lm_L}(\boldsymbol{p}) = \int d^3\boldsymbol{x} \mathrm{e}^{i\boldsymbol{p}\cdot\boldsymbol{x}} \psi_{Lm_L}(\boldsymbol{x}) \tag{5.23}$$

where

$$\psi_{1,0}(\boldsymbol{x}) = Nr\mathrm{e}^{-r/(2a_0)}\cos\theta \quad \text{and}$$
$$\psi_{1,\pm1}(\boldsymbol{x}) = \mp\frac{N}{\sqrt{2}}r\mathrm{e}^{-r/(2a_0)}\sin\theta\ \mathrm{e}^{\pm i\phi} \tag{5.24}$$

with

$$N = \frac{1}{a_0}\frac{1}{\sqrt{32\pi a_0^3}}$$
$$a_0 = \frac{2}{3}\frac{1}{m_{\tilde{g}}\alpha_s}. \tag{5.25}$$

We choose the scale in $\alpha_s(Q)$ to be determined by the mean size of the gluinonium state, i.e.

$$Q = \frac{1}{\langle r\rangle} = \frac{1}{10a_0}. \tag{5.26}$$

This scale is substantially smaller than the value chosen in [46], but ought to be more appropriate, since the bound state is P-wave rather than S-wave. In any case, we show our final results for both choices of scale.

Taking matrix elements of these states with the initial state of two gluons gives, in the centre-of-mass frame

$$^z\langle L, m_L; S, m_S|gg\rangle = \frac{1}{2}\left(\frac{2M_{\tilde{G}}}{2m_{\tilde{g}}2m_{\tilde{g}}}\right)^{1/2}\int\frac{d^3p}{(2\pi)^3}\times$$
$$\frac{1}{\sqrt{2}}\left(\tilde{\psi}^*_{Lm_L}(\boldsymbol{p}) - \tilde{\psi}^*_{Lm_L}(-\boldsymbol{p})\right)\ ^z\langle \boldsymbol{p}, S, m_S|gg\rangle\ , \tag{5.27}$$

where $\boldsymbol{p}$ is the momentum of one of the gluinos, $|\boldsymbol{p}, S, m_S\rangle^z$ is the free particle state of two gluinos with total spin S and spin projection along the z-axis m_S and

$$\int\frac{d^3p}{(2\pi)^3}\left|\tilde{\psi}_{Lm_L}(\boldsymbol{p})\right|^2 = 1\ . \tag{5.28}$$

Taking the matrix element of (5.22) and substituting (5.27) one obtains

$$A\left(gg\to{}^3P_0\right) = \frac{1}{2}\frac{1}{\sqrt{3}}\left(\frac{2M_{\tilde{G}}}{2m_{\tilde{g}}2m_{\tilde{g}}}\right)^{1/2}\int\frac{d^3p}{(2\pi)^3}\Big(\tilde{\psi}^*_{11}(\boldsymbol{p})\ ^z\langle\boldsymbol{p},1,-1|gg\rangle$$
$$-\tilde{\psi}^*_{10}(\boldsymbol{p})\ ^z\langle\boldsymbol{p},1,0|gg\rangle \tag{5.29}$$
$$+\tilde{\psi}^*_{1-1}(\boldsymbol{p})\ ^z\langle\boldsymbol{p},1,1|gg\rangle\Big)\ ,$$

where,

$$A\left(gg \to {}^3P_0\right) = \langle {}^3P_0|gg\rangle \ . \tag{5.30}$$

The factor involving the bound state mass, $M_{\tilde{G}}$ ($\approx 2m_{\tilde{g}}$), has been introduced to normalise the states correctly and the factor of $1/2$ is to avoid double counting since the gluinos are identical particles.

The cross-section for the production of the ${}^3P_0$ state is then given by

$$\hat{\sigma}\left(gg \to {}^3P_0\right) = \frac{1}{2\hat{s}} \int d\Pi_1 \left|A\left(gg \to {}^3P_0\right)\right|^2 , \tag{5.31}$$

where $d\Pi_1$ is an element of relativistically invariant one-body phase space.

As described in section 5.2, the amplitudes are calculated in terms of helicity states. Hence we now rewrite the matrix elements ${}^z\langle \boldsymbol{p}, S, m_S|gg\rangle$ in terms of matrix elements with the spin quantized along the momentum axis of one of the particles ${}^p\langle \boldsymbol{p}, S, m_S|gg\rangle$

$$\begin{aligned}
{}^z\langle \boldsymbol{p}, 1, 1|gg\rangle &= -{}^p\langle \boldsymbol{p}, 1, 0|gg\rangle \frac{1}{\sqrt{2}} \sin\theta e^{-i\phi} \\
{}^z\langle \boldsymbol{p}, 1, 0|gg\rangle &= {}^p\langle \boldsymbol{p}, 1, 0|gg\rangle \cos\theta \\
{}^z\langle \boldsymbol{p}, 1, -1|gg\rangle &= {}^p\langle \boldsymbol{p}, 1, 0|gg\rangle \frac{1}{\sqrt{2}} \sin\theta e^{i\phi} \ ,
\end{aligned} \tag{5.32}$$

where $\boldsymbol{p} = (|\boldsymbol{p}|\sin\theta\cos\phi, |\boldsymbol{p}|\sin\theta\sin\phi, |\boldsymbol{p}|\cos\theta)$ and we have used the fact that ${}^p\langle \boldsymbol{p}, 1, \pm 1|gg\rangle = 0$ (equation (5.16)).

Using equation (5.15), ${}^p\langle \boldsymbol{p}, 1, 0|gg\rangle$ is given by

$${}^p\langle \boldsymbol{p}, 1, 0|gg\rangle \approx 6\sqrt{2}i\pi\alpha_s(m_{\tilde{g}})\frac{|\boldsymbol{p}|}{m_{\tilde{g}}} \ , \tag{5.33}$$

where we have taken the non-relativistic limit, keeping only single powers of $\boldsymbol{p}$. Substituting (5.33) and (5.32) in equation (5.29) and using the identity

$$\int \frac{d^3p}{(2\pi)^3} \tilde{\psi}^*(\boldsymbol{p}) p_i = -i\frac{\partial\psi^*(0)}{\partial x_i} \ , \tag{5.34}$$

one obtains

$$A\left(gg \to {}^3P_0\right) = \sqrt{6}\pi \frac{\alpha_s(m_{\tilde{g}})}{m_{\tilde{g}}^{3/2}} \left(\frac{\partial \psi_{11}^*(0)}{\partial x_1} + i\frac{\partial \psi_{11}^*(0)}{\partial x_2} - \sqrt{2}\frac{\partial \psi_{10}^*(0)}{\partial x_3} - \frac{\partial \psi_{1-1}^*(0)}{\partial x_1} + i\frac{\partial \psi_{1-1}^*(0)}{\partial x_2} \right). \tag{5.35}$$

This gives

$$|A\left(gg \to {}^3P_0\right)|^2 = 51.26\pi\alpha_s^2(m_{\tilde{g}})\alpha_s^5(Q)\, m_{\tilde{g}}^2\,. \tag{5.36}$$

Substituting in (5.31) one obtains

$$\hat{\sigma} = 12.82\pi^2\alpha_s^2(m_{\tilde{g}})\alpha_s^5(Q)\,\delta(\hat{s} - 2m_{\tilde{g}}). \tag{5.37}$$

5.4.2 Results

After calculating the full cross-section, by running ExHuME with (5.37), the bound state is decayed, isotropically in its rest frame, to two gluons. These are then hadronized using PYTHIA [106], with a cut on the jet's transverse momentum of $p_\perp > 150$ GeV in order to model the level 1 trigger acceptance at ATLAS. Figure 5.4 shows the total cross-section with this cut as a function of gluino mass for both choices of scale and using two different parton distribution functions.

Unfortunately the rate is too small, corresponding to less than ~ 5 events per year at low luminosity (10 fb^{-1} per year) for a bound-state mass of 340 GeV, which is the current experimental lower bound. This rises to ~ 45 events at high luminosity (100 fb^{-1} per year), but this is before cuts to remove the backgrounds coming from inclusive central production ($pp \to p+jj+X+p$) and exclusive dijet production ($pp \to p+jj+p$). We model these backgrounds using POMWIG [107] and ExHuME respectively and confirm that they are prohibitive.

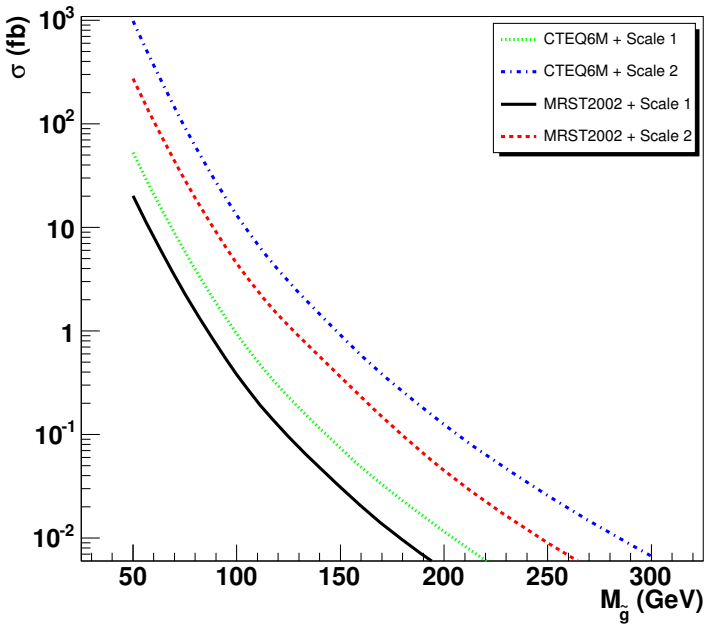

Figure 5.4: The total cross section for gluinonium production. Shown are results for the MRST2002nlo [77] and CTEQ6m [78] PDF sets with 2 different choices of scale. Scale 1 is the choice $Q^{-1} = a_0$ and Scale 2 is the choice $Q^{-1} = 10a_0$.

Chapter 6

Conclusions

In this thesis we have studied the central exclusive production process. In particular, we studied the amplitude for Higgs production, using perturbation theory, in three approaches. In one, we considered the amplitude at all-orders in the strong coupling constant, requiring a large logarithm at each order. This approach allowed us to write the amplitude in terms of parton distributions, a Sudakov form factor and derivatives of these functions. The second approach consisted of expanding out the amplitude to next-to-leading order in the strong coupling constant. We then evaluated the sub-set of the corrections at this order that are relevant to the Sudakov factor. Thirdly, we repeated the calculation of soft gluon bremsstrahlung in the $gg \to H$ process, used by the Durham group to constrain the form of the Sudakov factor (by exploiting unitarity).

Our findings were, that the calculation of this process by the Durham group, while correct in general form, requires modification. Specifically, we found that the cutoff on soft gluon radiation in the Durham Sudakov factor is incorrect. After modifying the Durham group's result, to incorporate our findings, we used central exclusive Higgs production at the LHC to assess the impact on cross-section predictions. Having computed the cross-section using the Monte Carlo generator ExHuME, we found that the modified Sudakov factor suppresses the

central exclusive production cross-section at the LHC by approximately a factor of 2 relative to the Durham group's predictions, for central system masses in the range 80-560 GeV. As a point of further study, it would be interesting to assess the impact on predictions for the central exclusive production of dijets at the Tevatron, for which data exist. We do not expect to find a disagreement with the data however. Not only will the effect be smaller for the lower central system masses probed in this observable, but the theoretical uncertainty on other parts of the calculation, for example the gap survival factor and unintegrated pdfs, is expected to be of a similar size to this effect (see for example [108]).

We also note that the fixed-order corrections we have computed form a subset of the full next-to-leading order corrections to central exclusive Higgs production, offering the possibility of extending the theoretical description of the process to this order.

In addition to investigating the theoretical underpinnings of central exclusive production cross-section calculations, we have also studied the production of long-lived gluino pairs at the LHC, via this mechanism. Both bound-state and open production were studied. It was found however that only the open production channel would be observable, due to large backgrounds in the bound-state production case. In the open production channel we showed that one could expect to collect at least 3 events for 300 fb^{-1} of data , with negligible background, for gluino masses $m_{\tilde{g}} \lesssim 350$ GeV. These events would allow for an extraction of the gluino mass to an accuracy of better than 1%. This would be highly complementary to any measurement in inclusive production, which suffers from large systematic uncertainties in this region.

Appendix A

Scalar integrals

In this appendix we collect the analytic expressions for the scalar integrals used in the integral recursion described in chapter 3 (see for example [32]). In addition to the definitions of equations (3.41) we also define:

$$n = \frac{d}{2} - \sigma \tag{A.1}$$

and

$$c_\Gamma = \frac{\Gamma^2(1-\epsilon)\Gamma(1+\epsilon)}{\Gamma(1-2\epsilon)} = \frac{1}{\Gamma(1-\epsilon)} + \mathcal{O}(\epsilon^3) \; . \tag{A.2}$$

1. Self energy diagrams: $I(d; \{\nu_1, \nu_2\}|p_1^2)$

See for example [109]:

$$I(d; \{\nu_1, \nu_2\}|p_1^2) = (-1)^\sigma (-p_1^2)^n \frac{\Gamma(\nu_1+n)\Gamma(\nu_2+n)\Gamma(-n)}{\Gamma(\nu_1)\Gamma(\nu_2)\Gamma(\sigma+2n)} \; . \tag{A.3}$$

2. Triangle diagrams: $I(d; \{\nu_1, \nu_2, \nu_3\}|p_1^2, p_2^2, p_3^2)$

(a) *One off-shell leg* [110]

$$I(d; \{\nu_1, \nu_2, \nu_3\}|0, 0, p_3^2) = (-1)^\sigma (-p_3^2)^n \frac{\Gamma(\nu_2+n)\Gamma(\nu_3+n)\Gamma(-n)}{\Gamma(\nu_2)\Gamma(\nu_3)\Gamma(\sigma+2n)} \; . \tag{A.4}$$

(b) *Two off-shell legs* [32]

$$I(d=4-2\epsilon;\{1,1,1\}|p_1^2,p_2^2,0)=\frac{c_\Gamma}{\epsilon^2}\frac{1}{p_1^2-p_2^2}\Big((-p_1^2)^{-\epsilon}-(-p_2^2)^{-\epsilon}\Big)\ . \quad \text{(A.5)}$$

(c) *Three off-shell legs* [111, 112]

$$I(d=4-2\epsilon;\{1,1,1\}|p_1^2,p_2^2,p_3^2)=\frac{i\pi^2}{\sqrt{\lambda}p_3^2}\Bigg(2\mathrm{Li}_2(-\rho x)+2\mathrm{Li}_2(-\rho y)$$
$$+(\ln(-\rho x)+i\pi)(\ln(-\rho y)+i\pi)+\ln\left(\frac{y}{x}\right)\ln\left(\frac{1+\rho y}{1+\rho x}\right)+\frac{\pi^2}{3}\Bigg)$$
$$x,y<0\ ;\quad p_3^2>0\ . \quad \text{(A.6)}$$

where $x=p_1^2/p_3^2$, $y=p_2^2/p_3^2$ and

$$\lambda=(1-x-y)^2-4xy\ ,\qquad \rho=\frac{2}{1-x-y+\sqrt{\lambda}}\ . \quad \text{(A.7)}$$

See [113] for the analytic continuation to other regions.

3. Box diagrams: $I(d=4-2\epsilon;\{1,1,1,1\}|(p_1+p_2)^2,(p_2+p_3)^2,p_1^2,p_2^2,p_3^2,p_4^2)$

(a) *Four on-shell legs* [32]

$$I(d=4-2\epsilon;\{1,1,1,1\}|s_{12},s_{23},0,0,0,0)=\frac{c_\Gamma}{s_{12}s_{23}}$$
$$\times\left[\frac{2}{\epsilon^2}\Big((-s_{12})^{-\epsilon}+(-s_{23})^{-\epsilon}\Big)-\ln^2\left(\frac{-s_{12}}{-s_{23}}\right)-\pi^2\right]\ . \quad \text{(A.8)}$$

(b) *One off-shell leg* [32]

$$I(d=4-2\epsilon;\{1,1,1,1\}|s_{12},s_{23},0,0,0,p_4^2)=\frac{c_\Gamma}{s_{12}s_{23}}$$
$$\times\left[\frac{2}{\epsilon^2}\Big((-s_{12})^{-\epsilon}+(-s_{23})^{-\epsilon}-(-p_4^2)^{-\epsilon}\Big)-2\mathrm{Li}\left(1-\frac{p_4^2}{s_{12}}\right)\right.$$
$$\left.-2\mathrm{Li}\left(1-\frac{p_4^2}{s_{23}}\right)-\ln^2\left(\frac{-s_{12}}{-s_{23}}\right)-\frac{\pi^2}{3}\right]\ . \quad \text{(A.9)}$$

(c) *Two adjacent off-shell legs* [32]

$$I(d=4-2\epsilon;\{1,1,1,1\}|s_{12},s_{23},0,0,p_3^2,p_4^2)=\frac{c_\Gamma}{s_{12}s_{23}}$$
$$\times\left[\frac{2}{\epsilon^2}\Big((-s_{12})^{-\epsilon}+(-s_{23})^{-\epsilon}-(-p_3^2)^{-\epsilon}-(-p_4^2)^{-\epsilon}\Big)+\frac{1}{\epsilon^2}\frac{(-p_3^2)^{-\epsilon}(-p_4^2)^{-\epsilon}}{(-s_{12})^{-\epsilon}}\right.$$
$$\left.-2\mathrm{Li}\left(1-\frac{p_3^2}{s_{23}}\right)-2\mathrm{Li}\left(1-\frac{p_4^2}{s_{23}}\right)-\ln^2\left(\frac{-s_{12}}{-s_{23}}\right)\right]\ . \qquad (A.10)$$

(d) *Two opposite off-shell legs* [32]

$$I(d=4-2\epsilon;\{1,1,1,1\}|s_{12},s_{23},0,p_2^2,0,p_4^2)=\frac{c_\Gamma}{(s_{12}s_{23}-p_4^2p_2^2)}$$
$$\times\left[\frac{2}{\epsilon^2}\Big((-s_{12})^{-\epsilon}+(-s_{23})^{-\epsilon}-(-p_2^2)^{-\epsilon}-(-p_4^2)^{-\epsilon}\Big)-2\mathrm{Li}\left(1-\frac{p_2^2}{s_{12}}\right)\right.$$
$$-2\mathrm{Li}\left(1-\frac{p_2^2}{s_{23}}\right)-2\mathrm{Li}\left(1-\frac{p_4^2}{s_{12}}\right)-2\mathrm{Li}\left(1-\frac{p_4^2}{s_{23}}\right)$$
$$\left.+2\mathrm{Li}\left(1-\frac{p_2^2p_4^2}{s_{12}s_{23}}\right)-\ln^2\left(\frac{-s_{12}}{-s_{23}}\right)\right]\ . \qquad (A.11)$$

(e) *Three off-shell legs* [35]

$$I(d=4-2\epsilon;\{1,1,1,1\}|s_{12},s_{23},0,p_2^2,p_3^2,p_4^2)=\frac{c_\Gamma}{(s_{12}s_{23}-p_4^2p_2^2)}$$
$$\times\left[\frac{2}{\epsilon^2}\Big((-s_{12})^{-\epsilon}+(-s_{23})^{-\epsilon}-(-p_2^2)^{-\epsilon}-(-p_3^2)^{-\epsilon}-(-p_4^2)^{-\epsilon}\Big)\right.$$
$$+\frac{1}{\epsilon^2}\frac{(-p_2^2)^{-\epsilon}(-p_3^2)^{-\epsilon}}{(-s_{23})^{-\epsilon}}+\frac{1}{\epsilon^2}\frac{(-p_3^2)^{-\epsilon}(-p_4^2)^{-\epsilon}}{(-s_{12})^{-\epsilon}}-2\mathrm{Li}\left(1-\frac{p_2^2}{s_{12}}\right)$$
$$\left.-2\mathrm{Li}\left(1-\frac{p_4^2}{s_{23}}\right)+2\mathrm{Li}\left(1-\frac{p_2^2p_4^2}{s_{12}s_{23}}\right)-\ln^2\left(\frac{-s_{12}}{-s_{23}}\right)\right]\ . \qquad (A.12)$$

(f) *Four off-shell legs* [112]

$$I(d=4-2\epsilon;\{1,1,1,1\}|s_{12},s_{23},p_1^2,p_2^2,p_3^2,p_4^2)=$$
$$I(d=4-2\epsilon;\{1,1,1\}|s_{12}s_{23},p_1^2p_3^2,p_2^2p_4^2)\ , \qquad (A.13)$$

for all momenta space like. See [114] for the continuation to other regions.

4. Pentagon diagrams: $I(d = 6 - 2\epsilon; \{1, 1, 1, 1, 1\})$

The pentagon integral in $d = 6 - 2\epsilon$ dimensions, with unit propagators, is finite. As shown in chapter 3, this integral always appears multiplied by a factor of ϵ and so we do not require it's explicit expression [34, 35].

Appendix B

Large top mass effective theory

In this appendix we describe the effective theory, formed by taking the top quark mass to infinity [61–63] and used in chapter 4 to compute the next-to-leading order corrections to central exclusive Higgs production. This approach has been found to give good agreement with the full theory, provided that the Higgs mass satisfies $m_H \lesssim 2m_{\rm top}$ and the transverse momenta of any jets produced in association with the Higgs satisfy $p_\perp \lesssim m_{\rm top}$ [115, 116].

We work in a theory in which the top quark has been integrated out and all other quarks are taken as massless. In this approach, the only coupling of the Higgs is to gluons[1], via the following term in the effective Lagrangian

$$\mathcal{L}_{\rm eff} = -\frac{H}{4} C_1^0 \mathcal{O}_1^0 \,, \qquad \mathcal{O}_1^0 = (G_0)^a_{\mu\nu} (G_0)^{a\mu\nu} \tag{B.1}$$

where C_1^0 is a coefficient function, zeros indicate that these are bare quantities and it is understood that they are defined in the five flavour effective theory. Both C_1^0 and matrix elements of $\mathcal{O}_1^0$ contain ultraviolet divergences, however their product is finite, since the operator in the full theory which (B.1) approximates ($\frac{H}{v} m_t \bar{\psi}\psi$) is a conserved current.

Using the Bogolyubov-Parasiuk R-operation [117, 118], it is possible to define

[1] We consistently ignore electro-weak couplings throughout.

a finite version of $\mathcal{O}_1^0$, which we denote $\mathcal{O}_1^R$. This finite operator may then be related to the bare operator as [118]

$$\mathcal{O}_1^R = Z_{\mathcal{O}_1}\mathcal{O}_1^0\,, \qquad Z_{\mathcal{O}_1} = \frac{1}{1-\beta(\mathcal{N}\alpha_s)/\epsilon} \tag{B.2}$$

where

$$\mathcal{N} = \exp[\epsilon(-\gamma_{\rm E} + \ln(4\pi))], \tag{B.3}$$

and $\beta(\alpha_s)$ and $\alpha_s \equiv \alpha_s(\mu)$ are the QCD beta function and the $\overline{\rm MS}$ running coupling respectively. Again, both are defined in the five flavour theory.

The effective Lagrangian now reads

$$\mathcal{L}_{\rm eff} = -\frac{H}{4}C_1^R\mathcal{O}_1^R \qquad C_1^R = Z_{\mathcal{O}_1}^{-1}C_1^0\,. \tag{B.4}$$

Since both matrix elements of $\mathcal{O}_1^R$ and the full expression are finite, C_1^R is also finite and is given by

$$C_1^R(\mu) = -\frac{1}{3v}\frac{\alpha_s(\mu)}{\pi}\left(1+\frac{11}{4}\frac{\alpha_s(\mu)}{\pi}\right) + \mathcal{O}(\alpha_s^3) \tag{B.5}$$

where again $\alpha_s(\mu)$ is the five flavour $\overline{\rm MS}$ running coupling and v is the Higgs vacuum expectation value.

The Feynman rules generated by equation (B.4) are displayed in figure B.1, written in terms of the standard three and four gluon vertices:

$$\begin{aligned} V^{a_1a_2a_3}_{3,\mu_1\mu_2\mu_3}(k_1,k_2,k_3) = gf^{a_1a_2a_3}\big(&g_{\mu_1\mu_2}(k_1-k_2)_{\mu_3} + g_{\mu_2\mu_3}(k_2-k_3)_{\mu_1} \\ &+ g_{\mu_3\mu_1}(k_3-k_1)_{\mu_2}\big) \end{aligned} \tag{B.6}$$

$$\begin{aligned} V^{a_1a_2a_3a_4}_{4,\mu_1\mu_2\mu_3\mu_4}(k_1,k_2,k_3,k_4) = -ig^2\big(&f^{a_1a_2e}f^{a_4a_3e}(g_{\mu_1\mu_4}g_{\mu_2\mu_3} - g_{\mu_1\mu_3}g_{\mu_4\mu_2}) \\ &f^{a_1a_3e}f^{a_4a_2e}(g_{\mu_1\mu_4}g_{\mu_2\mu_3} - g_{\mu_1\mu_2}g_{\mu_4\mu_3}) \\ &f^{a_1a_4e}f^{a_2a_3e}(g_{\mu_1\mu_2}g_{\mu_4\mu_3} - g_{\mu_1\mu_3}g_{\mu_4\mu_2})\big)\,. \end{aligned} \tag{B.7}$$

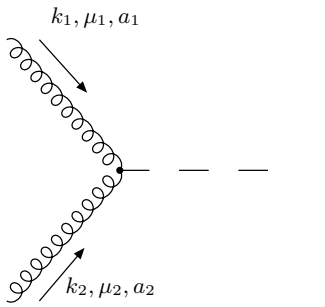

$$= \qquad -iC_1^R(\mu)\delta^{a_1a_2}(k_1 \cdot k_2 g^{\mu_1\mu_2} - k_2^{\mu_1}k_1^{\mu_2})$$

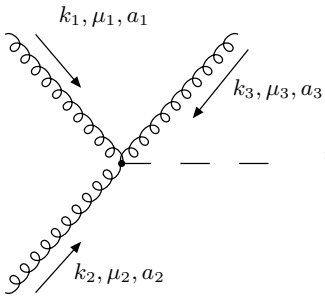

$$= \qquad -C_1^R(\mu)V^{a_1a_2a_3}_{3,\mu_1\mu_2\mu_3}(k_1, k_2, k_3)$$

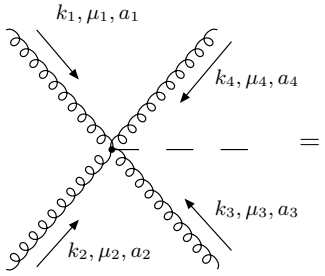

$$= \qquad -C_1^R(\mu)V^{a_1a_2a_3a_4}_{4,\mu_1\mu_2\mu_3\mu_4}(k_1, k_2, k_3, k_4)$$

Figure B.1: Feynman rules for the large top mass effective theory. See the text for the definitions of V_3 and V_4.

Bibliography

[1] John C. Collins, Davison E. Soper, and George Sterman. Factorization of Hard Processes in QCD. *Adv. Ser. Direct. High Energy Phys.*, **5**:1–91, 1988. hep-ph/0409313.

[2] R. J. Eden, P. V. Landshoff, D. I. Olive, and J. C. Polkinghorne. The Analytic S-matrix. *Cambridge University Press*, 1966.

[3] George Sterman. Mass Divergences in Annihilation Processes. 1. Origin and Nature of Divergences in Cut Vacuum Polarization Diagrams. *Phys. Rev.*, **D17**:2773, 1978.

[4] L. D. Landau. On analytic properties of vertex parts in quantum field theory. *Nucl. Phys.*, **13**:181–192, 1959.

[5] S. Coleman and R. E. Norton. Singularities in the physical region. *Nuovo Cim.*, **38**:438–442, 1965.

[6] George Sterman. Partons, factorization and resummation. 1995. hep-ph/9606312.

[7] George Sterman. An Introduction to Quantum Field Theory. *Cambridge University Press*, 1993.

[8] Geoffrey T. Bodwin, Stanley J. Brodsky, and G. Peter Lepage. Initial State Interactions and the Drell-Yan Process. *Phys. Rev. Lett.*, **47**:1799, 1981.

[9] John C. Collins and George Sterman. Soft partons in QCD. *Nucl. Phys.*, **B185**:172, 1981.

[10] John C. Collins, Davison E. Soper, and George Sterman. Soft Gluons and Factorization. *Nucl. Phys.*, **B308**:833, 1988.

[11] John C. Collins, Davison E. Soper, and George Sterman. Factorization is not violated. *Phys. Lett.*, **B438**:184–192, 1998. hep-ph/9806234.

[12] Jeffrey R. Forshaw, A. Kyrieleis, and M. H. Seymour. Super-leading logarithms in non-global observables in QCD. *JHEP*, **08**:059, 2006. hep-ph/0604094.

[13] J. R. Forshaw, A. Kyrieleis, and M. H. Seymour. Super-leading logarithms in non-global observables in QCD: Colour basis independent calculation. *JHEP*, **09**:128, 2008. 0808.1269.

[14] Jeffrey Forshaw, James Keates, and Simone Marzani. Jet vetoing at the LHC. *JHEP*, **07**:023, 2009. 0905.1350.

[15] Private communication, G. Sterman.

[16] John C. Collins, Davison E. Soper, and George Sterman. Factorization for Short Distance Hadron - Hadron Scattering. *Nucl. Phys.*, **B261**:104, 1985.

[17] A. V. Belitsky and A. V. Radyushkin. Unraveling hadron structure with generalized parton distributions. *Phys. Rept.*, **418**:1–387, 2005. hep-ph/0504030.

[18] R. Keith Ellis, W. James Stirling, and B. R. Webber. QCD and collider physics. *Camb. Monogr. Part. Phys. Nucl. Phys. Cosmol.*, **8**:1–435, 1996.

[19] V. N. Gribov and L. N. Lipatov. Deep inelastic e p scattering in perturbation theory. *Sov. J. Nucl. Phys.*, **15**:438–450, 1972.

[20] L. N. Lipatov. The parton model and perturbation theory. *Sov. J. Nucl. Phys.*, **20**:94–102, 1975.

[21] Guido Altarelli and G. Parisi. Asymptotic Freedom in Parton Language. *Nucl. Phys.*, **B126**:298, 1977.

[22] Yuri L. Dokshitzer. Calculation of the Structure Functions for Deep Inelastic Scattering and e+ e- Annihilation by Perturbation Theory in Quantum Chromodynamics. *Sov. Phys. JETP*, **46**:641–653, 1977.

[23] Andrey Grozin. Lectures on QED and QCD: Practical calculation and renormalization of one- and multi-loop Feynman diagrams. Hackensack, USA: World Scientific (2007) 224 p.

[24] Victor S. Fadin, E. A. Kuraev, and L. N. Lipatov. On the Pomeranchuk Singularity in Asymptotically Free Theories. *Phys. Lett.*, **B60**:50–52, 1975.

[25] E. A. Kuraev, L. N. Lipatov, and Victor S. Fadin. Multi - Reggeon Processes in the Yang-Mills Theory. *Sov. Phys. JETP*, **44**:443–450, 1976.

[26] E. A. Kuraev, L. N. Lipatov, and Victor S. Fadin. The Pomeranchuk Singularity in Nonabelian Gauge Theories. *Sov. Phys. JETP*, **45**:199–204, 1977.

[27] I. I. Balitsky and L. N. Lipatov. The Pomeranchuk Singularity in Quantum Chromodynamics. *Sov. J. Nucl. Phys.*, **28**:822–829, 1978.

[28] Jeffrey R. Forshaw and D. A. Ross. Quantum chromodynamics and the pomeron. *Cambridge Lect. Notes Phys.*, **9**:1–248, 1997.

[29] Stefan Dittmaier. Weyl-van-der-Waerden formalism for helicity amplitudes of massive particles. *Phys. Rev.*, **D59**:016007, 1999. hep-ph/9805445.

[30] Frits A. Berends and W. Giele. The Six Gluon Process as an Example of Weyl-Van Der Waerden Spinor Calculus. *Nucl. Phys.*, **B294**:700, 1987.

[31] Michelangelo L. Mangano and Stephen J. Parke. Multi-Parton Amplitudes in Gauge Theories. *Phys. Rept.*, **200**:301–367, 1991. hep-th/0509223.

[32] R. Keith Ellis, W. T. Giele, and G. Zanderighi. Semi-numerical evaluation of one-loop corrections. *Phys. Rev.*, **D73**:014027, 2006. hep-ph/0508308.

[33] Andrei I. Davydychev. A Simple formula for reducing Feynman diagrams to scalar integrals. *Phys. Lett.*, **B263**:107–111, 1991.

[34] T. Binoth, J. Ph. Guillet, G. Heinrich, E. Pilon, and C. Schubert. An algebraic / numerical formalism for one-loop multi-leg amplitudes. *JHEP*, **10**:015, 2005. hep-ph/0504267.

[35] Zvi Bern, Lance J. Dixon, and David A. Kosower. Dimensionally regulated pentagon integrals. *Nucl. Phys.*, **B412**:751–816, 1994. hep-ph/9306240.

[36] Valery A. Khoze, Alan D. Martin, and M. G. Ryskin. Double-diffractive processes in high-resolution missing- mass experiments at the Tevatron. *Eur. Phys. J.*, **C19**:477–483, 2001. hep-ph/0011393.

[37] M. G. Albrow and A. Rostovtsev. Searching for the Higgs at hadron colliders using the missing mass method. 2000. hep-ph/0009336.

[38] M. G. Albrow et al. [FP420 R and D Collaboration]. The FP420 R&D Project: Higgs and New Physics with forward protons at the LHC. *JINST*, **4**:T10001, 2009. 0806.0302.

[39] A. B. Kaidalov, V. A. Khoze, A. D. Martin, and M. G. Ryskin. Central exclusive diffractive production as a spin parity analyser: From hadrons to Higgs. *Eur. Phys. J.*, **C31**:387–396, 2003. hep-ph/0307064.

[40] T. Aaltonen et al. [CDF Collaboration]. Search for exclusive $\gamma\gamma$ production in hadron- hadron collisions. *Phys. Rev. Lett.*, **99**:242002, 2007. 0707.2374.

[41] T. Aaltonen et al. [CDF Collaboration]. Observation of Exclusive Dijet Production at the Fermilab Tevatron $p^{-}\bar{p}$ Collider. *Phys. Rev.*, **D77**:052004, 2008. 0712.0604.

[42] T. Aaltonen et al. [CDF Collaboration]. Observation of exclusive charmonium production and $\gamma\gamma$ to $\mu^{+}\mu^{-}$ in $p\bar{p}$ collisions at $\sqrt{s} = 1.96$ TeV. *Phys. Rev. Lett.*, **102**:242001, 2009. 0902.1271.

[43] Valery A. Khoze, Alan D. Martin, and M. G. Ryskin. Can the Higgs be seen in rapidity gap events at the Tevatron or the LHC? *Eur. Phys. J.*, **C14**:525–534, 2000. hep-ph/0002072.

[44] Valery A. Khoze, Alan D. Martin, and M. G. Ryskin. The rapidity gap Higgs signal at LHC. *Phys. Lett.*, **B401**:330–336, 1997. hep-ph/9701419.

[45] A. B. Kaidalov, V. A. Khoze, A. D. Martin, and M. G. Ryskin. Extending the study of the Higgs sector at the LHC by proton tagging. *Eur. Phys. J.*, **C33**:261–271, 2004. hep-ph/0311023.

[46] V. A. Khoze, A. D. Martin, and M. G. Ryskin. Prospects for new physics observations in diffractive processes at the LHC and Tevatron. *Eur. Phys. J.*, **C23**:311–327, 2002. hep-ph/0111078.

[47] Yuri L. Dokshitzer, Valery A. Khoze, and S. I. Troian. New perturbative results in hadron jet physics. LENINGRAD-86-1218.

[48] J. D. Bjorken. Rapidity gaps and jets as a new physics signature in very high-energy hadron hadron collisions. *Phys. Rev.*, **D47**:101–113, 1993.

[49] Yuri L. Dokshitzer, Valery A. Khoze, and T. Sjostrand. Rapidity gaps in Higgs production. *Phys. Lett.*, **B274**:116–121, 1992.

[50] Valery A. Khoze, Alan D. Martin, and M. G. Ryskin. Soft diffraction and the elastic slope at Tevatron and LHC energies: A MultiPomeron approach. *Eur. Phys. J.*, **C18**:167–179, 2000. hep-ph/0007359.

[51] M. G. Ryskin, A. D. Martin, and V. A. Khoze. Soft diffraction at the LHC: A Partonic interpretation. *Eur. Phys. J.*, **C54**:199–217, 2008. 0710.2494.

[52] A. D. Martin, V. A. Khoze, and M. G. Ryskin. Rapidity gap survival probability and total cross sections. 2008. 0810.3560.

[53] M. G. Ryskin, A. D. Martin, and V. A. Khoze. Soft processes at the LHC, I: Multi-component model. *Eur. Phys. J.*, **C60**:249–264, 2009. 0812.2407.

[54] M. G. Ryskin, A. D. Martin, and V. A. Khoze. Soft processes at the LHC, II: Soft-hard factorization breaking and gap survival. *Eur. Phys. J.*, **C60**:265–272, 2009. 0812.2413.

[55] A. D. Martin, V. A. Khoze, and M. G. Ryskin. Diffractive processes at the LHC. *AIP Conf. Proc.*, **1105**:252–257, 2009. 0811.1481.

[56] Alan D. Martin and M. G. Ryskin. Unintegrated generalised parton distributions. *Phys. Rev.*, **D64**:094017, 2001. hep-ph/0107149.

[57] A. G. Shuvaev, Krzysztof J. Golec-Biernat, Alan D. Martin, and M. G. Ryskin. Off-diagonal distributions fixed by diagonal partons at small x and ξ. *Phys. Rev.*, **D60**:014015, 1999. hep-ph/9902410.

[58] Yuri L. Dokshitzer, Dmitri Diakonov, and S. I. Troian. Hard Processes in Quantum Chromodynamics. *Phys. Rept.*, **58**:269–395, 1980.

[59] V. A. Khoze, A. D. Martin, and M. G. Ryskin. Early LHC measurements to check predictions for central exclusive production. *Eur. Phys. J.*, **C55**:363–375, 2008. 0802.0177.

[60] Private communication, M. Ryskin.

[61] Mikhail A. Shifman, A. I. Vainshtein, M. B. Voloshin, and Valentin I. Zakharov. Low-Energy Theorems for Higgs Boson Couplings to Photons. *Sov. J. Nucl. Phys.*, **30**:711–716, 1979.

[62] M. B. Voloshin. Once Again About the Role of Gluonic Mechanism in Interaction of Light Higgs Boson with Hadrons. *Sov. J. Nucl. Phys.*, **44**:478, 1986.

[63] John R. Ellis, Mary K. Gaillard, and Dimitri V. Nanopoulos. A Phenomenological Profile of the Higgs Boson. *Nucl. Phys.*, **B106**:292, 1976.

[64] R. E. Cutkosky. Singularities and discontinuities of Feynman amplitudes. *J. Math. Phys.*, **1**:429–433, 1960.

[65] J. R. Cudell, A. Dechambre, O. F. Hernandez, and I. P. Ivanov. Central exclusive production of dijets at hadronic colliders. *Eur. Phys. J.*, **C61**:369–390, 2009. 0807.0600.

[66] J. F. Gunion and Davison E. Soper. Quark Counting and Hadron Size Effects for Total Cross- Sections. *Phys. Rev.*, **D15**:2617–2621, 1977.

[67] E. M. Levin and M. G. Ryskin. Born Approximation of QCD for Description of High-Energy Hadronic Interactions. *Sov. J. Nucl. Phys.*, **34**:619–623, 1981.

[68] S. Catani, B. R. Webber, and G. Marchesini. QCD coherent branching and semiinclusive processes at large x. *Nucl. Phys.*, **B349**:635–654, 1991.

[69] A. Bassetto, M. Ciafaloni, and G. Marchesini. Jet Structure and Infrared Sensitive Quantities in Perturbative QCD. *Phys. Rept.*, **100**:201–272, 1983.

[70] M. Spira, A. Djouadi, D. Graudenz, and P. M. Zerwas. Higgs boson production at the LHC. *Nucl. Phys.*, **B453**:17–82, 1995. hep-ph/9504378.

[71] Z. Kunszt, S. Moretti, and W. James Stirling. Higgs production at the LHC: An update on cross sections and branching ratios. *Z. Phys.*, **C74**:479–491, 1997. hep-ph/9611397.

[72] Wolfram Research Inc. Mathematica, Version 6.0.

[73] J.A.M. Vermaseren. New features of FORM. math-ph/0010025.

[74] R. Mertig, M. Bohm, and Ansgar Denner. FEYN CALC: Computer algebraic calculation of Feynman amplitudes. *Comput. Phys. Commun.*, **64**:345–359, 1991.

[75] Roger Cutler and Dennis W. Sivers. Quantum Chromodynamic Gluon Contributions to Large p(T) Reactions. *Phys. Rev.*, **D17**:196, 1978.

[76] J. Monk and A. Pilkington. ExHuME: A Monte Carlo event generator for exclusive diffraction. *Comput. Phys. Commun.*, **175**:232–239, 2006. hep-ph/0502077.

[77] A. D. Martin, R. G. Roberts, W. J. Stirling, and R. S. Thorne. Uncertainties of predictions from parton distributions. I: Experimental errors. *Eur. Phys. J.*, **C28**:455–473, 2003. hep-ph/0211080.

[78] J. Pumplin et al. New generation of parton distributions with uncertainties from global QCD analysis. *JHEP*, **07**:012, 2002. hep-ph/0201195.

[79] P. J. Bussey, T. D. Coughlin, Jeffrey R. Forshaw, and A. D. Pilkington. Central exclusive production of longlived gluinos at the LHC. *JHEP*, **11**:027, 2006. hep-ph/0607264.

[80] Nima Arkani-Hamed and Savas Dimopoulos. Supersymmetric unification without low energy supersymmetry and signatures for fine-tuning at the LHC. *JHEP*, **06**:073, 2005. hep-th/0405159.

[81] G. F. Giudice and A. Romanino. Split supersymmetry. *Nucl. Phys.*, **B699**:65–89, 2004. hep-ph/0406088.

[82] Glennys R. Farrar and Pierre Fayet. Phenomenology of the production, decay and detection of new hadronic states associated with supersymmetry. *Phys. Lett.*, **B76**:575–579, 1978.

[83] Stuart Raby and Kazuhiro Tobe. The phenomenology of SUSY models with a gluino LSP. *Nucl. Phys.*, **B539**:3–22, 1999. hep-ph/9807281.

[84] Howard Baer, King-man Cheung, and John F. Gunion. A heavy gluino as the lightest supersymmetric particle. *Phys. Rev.*, **D59**:075002, 1999. hep-ph/9806361.

[85] Kingman Cheung and Wai-Yee Keung. Split supersymmetry, stable gluino, and gluinonium. *Phys. Rev.*, **D71**:015015, 2005. hep-ph/0408335.

[86] E. Bouhova-Thacker, V. Kartvelishvili, and A. Small. Search for gluino gluino bound states. *Nucl. Phys. Proc. Suppl.*, **133**:122–125, 2004.

[87] E. Chikovani, V. Kartvelishvili, R. Shanidze, and G. Shaw. Bound States of Two Gluinos at the Tevatron and LHC. *Phys. Rev.*, **D53**:6653–6657, 1996. hep-ph/9602249.

[88] T. Goldman and H. Haber. Gluinonium: The hydrogen atom of supersymmetry. *Physica*, **15D**:181–196, 1985.

[89] P. Gambino, G. F. Giudice, and P. Slavich. Gluino decays in split supersymmetry. *Nucl. Phys.*, **B726**:35–52, 2005. hep-ph/0506214.

[90] Asimina Arvanitaki, Chad Davis, Peter W. Graham, Aaron Pierce, and Jay G. Wacker. Limits on split supersymmetry from gluino cosmology. *Phys. Rev.*, **D72**:075011, 2005. hep-ph/0504210.

[91] JoAnne L. Hewett, Ben Lillie, Manuel Masip, and Thomas G. Rizzo. Signatures of long-lived gluinos in split supersymmetry. *JHEP*, **09**:070, 2004. hep-ph/0408248.

[92] V. M. Abazov et al. [D0 Collaboration]. Search for stopped gluinos from $p\bar{p}$ collisions at $\sqrt{s} = 1.96$-TeV. *Phys. Rev. Lett.*, **99**:131801, 2007. 0705.0306.

[93] Ansgar Denner, H. Eck, O. Hahn, and J. Kublbeck. Compact Feynman rules for Majorana fermions. *Phys. Lett.*, **B291**:278–280, 1992.

[94] K. Adel and F. J. Yndurain. Production of heavy quarks close to threshold. *Phys. Rev.*, **D52**:6577–6594, 1995. hep-ph/9502290.

[95] W. Beenakker, R. Hopker, M. Spira, and P. M. Zerwas. Squark and gluino production at hadron colliders. *Nucl. Phys.*, **B492**:51–103, 1997. hep-ph/9610490.

[96] Michael S. Chanowitz and Stephen R. Sharpe. Spectrum of gluino bound states. *Phys. Lett.*, **B126**:225, 1983.

[97] Franco Buccella, Glennys R. Farrar, and Alessandra Pugliese. R Baryon masses. *Phys. Lett.*, **B153**:311, 1985.

[98] M. Foster and C. Michael [UKQCD Collaboration]. Hadrons with a heavy colour-adjoint particle. *Phys. Rev.*, **D59**:094509, 1999. hep-lat/9811010.

[99] Gabriel Karl and Jack E. Paton. Gluelump spectrum in the bag model. *Phys. Rev.*, **D60**:034015, 1999. hep-ph/9904407.

[100] Arash Mafi and Stuart Raby. An analysis of a heavy gluino LSP at CDF: The heavy gluino window. *Phys. Rev.*, **D62**:035003, 2000. hep-ph/9912436.

[101] Aafke Christine Kraan. Interactions of heavy stable hadronizing particles. *Eur. Phys. J.*, **C37**:91–104, 2004. hep-ex/0404001.

[102] W. Kilian, T. Plehn, P. Richardson, and E. Schmidt. Split supersymmetry at colliders. *Eur. Phys. J.*, **C39**:229–243, 2005. hep-ph/0408088.

[103] A. C. Kraan, J. B. Hansen, and P. Nevski. Discovery potential of R-hadrons with the ATLAS detector. 2005. hep-ex/0511014.

[104] A. Arvanitaki, S. Dimopoulos, A. Pierce, S. Rajendran, and Jay G. Wacker. Stopping gluinos. 2005. hep-ph/0506242.

[105] Michael Edward Peskin and Daniel V. Schroeder. An Introduction to quantum field theory. *Reading, USA: Addison-Wesley.*

[106] T. Sjöstrand et al. Pythia. *Computer Phys. Commun.*, **135**:238, 2001.

[107] Brian E. Cox and Jeffrey R. Forshaw. POMWIG: HERWIG for diffractive interactions. *Comput. Phys. Commun.*, **144**:104–110, 2002. hep-ph/0010303.

[108] Jeff R. Forshaw. Diffractive Higgs production: Theory. 2005. hep-ph/0508274.

[109] Vladimir A. Smirnov. Evaluating Feynman integrals. *Springer Tracts Mod. Phys.*, **211**:1–244, 2004.

[110] C. Anastasiou, E. W. Nigel Glover, and C. Oleari. Scalar One-Loop Integrals using the Negative-Dimension Approach. *Nucl. Phys.*, **B572**:307–360, 2000. hep-ph/9907494.

[111] Hung Jung Lu and Christopher A. Perez. Massless one loop scalar three point integral and associated Clausen, Glaisher and L functions. SLAC-PUB-5809.

[112] N. I. Usyukina and Andrei I. Davydychev. An Approach to the evaluation of three and four point ladder diagrams. *Phys. Lett.*, **B298**:363–370, 1993.

[113] Zvi Bern, Lance J. Dixon, and David A. Kosower. One-loop amplitudes for e^+e^- to four partons. *Nucl. Phys.*, **B513**:3–86, 1998. hep-ph/9708239.

[114] Ansgar Denner, U. Nierste, and R. Scharf. A Compact expression for the scalar one loop four point function. *Nucl. Phys.*, **B367**:637–656, 1991.

[115] V. Del Duca, W. Kilgore, C. Oleari, C. Schmidt, and D. Zeppenfeld. Gluon-fusion contributions to H + 2 jet production. *Nucl. Phys.*, **B616**:367–399, 2001. hep-ph/0108030.

[116] V. Del Duca, W. Kilgore, C. Oleari, C. R. Schmidt, and D. Zeppenfeld. Kinematical limits on Higgs boson production via gluon fusion in association with jets. *Phys. Rev.*, **D67**:073003, 2003. hep-ph/0301013.

[117] N. N. Bogolyubov and D. V. Shirkov. Introduction to the theory of quantized fields. *Intersci. Monogr. Phys. Astron.*, **3**:1–720, 1959.

[118] V. P. Spiridonov. Anomalous Dimension of $G^2_{\mu\nu}$ and β-function. IYaI-P-0378.